Improving Sorption Compressors for Cryogenic Cooling

MESA+
Institute for Nanotechnology

The research described in this thesis is part of and financially supported by the THz research orientation of the MESA+ research institute. It was carried out at the Low Temperature Division of the faculty of Science and Technology of the University of Twente.

Print: Febodruk b.v., Enschede

ISBN 90-365-2213-7

IMPROVING SORPTION COMPRESSORS FOR CRYOGENIC COOLING

PROEFSCHRIFT

ter verkrijging van
de graad van doctor aan de Universiteit Twente,
op gezag van de rector magnificus,
prof. dr. W.H.M. Zijm,
volgens besluit van het College voor Promoties
in het openbaar te verdedigen
op donderdag 23 juni 2005 om 15.00 uur

door

Gideon Frederik Maria Wiegerinck

geboren op 19 maart 1975
te Aalten.

Dit proefschrift is goedgekeurd door de promotoren:

prof. dr. ir. H.J.M. ter Brake
prof. dr. H. Rogalla

Contents

Chapter 1

Introduction

1.1 The THz project

The aim of the THz project of the MESA+ research institute, as defined in 1999, is to demonstrate an analogue-to-digital converter (ADC) with an input signal bandwidth of 60 MHz and an output resolution of 14-16 bits. The analog input signal will be sampled by a digitiser made of high-T_c superconducting circuits. The outgoing bit stream has to be slowed down to a speed that CMOS can handle. InP and GaAs are possible candidates for this decimation step. Besides the speed reduction, the output signal of the superconducting circuits, typically on the order of 0.5 mV, has to be increased to semiconductor level, typically hundreds of millivolts. The superconducting circuits require cooling and the aim is to realise this by means of a closed-cycle cooling system. To reduce the amount of bit errors made by the digitiser, it is advantageous to have the operating temperature as low as possible. To achieve an acceptable bit error probability, the temperature should not exceed 40 K [1, 2]. A lower temperature is preferred as a 10 K lower temperature gives a bit error probability that is two orders of magnitude lower. Therefore, the aim was set to 30 K. Also cooling of the semiconducting devices is advantageous. Their performance can be largely improved by cooling: lower noise can be established and higher speed can be achieved in digital circuits. It was therefore proposed to also consider cooling of the semiconductor electronics. An operating temperature between 80 K and 150 K seems likely as will be discussed in section 2.1.

Four options were considered to cool the THz ADC demonstrator and these are shown schematically in figure 1.1. In the first option (A), only the superconductor stage is cooled. In the other three options (B1 to B3), the semiconductor stage is also

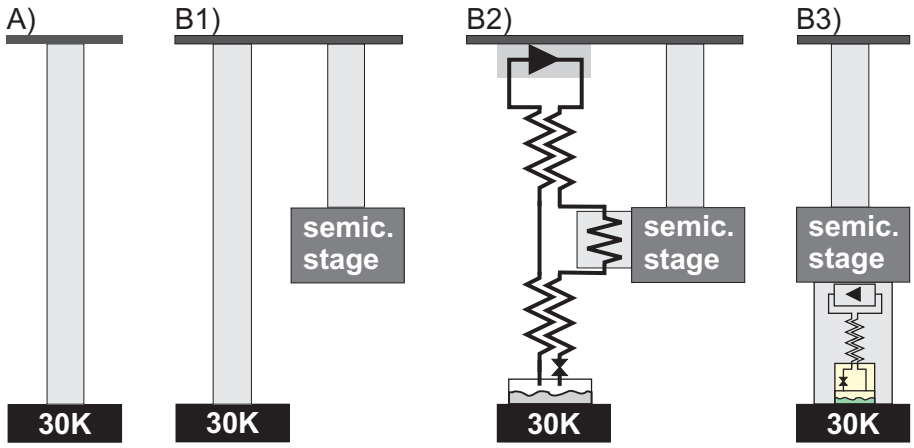

Figure 1.1: Cooling options for the THz demonstrator. Option A: only cooling of superconductor stage. Option B1: Both the superconductor and the semiconductor stages are cooled from room temperature. Option B2: The cooler of the semiconductor stage precools high-pressure gas that is compressed at room temperature. The precooled gas is expanded in a Joule-Thomson valve to establish 30 K. Option B3: The cooler of the semiconductor stage acts as a heat sink for a small cooler consisting of a sorption compressor combined with a Joule-Thomson expansion stage that cools to 30 K.

cooled and the cooling system for the demonstrator needs to realise two different temperature stages. The required cooling powers at these two temperatures differ considerably. The semiconductor stage requires a powerful cooler with a cooling capacity of more than 10 W whereas a capacity on the order of tenths of a watt is needed to cool the superconductor stage as is discussed in chapter 2. An option is to use two separate coolers that each cool from room temperature to the desired temperature. This is cooling configuration B1 in figure 1.1. In option B2, the powerful cooler for the semiconductor stage is used to precool high-pressure gas that is compressed at room temperature and is expanded in a Joule-Thomson restriction to cool the superconductors. Neon or hydrogen can be taken as the working gas. Since the required cooling powers at the two temperature stages differ significantly, a much more elegant solution, option B3, would be to mount a small cooler onto the powerful cooler, next to the semiconductor electronics. This cooler should cool from the temperature of the semiconductor stage to that of the superconductor stage. For this purpose, a sorption compressor in combination with a Linde-Hampson cold stage can be taken as this cooler can be scaled to small sizes and has the potential for a long lifetime. The majority of the work described in this thesis is devoted to such a sorption compressor unit. An introduction to this work is given in the next

section. Cooler specifications like input power, mass, and price for the coolers in the above-mentioned cooling options are discussed in section 3.7.

1.2 Sorption cooler development

A sorption compressor cell basically consists of a container that is filled with a sorbent. This can either be a physical or a chemical sorber [3, 4]. Microporous activated carbons, zeolites and silica gels are some typical physical sorbers [5] whereas metal-hydrides are well-known chemical sorbers [6]. A container filled with a sorber material can act as a compressor by thermally cycling the sorbent and at the same time controlling the gas flow to and from the system. One can distinguish four different parts in the cycle. These are schematically shown in figure 1.2 that depicts the isotherms of xenon on Maxsorb activated carbon as an illustrative example. Starting from an initial low (heat sink) temperature and pressure, during the first part of the cycle (A) the sorber container is heated while no gas can flow into or out off the compressor cell, so the total amount of gas in the container is constant. Adsorbed gas comes off the surface and builds up pressure in the void volume. When, at some point, the container is opened, high-pressure gas flows out (phase B). In this phase, further heating of the container is required to keep the pressure constant. When most of the gas has come off the surface, the container is cooled back to the heat sink temperature and the container is closed (phase C). Gas from the void volume now adsorbs onto the surface of the sorber material, causing the pressure in the container

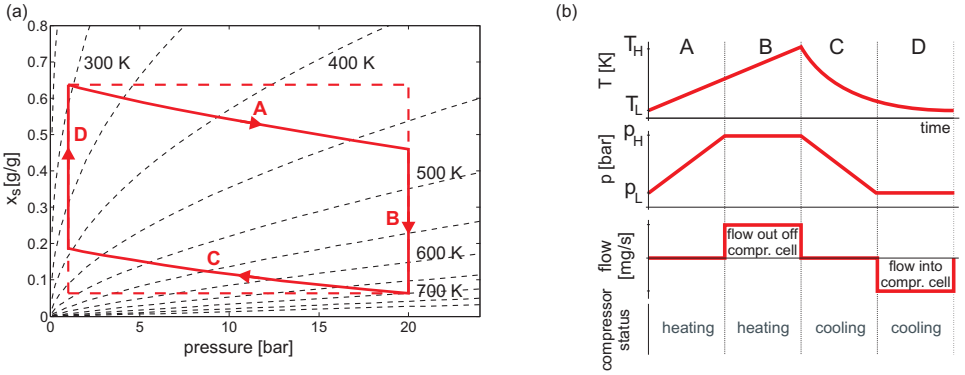

Figure 1.2: (a) Amount of adsorbed xenon per gram of sorber material x_s during the sorption cycle for Maxsorb activated carbon. (b) Temperature, pressure, flow and compressor status with time during the sorption cycle.

	Boiling point [K]	Maximum inversion temp. [K]	Critical temp. [K]	Critical pressure [bar]	Triple point temp. [K]	Triple point pressure [bar]
Helium-4	4.2	40	5.2	2.3	2.2	0.05
Hydrogen	20.2	205	32.9	12.8	13.8	0.07
Neon	27.1	250	44.4	26.5	24.6	0.43
Nitrogen	77.2	621	126.2	34.0	63.1	0.13
Argon	87.2	794	150.9	49.1	83.8	0.69
Oxygen	90.1	761	154.6	50.4	54.4	$1.5 \cdot 10^{-3}$
Methane	111.5	939	190.6	46.0	90.7	0.12
Krypton	119.6		209.4	55.0	115.8	0.73
Xenon	164.8		289.7	58.2	161.4	0.82
Ethylene	169.0		282.3	50.4	104.0	$1.2 \cdot 10^{-3}$

Table 1.1: Properties of gases that can achieve temperatures lower than 170 K when used in a Linde-Hampson cold stage. Data was taken from GasPak [8].

to drop. At a sufficiently low pressure, gas should be supplied to the sorber container in order to return to the starting point (phase D). So, during only one phase of the cycle (phase B) high-pressure gas is supplied by the cell and during another phase (phase D) low-pressure gas is taken up by the cell. In the other two phases no gas flows into or out off the system.

Cooling is obtained when the created high-pressure gas is expanded by a Joule-Thomson (JT) expansion in a Linde-Hampson (LH) cold stage, see e.g. [7]. The cold-stage temperature that is realised is the temperature at which the gas-liquid phase transition occurs at the low pressure of the compressor. An overview of relevant properties of gases that can be used to realise a cold-stage temperature below 170 K is given in table 1.1. Obviously, for the cooling options B2 and B3 in figure 1.1, neon or hydrogen need to be applied

A LH cold stage needs a more or less continuous mass flow in order to provide continuous cooling power, whereas an individual sorption cell provides an intermittent flow. In general, a continuous flow is obtained by using three or more compressor cells. They are operated out of phase and their phases are synchronised. A set of valves is used to convert the intermittent flows of the individual cells to a continuous flow through the cold stage. A schematic picture of such a cooler using four sorption cells is shown in figure 1.3. Bowman *et al.* [4] recently published an overview of closed-cycle JT cryocoolers with a focus on sorption compressors.

Coolers that consist of a sorption compressor with a LH cold stage have several advantages. They are thermally driven and have no moving parts, apart from the valves. As a consequence, they can be scaled to small sizes [10] and can operate

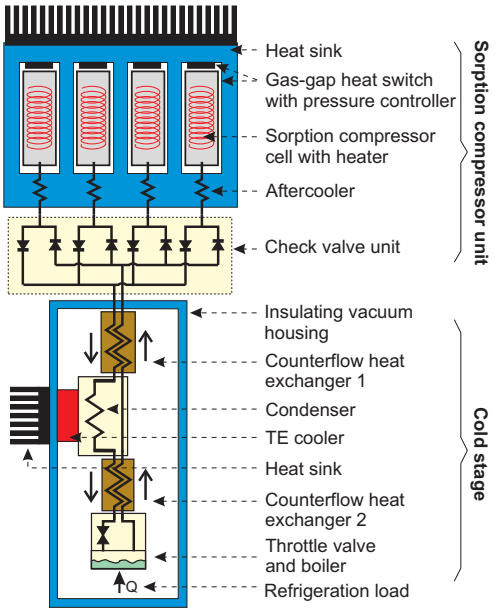

Figure 1.3: Sorption compressor with a Linde-Hampson cold stage using four sorption compressor cells operating 90 degrees out of phase. For more information, see e.g. [9].

with an absolute minimum vibration level. Besides, wear-related issues hardly play a role giving the potential for a long cooler lifetime. A disadvantage of this cooler type is the relatively complex compressor design including three or more compressor cells, each consisting of a container filled with sorber material and equipped with a heater, a heat switch with an actuator, and some means to control the heater and the heat switch actuator. As more complicated components in a system increase the risk of failures, a reduction of complexity would increase the reliability of the cooler. Another drawback of a sorption compressor, combined with a LH cold stage, is that, in many cases, the cooler is relatively inefficient compared to other types of coolers. Every time the container is to be pressurised, the complete container including sorber material, heater, and walls needs to be heated. When the compressor is operated at low temperatures, this negative effect on the efficiency is smaller compared to room temperature operation as the heat capacities are lower. Furthermore, a considerable amount of pressurised gas remains in the void volume of the sorber material and does not contribute to the mass flow through the cold stage. With respect to sorption compressors, this thesis addresses both the issue of complexity and that of efficiency. An outline of this thesis is given in the next section.

1.3 Outline

This thesis explores the cooling options for the THz ADC demonstrator. First, the boundary conditions for the cooling system were determined and this is discussed in chapter 2. To do this, three configurations that differ in the way high-speed data is transported from the superconductor stage to the semiconductor stage were used as starting points. The required cooling powers for these configurations were estimated based on simple assumptions for the cooling system and commonly used techniques for heat load reduction.

To select a cooler for a specific application, it is useful to have an overview of up-to-date cryocooler specifications. Such a database is also useful to derive trends that can be used as a first estimate of the cooler specifications based on the cold-stage temperature and the required cooling power. Such a database was compiled and trends were derived. This is discussed in chapter 3. This chapter concludes with an estimate of the input power, mass, and cost of the four cooling configurations for the THz demonstrator from section 1.1.

One of the cooling options for the THz demonstrator uses a powerful cooler for the semiconductor stage that also acts as a precooler for high-pressure gas that is compressed at room temperature and expanded in a JT restriction. This concept was applied to make a cooler that is suitable to cool a MgB_2-SQUID. The cooler was fully made out of glass and precooling was provided by liquid nitrogen. The design of the cooler and its operation is discussed in chapter 4.

The majority of the research described in this thesis is performed on improving a sorption compressor that is coupled to a LH cold stage. In the cooling system of the THz demonstrator, such a cooler in miniature form can be used to cool the superconductor stage from the temperature of the semiconductor stage. The cooler can, however, also be attractive in other applications. As denoted in section 1.2, the conventional design of a sorption compressor is rather complex. In chapter 5, an alternative sorption compressor design, consisting of a single compressor cell, two check valves and two buffer volumes, is introduced. As set out by Bard [11], the efficiency can be increased by application of two-stage compression. In chapter 5, also a model was developed to determine the efficiencies of both a single-stage and a two-stage compressor. This was combined with a standard thermodynamic treatment of the cold stage to determine the cooler efficiency. The influence of two-stage compression on the compressor efficiency and on the cooler efficiency was studied. Application of a two-stage compressor also gives the opportunity to precool the high-pressure gas by an additional JT expansion stage between the high-pressure and the intermediate pressure.

A set-up was built to investigate the operation of the single-stage single-cell compressor configuration. Its design and operation are discussed in chapter 6. A property of the single-cell compressor concept is that the pressures in both buffers vary with time. This is especially an attention point in the design of the low-pressure buffer as the pressure in this buffer is directly related to the temperature of the liquid in the boiler. Variations in this pressure result in some fluctuation in this temperature. The most simple buffers that can be applied in the single-cell design are 'empty' volumes. However, the sizes required to keep the pressure variations at an acceptable level are large compared to the compressor volume. The sizes of the buffers can be reduced by filling them with a sorber material which improves their storage capacities. Alternatively, application of a sorber in the buffers and unchanged buffer sizes will result in smaller pressure variations. A further reduction in buffer size and in pressure variation can be achieved by means of actively heating and cooling of the sorber material in the buffer at the cost of some input power. The compressor was operated with these three types of buffers and the sizing and operation of the buffers is also discussed in chapter 6.

Realisation of a two-stage compressor with the conventional compressor design results in an extremely complex compressor, with at least 6 compressor cells and 12 check valves. Therefore, the advantages of the single-cell concept become even more pronounced when applied to a two-stage compressor. A two-stage compressor set-up was realised based on the single-cell concept. Two-stage compression can be used to improve the efficiency compared to a single-stage compressor operating between the same pressures. Alternatively, two-stage compression also enables compression to higher pressures at the cost of some compressor efficiency. Often, application of higher pressures improves the efficiency of the cold stage. This depends on the selected gas, on the operating pressures, the precool temperature and the heat sink temperature. Measurements were done to verify both features of the two-stage compressor and these are described and the results discussed in chapter 7. The efficiencies found were compared with the calculated efficiencies predicted by the model from chapter 5. In chapter 8, conclusions on the work performed and an outlook are given.

References

[1] Personal communication with the partners of the THz-project. MESA+ research institute, University of Twente, PO Box 217, 7500 AE, Enschede, The Netherlands, http://www.mesaplus.utwente.nl.

[2] J. Satchell. Limitations on HTS single flux quantum logic. *IEEE transactions on*

applied superconductivity, 9(2), 1999.

[3] L. A. Wade. An overview of the development of sorption refrigeration. In *Adv. in Cryogenic Eng.*, volume 37, pages 1095–1106, 1992.

[4] R. C. Bowman Jr, B. Kiehl, and E. Marquardt. *Spacecraft Thermal Control Handbook*, volume 2, chapter 10, pages 187–216. The Aerospace Press, El Segundo, California, 2003.

[5] V. C. Menon and S. Komarneni. Porous adsorbents for vehicular natural gas storage: A review. *Journal of Porous Materials*, 5:4358, 1998.

[6] L. Schlapbach, editor. *Hydrogen in intermetallic compounds*, volume 63 and 67 of *Topics in applied physics*. Springer-Verlag, Berlin, 1992.

[7] G. Walker. *Miniature refrigerators for cryogenic sensors and cold electronics*. Clarendon Press, 1989.

[8] Cryodata Inc., P.O. box 558, Niwot, CO 80544, USA, http://www.cryodata.com.

[9] J. F. Burger, H. J. M. ter Brake, H. J. Holland, J. W. Berenschot, M. Elwenspoek, and H. Rogalla. A 170 K microcooler with a thermal sorption compressor and a micromachined cold stage. *submitted to Cryogenics*, 2005.

[10] J. F. Burger. *Cryogenic Microcooling, A micromachined cold stage operating with a sorption compressor in a vapor compression cycle*. PhD thesis, University of Twente, The Netherlands, 1987. downloadable from: http://purl.org/utwente/23470.

[11] S. Bard. Improving adsorption cryocoolers by multi-stage compression and reducing void volume. *Cryogenics*, 26:450 – 458, 1986.

Chapter 2

THz design specifications

2.1 THz ADC demonstrator system

The ADC demonstrator as introduced in section 1.1 can be realised in several ways. Three basic configurations were distinguished that differ in the way high-speed data is transported from the superconductor stage to the semiconductor stage: by coaxial lines, by an optical fibre or by striplines (see figure 2.1) [1]. The requirements for the cooling system were determined based on these three configurations. An important issue is the temperature of the semiconductor stage. This temperature affects the performance of the semiconductors, the efficiency, mass and size of the cooler and the heat load to both stages. At the start of the project, the temperature range of the first stage was set to 80 K to 150 K. At the latter temperature, the increase in performance of semiconductors with respect to speed and noise is already appreciable [2]. At lower temperatures, carrier freeze out may become relevant and technologies alternative to CMOS may need to be applied. In general, however, performance increases at lower temperatures at the cost of more intensive cooling. The lowest temperature of 80 K was set to allow the incorporation of high-T_c superconducting components in the signal processing, such as passive narrow-band filtering. The influence of the operating temperature on the cooler specifications will be discussed in chapter 3.

2.2 Design specifications for the cooling system

At the start of the project, an inventory of the specifications, as defined by the partners in the THz project, was made. This turned out to be a complicated task, as the

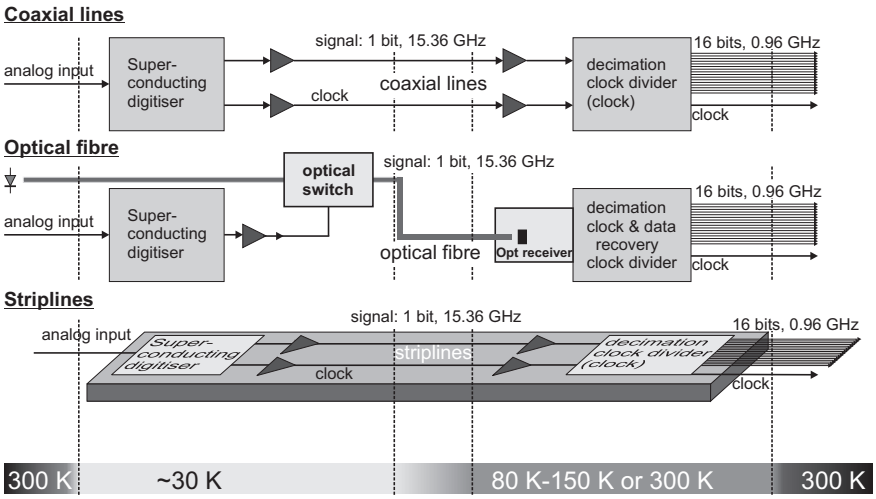

Figure 2.1: Basic configurations of the THz ADC demonstrator set-up. The application of striplines was only considered for the case of cooled semiconductors.

work on the components had just been started and many design options were still open. For the superconductor stage, the aim for the temperature was set at 30 K (see section 1.1). Both the temperature stability and the temperature gradient over the cold stage have to be smaller than about 0.3 K. The DC magnetic background field must not exceed about 2 nT. Sufficient shielding can be obtained by using a high-permeability material [3]. Some shielding of the AC magnetic background field, which is typically about 0.1 nT/$\sqrt{\text{Hz}}$ at 10 Hz [4], is necessary but probably application of a thermal radiation shield already gives sufficient field reduction.

One of the possible applications of the THz ADC demonstrator is using it in base stations for mobile telecommunications. This was kept in mind when defining the specifications for the system as a whole. The size has to be smaller than about 50 x 50 x 50 cm^3. The system needs to be portable and this implies a maximum weight of about 10 kg. There was no stringent requirement on the input power. As a starting point it was suggested that the efficiency should be comparable with commercial 30 K coolers. For commercial application in mobile telecommunications, the total system price should not exceed about 5,000 €. In other applications where the system has a clear advantage over other technologies, considerably higher prices may be acceptable. Roughly ten percent of this amount is reserved for the cooler. A standard requirement for base stations is that they can operate between -33 ℃ to +40 ℃ and that they have a lifetime of 10 - 20 years [5]. This is extremely long. However, intermediate maintenance is allowed.

2.3 Heat load analysis

The heat load to the superconductor stage and the cooled semiconductor stage consists of dissipation of the devices at that stage, radiation, thermal load from wires that are connected to that stage, a contribution from the support structure and conduction through the residual gas in the vacuum space. In the next sections, these contributions are estimated for the different configurations of the ADC demonstrator based on simple assumptions for the cooling set-up.

2.3.1 Dissipation

The components of the THz demonstrator are part of research within MESA+ or the Super-ADC project [6]. Each group working on a specific device has provided an estimate of the dissipation of that device [1]. The dissipation of the digitiser was estimated at 10 mW. At the superconductor stage, pre-amplification is needed to prevent reduction of the signal-to-noise ratio because of the increase in thermal noise when the signal is transferred to a higher temperature. For this purpose, the use of 9 dB 15 GHz InP amplifiers with an aimed dissipation of 3 mW was assumed [6]. The number of amplifiers was estimated assuming that an analog signal instead of a digital signal has to be transported to a higher temperature. This results in a contribution of 6 mW in case of cooled semiconductors and 12 mW for room temperature operation. When an optical fibre is used for the data transport, the electrical signal is converted to an optical signal at the superconductor stage. All amplification that is needed to increase the voltage to an acceptable level for the optical switch, which is about 100 mV, has to be put on the superconductor stage. As a result, the contribution to the heat load is higher than for electrical data transport and was estimated at 18 mW. The loss of optical power was estimated at 3 mW. The total dissipation for the superconductor stage is then between 16 and 31 mW, depending on the configuration that is chosen.

The total dissipation of the CMOS decimation filter, clock, clock divider and amplification at the semiconductor stage was estimated at 11 W. This number was based on extrapolations of dissipation of electronics with similar functionality operating at lower temperatures [1].

2.3.2 Radiation

When the semiconductors are operated at room temperature, the radiation heat load to the superconductor stage will be considerable and can be reduced by application

of a floating radiation shield, see e.g. [7]. Such a lay-out is shown schematically in figure 2.2a and results in a heat load of 0.12 W. A further reduction can be obtained by increasing the number of shields, for instance by using multiple layers of aluminised Mylar foil. With the dimensions and emissivities [8] from the figure and assuming that 25 layers of foil are applied, the heat load reduces to 38 mW [9, 10]. The temperature of the inner layer of the shields is estimated at 202 K.

When the superconductor stage is cooled, a configuration like in figure 2.2b results. The radiation shield that surrounds the superconductor stage is now actively cooled reducing the temperature of this shield, and thus the radiation, significantly. For the superconductor stage, the heat load is 13 mW when the shield is at 150 K and 1.0 mW when at 80 K. Additionally, a floating temperature shield is assumed around the semiconductor stage resulting in a radiation load to that stage of about 0.5 W in the temperature range from 80 K to 150 K.

When both the superconductor and the semiconductor electronics are on a single substrate, a lay-out as in figure 2.2c can be taken. The heat load to the superconductor stage is 0.3 mW when the semiconductors are cooled to 80 K and 3.1 mW when cooled to 150 K. The radiative load to the semiconductor stage is 0.2 W. We assumed a relatively high emissivity, ϵ = 0.5, as the substrate material will probably be selected based on the requirements for high-speed electrical signal transport rather than for its thermal properties.

2.3.3 Thermal load caused by wires

For cooled electronics, a variety of wires connect the cold devices to the outside world and they contribute to the heat loads at the cold stages. This load consists of heat conduction from the hot end temperature of the wire, dissipation within the wire and radiation to the wire. If dissipation and radiation are negligible, the heat flow can be derived from the Fourier-Biot relation as [11]

$$\dot{Q}_{conduction} = \frac{A}{l} \int_{T_L}^{T_H} \lambda(T) dT \tag{2.1}$$

Here, A is the cross-sectional area of the wire, l its length, λ the thermal conductivity, T_L and T_H are the low-end and high-end temperatures of the wire, respectively. From this equation it is obvious that the conductive load can be reduced by reducing A/l or by reducing the thermal conductivity. The heat load to the cold tip can also be reduced by heat sinking the wire at intermediate temperatures, e.g. by winding it along the cold stage. This can, however, degrade the performance of the cooler.

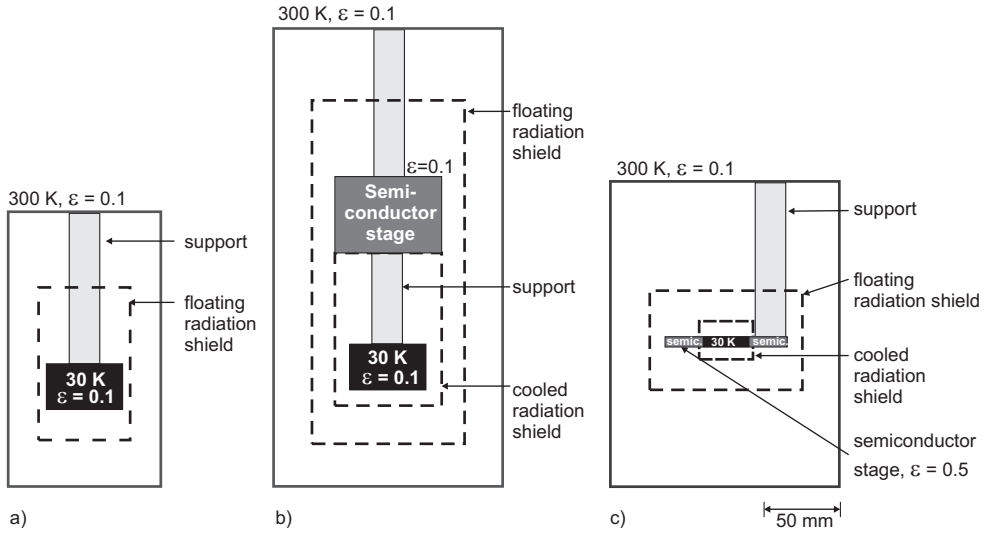

Figure 2.2: Schematic lay-out and dimensions for configurations with: (a) semiconductors at room temperature (b) cooled semiconductors, data transport via coaxial lines or optical fibre (c) cooled semiconductors, data transport by a stripline. Emissivities ϵ = 0.03 were taken for the radiation shields and ϵ = 0.1 for the support structures.

The Wiedemann-Franz-Lorenz (WFL) law [12] states that, for metals and alloys, the temperature behaviour of the thermal conductivity λ and the electrical conductivity σ are coupled:

$$\frac{\lambda}{\sigma} = LT \tag{2.2}$$

Here, T is the absolute temperature and L the Lorenz constant. Hence, application of wires with a low thermal conductivity reduces the thermal load but increases the electrical losses.

For power supply lines, resistive wire can be used. The total thermal load was estimated using a 1-D finite element model that also includes dissipation and radiation, similar to the work of Hanzelka [13]. The temperature dependent thermal and electrical conductivity data were taken from Cryodata [14]. The estimated thermal load to the superconductor stage due to the power supply lines is for all three configurations smaller than 4 mW. For this calculation, it was assumed that manganine wire with thicknesses smaller than 0.25 mm, wire lengths of 20 cm, an emissivity ϵ = 0.1, and a supply voltage of 1 V will be taken. For the semiconductor stage, application of 10 pairs of manganine wire with a thickness of 2.0 mm was assumed. This resulted in a heat load of 80 mW when the semiconductors are cooled

to 150 K and 100 mW when cooled to 80 K. Further reduction of the heat load can be achieved by optimisation of wire lengths, diameters, and materials.

Both the thermal load and the electrical loss should be minimised for electrical high-frequency data transport lines. These two requirements contradict according to the WFL-law (equation (2.2)). The remainder of this section discusses the heat leak through coaxial lines, optical fibres, and striplines, respectively.

Coaxial lines

The optimum design for coaxial lines results from a careful consideration of geometry and composition of inner conductor, dielectric and outer conductor for the considered signal frequency. If the temperature dependencies of the thermal conductivities of these three parallel conductors differ, transversal heat flows can occur that increase the effective thermal conductivity of the line. In addition, the thermal contact resistance between the layers might vary over the length of the line. Therefore, heat load estimates were, as far as available, based on measurement results from literature.

Wedenig *et al.* [15] measured heat load and electrical loss of some commercially available coaxial lines. In these measurements they corrected for radiation and they assumed that dissipation was negligible. For this situation in which only conduction plays a role, they defined a useful figure of merit FOM [dB·W]:

$$\mathrm{FOM} = A_l \cdot A \int_{T_L}^{T_H} \lambda(T) dT \tag{2.3}$$

Here, A_l is the attenuation per unit length. Contrary to most other figures of merit, this one should be as small as possible. The results for a selection of their cables are summarised in table 2.1 and the overview was extended with cryogenic RF cables from other sources [7, 16–18].

The electrical loss for all coaxial cables is considered at room temperature, as only limited data are available at lower temperatures. If conductor loss is the dominant loss source in the coaxial line, which is roughly the case up to several GHz [15, 17], the losses become lower at lower temperatures as the electrical resistivity decreases [12]. The given values are then a worst case estimate.

The AMTEL cable [17] and the Keycom ULT3-cable [18], which were especially designed for use in a cryogenic environment, have the lowest figures of merit. The AMTEL cable has a very thin outer conductor, 5 μm, only a few times the skin depth of copper at GHz frequencies because a thicker layer does not decrease the electrical

Type	**AN50085** [15, 19]	**UT-20-SS** [15, 20]	**AMTEL** [17]	**TRW** [16]	**ULT3** [18]
Configuration					
inner conductor material	SCW	SPCW	SPCW	Cu	SBC
inner cond. O.D. [mm]	0.51	0.11	0.51		0.51
dielectric material	PTFE	PTFE	PTFE	Kapton	PTFE
dielectric mat. O.D. [mm]	1.68	0.38	1.68		1.68
outer conductor material	304SS/Cu	304SS	5 μm Cu	Cu	304SS/Cu
outer cond. O.D. [mm]	2.16	0.51	1.68		2.16
Attenuation [dB/m]	3.0	23[a]	5[b]	11	2.9
Conduction [Wm]					
30 - 300 K	0.49[c]	0.0080[c]	0.005[d]	0.0092[e]	0.015[f]
30 - 150 K	0.19[c]	0.0032[c]	0.002[d]	0.0051[e]	0.008[f]
150 - 300 K	0.30[c]	0.0048[c]	0.003[d]	0.0041[e]	0.007[f]
FOM [dB·W]					
30 - 300 K	1.5	0.18	0.03	0.10	0.043
30 - 150 K	0.57	0.07	0.01	0.06	0.023
150 - 300 K	0.90	0.11	0.02	0.05	0.020

a. Estimate based on 1 GHz data from [15] and $\sqrt{\nu}$ behaviour of losses [15, 17].
b. Estimate based on 2 GHz data from [17] and $\sqrt{\nu}$ behaviour of losses [15, 17].
c. Estimate based on extrapolation of measured conduction integrals from [15].
d. Estimate based on extrapolation of data from [17] assuming the temperature dependent behaviour as measured by [15].
e. Conduction integral calculated from [14] with RRR=60.
f. Estimate based on extrapolation of heat load data supplier.

Table 2.1: RF coaxial lines: configuration, attenuation at 15 GHz, heat load and figure of merit. SCW = silvered copper - clad steel wire, SBC = silvered beryllium copper wire, SPCW = silver plated copper - clad steel wire, PTFE = polytetrafluorethylene (Teflon), SS = stainless steel, Cu = copper.

loss but does increase the thermal load. The ULT3 cable has a lower electrical loss at the cost of a larger heat load. TRW has manufactured a prototype of a flexible ribbon cable, especially suited for a large number of RF lines to a cryogenic device [16]. The prototype was one inch wide and carried 127 signal lines. The dielectric, consisting of a 50 μm thick polyimide film, was coated on both sides with 0.6 μm thick copper ground planes. The signal lines were positioned inside the dielectric and were each 76 μm in width and 4 μm in height. The heat load in the table is for the total of 127 lines. The FOM for a single line is roughly one order of magnitude lower than that of the AMTEL and ULT3 cables and therefore such a cable is a promising option for data transport on short distances. The specifications of the AMTEL cable were used to estimate the load of the THz demonstrator, as this cable has a low FOM and

cables with similar properties are commercially available.

The effect of radiation was included by applying the 1-D model. Assuming a length of 20 cm and an emissivity of ϵ = 0.1, the heat load to the 30 K stage for a single coaxial line is 2.9 mW when the hot end of the wire is at 80 K, 9.6 mW when at 150 K and 29 mW when at room temperature.

Optical fibres

The thermal load for an optical fibre made out of quartz glass with a length of 20 cm, a diameter of 125 μm and an emissivity of ϵ = 0.1 between several temperature stages has been calculated. The largest heat load is 0.3 mW for the 30 K stage when the superconductors are operated at room temperature.

Striplines

At NIST, work has been done on striplines on flexible substrates [21]. They applied signal and ground lines with a height of 35 μm and a total cross-sectional area of $1{\cdot}10^{-7}$ m^2. These lines had a loss of 4.7 dB/m at a driving frequency of 16 GHz. As the length between the two temperature stages is small, dissipation and radiation are negligible compared to conduction and equation (2.1) applies. The heat load for copper lines of 2 cm is 120 mW for a temperature difference of 30 - 80 K and 210 mW for 30 - 150 K. A material with a lower electrical conductivity results in a lower load. Application of e.g. CuNi (90-10) reduces the heat load with about a factor 10, but will also increase the electrical loss. Note that the TRW cable has a roughly 100 times smaller leak and is also an alternative to this design.

2.3.4 Thermal load caused by support structure

The lay-out of the support structure strongly depends on the selected cooling system. Besides, the construction of the cooler itself can possibly be used to support the electronics boxes. This makes it difficult to provide a realistic estimate of the thermal load originating from the support structure. As an illustration, calculations have been done on a supporting tube.

To limit the conduction, a material with a large yield strength and a low thermal conductivity is preferred. Engineering composites, like e.g. epoxies reinforced with fibres of glass, carbon, Kevlar, and glasses are then the best options [7]. For the present estimate, the material G10 (FR4), an epoxy reinforced with glass, was chosen. A thickness of 1 mm and an outer diameter of 20 mm was taken. The length was

chosen at 10 cm to support the semiconductor stage and 6 cm for the superconductor stage. When the semiconductors are at room temperature, a support with a length of 10 cm was assumed. The thermal heat load was again calculated with the 1-D model, assuming an emissivity ϵ = 0.1. The heat load to the superconductor stage varies from 17 mW for a temperature of the semiconductor stage of 80 K to 110 mW for room temperature operation. The load to the semiconductor stage is about 0.2 W.

2.3.5 Thermal load caused by residual gas molecules

The residual gas molecules in the vacuum space conduct heat from the hot surface to the cold stage. If the pressure is low enough, the gas will be in the molecular regime. The mean free path of the molecules is larger than the characteristic dimensions of the system and the individual molecules carry the heat from wall to wall [22]. The heat transferred by molecules impinging to the wall with temperature T_i to a unit area is [22]:

$$\dot{Q}_{molecules} = \alpha \frac{\gamma + 1}{\gamma - 1} \left(\frac{R}{8\pi M T_i} \right)^{\frac{1}{2}} p(T_i - T_s) \tag{2.4}$$

The accommodation coefficient α accounts for an incomplete energy transfer between molecule and wall. This coefficient depends on the type of gas and on the surface. T_s is the temperature of the cold surface, R is the molar gas constant, M the gas mole mass and γ the specific heat ratio. The heat load through conduction scales linearly with the pressure p.

The pressure should be set at such a low value, that the contribution of the gas conduction to the total heat load is insignificant. A maximum heat load of 10 mW for the superconductor stage was chosen. In cryogenic vacuum systems, the most relevant gases are diatomic (O_2, H_2, N_2, CO [23]), so γ=$\frac{7}{5}$ [24]. In general, H_2 gives the largest contribution to the heat conduction as this is the dominant gas component in cryogenic vacuum systems [22] and has a relatively low mole mass. For H_2 the accommodation coefficient is roughly 0.5 [22]. For the temperature of the impinging gas, the shield temperature was used. With dimensions from figure 2.2, it turns out that the pressure should be below 3 mPa. It is not straightforward to maintain such a pressure for the desired lifetime [7]. For the other configurations, the heat load to the superconductor stage is even lower because of the cooled semiconductor stage. The heat loads to the semiconductor stage are negligible compared to the dissipation of the CMOS.

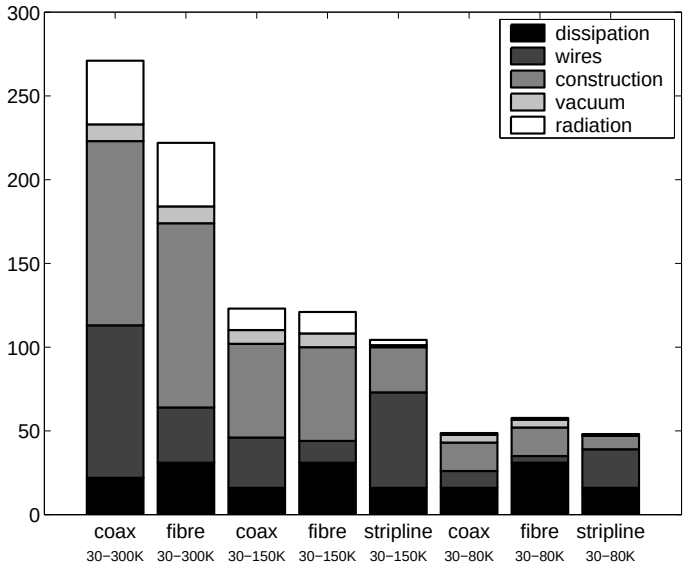

Figure 2.3: Heat load for the superconductor stage for 8 different configurations of the THz ADC demonstrator.

2.4 Cooling power requirements

The heat load estimates for the 30 K stage are summarised in figure 2.3. When the semiconductors are operated at room temperature, the total heat load to the superconductor stage is about 250 mW. The largest contribution is due to the support structure. Options to reduce this load are decreasing the A/l-ratio, or by fixing the electronics boxes by low-conductivity wires like Kevlar. It is even more attractive to use the cooler itself to support the electronics boxes. The use of a fibre instead of a coaxial line is attractive as the load due to additional amplification at the 30 K stage is compensated by a severe reduction in the load through the data transport line.

When the semiconductors are cooled to 150 K, the total load reduces to about 100 mW. Now, there is hardly a difference in load between application of a coaxial line or a fibre. The reduction in heat conduction through the signal line when a fibre is applied is counteracted by the additional load because of the larger amplification. When both stages are on one substrate, the largest contribution to the heat load is caused by conduction through the striplines. This can be reduced by application of a TRW-like flatband cable. When the semiconductors are cooled to 80 K, the thermal load reduces to about 50 mW. Application of a fibre now even results in a larger total load compared to the use of coaxial lines. Also here, application of a TRW-like cable

$T_{\text{semiconductor stage}}$ [K]	Heat load [W]	
	superconductor stage	semiconductor stage
300	0.25	-
150	0.10	14
80	0.050	15

Table 2.2: Heat load requirements for the cooling power of the THz ADC demonstrator set-up. The superconductor stage is at 30 K.

can further reduce the load for the situation that both stages are positioned onto a single substrate.

The total heat load for the semiconductor stage is 14 W when cooled to 150 K. This increases to 15 W when the semiconductors are cooled to 80 K because of the larger temperature difference with the environment. The differences in cooling load between the three configurations are small. The largest contributions originate from dissipation of the CMOS devices (11 W) and from the wiring (2-3 W).

2.5 Conclusions

Three configurations were identified as options to realise the THz ADC demonstrator. These configurations differ in the way high-speed data is transported from the superconductor stage to the semiconductor stage: by coaxial lines, by an optical fibre or by striplines. The superconductor stage will be operated at 30 K. The temperature of the semiconductor stage affects the performance of the semiconductors, the efficiency, mass, and size of the cooler and the heat load to both stages. It was assumed that the semiconductors are operated between 80 K and 150 K, or at room temperature. The heat loads to both the superconductor and the semiconductor stage are summarised in table 2.2. These were estimated based on simple assumptions for the lay-out of the system and standard techniques to reduce the thermal load.

When the semiconductors are operated at room temperature, it is attractive to use an optical fibre from the viewpoint of cooling load. There are no significant differences in the load to the superconductor stage between the three configurations when the semiconductors are cooled. Optimisation of the set-up can reduce the cooling load further once more details about the set-up become available. Attention points are reduction of the load caused by the high-speed data wires and through the support structure. For the semiconductor stage, the total load is 14 - 15 W and is dominated by dissipation.

References

[1] Personal communication with the partners of the THz-project. MESA+ research institute, University of Twente, PO Box 217, 7500 AE, Enschede, The Netherlands, http://www.mesaplus.utwente.nl.

[2] KryoTech, Inc., 2547 Morningside Drive, West Columbia, SC 29169, USA, http://www.kryotech.com.

[3] e.g., Amuneal Manufacturing Corp., 4737 Darrah Street, Philadelphia, PA 19124, USA, http://www.amuneal.com.

[4] J. Vrba. Multichannel SQUID biomagnetic systems. In H. Weinstock, editor, *Applications of superconductivity*, volume 365 of *NATO ASI Series E: Applied Sciences*, pages 61–138. Kluwer Academic, Dordrecht, The Netherlands, 2000.

[5] Personal communication with E. Wikborg, Ericsson, Sweden, 2001.

[6] A/D converter in superconductor-semiconductor hybrid technology, project funded by the European Commission under contract number IST-2001-33468 (Super-ADC), http://www.super- adc.org.

[7] H. J. M. ter Brake. *Cooling and packaging of RF components*, chapter 11, pages 271–304. Microwave superconductivity (NATO-ASI). Kluwer Academic Publishers, Dordrecht, The Netherlands, 2001.

[8] A. Bejan. *Heat transfer*. Wiley, New York, 1993.

[9] H. J. M ter Brake and J. Flokstra. Computer aided cryostat design in Twente: recent developments. In *ICEC 12*, Southampton, UK, 1988.

[10] R. Barron. *Cryogenic systems*. McGraw-Hill, USA, 1966.

[11] J. G. Weisend II (Ed.). *Handbook of Cryogenic Engineering*. Taylor & Francis, USA, 1998.

[12] R. P. Reed and A. F. Clark. *Materials at low temperatures*. Am. Soc. of Metals, 1983.

[13] P. Hanzelka. Current leads in vacuum space of cryogenic systems. *Cryogenics*, 39:955–961, 1999.

[14] Cryodata Inc., P.O. box 558, Niwot, CO 80544, USA, http://www.cryodata.com.

[15] R. Wedenig, Ch. Knoblauch, and T. O. Niinikoski. RF transmission line for cryogenic applications. *Cryogenics*, 38:239–245, 1998.

[16] T. S. Tighe, G. Akerling, and A. D. Smith. Cryogenic packaging of multi-GHz-electronics. *IEEE transactions on applied superconductivity*, 9(2):3173–3176, 1999.

[17] H. Kubota and H. Takeuchi. Low thermal leakage coaxial cable for HTS device. *IEEE transactions on applied superconductivity*, 9(2):3117–3120, 1999.

[18] Keycom Corp., 3-40-2 Minamiotsuka, Toshima-ku, Tokyo 170-0005, Japan, http://www.keycom.co.jp.

[19] Precision tube Company, Coaxitube Division, 620 Naylor Mill Road, Salisbury, MD 21801, USA. http://www.precisiontube.com.

[20] Uniform tubes Inc, Micro-coax line, P.O. Box 91, West Point, PA, 19486, USA. http://www.microstock-inc.com.

[21] J. H. Plantenberg. Flip-chip-on-flex technology for voltage standard applications. External training report NIST, Boulder, CO, USA/University of Twente, Enschede, the Netherlands, 2001.

[22] A. Roth. *Vacuum technology*. Elsevier Science, Amsterdam, 1990.

[23] P. della Porta. Gas problem and gettering in sealed-off vacuum devices. *Vacuum*, 47:771–777, 1996.

[24] D. V. Schroeder. *An introduction to thermal physics*. Addison Wesley Longman, 1999.

Chapter 3

Cryocooler survey

3.1 Introduction

In the process of developing cryocooler technology and market potentials, from time to time cryocooler surveys were presented [1–6]. The most recent survey with a wide coverage was prepared on CD by Nichols Research, sponsored by the Naval Research Laboratory (NRL) [5, 7]. Although the database is a very rich and user-friendly source of cooler information (154 coolers of 36 suppliers), it appeared difficult to transform the data into useful trend lines. The graphs presented in Reference [5] contain too much scatter in this respect. Therefore, we decided to generate a new cryocooler database and to investigate trends. The objectives were twofold. Firstly, we wanted to put up-to-date cryocooler specifications in a database and secondly, we aimed to derive trend lines. This information would not only be useful for the THz project, but also for other projects. In our survey, we started with the data from the above-mentioned NRL-Nichols survey and added any further information that we could find on the Internet. All suppliers were approached with the specific data that we had on their coolers, and they were asked to update this. Thus we have compiled a database of 235 cooler configurations from 32 suppliers. We explicitly tried to get data for the operating temperatures 4 K, 10 K, 20 K, 40 K, and 80 K. Although a few other coolers are included, we primarily focused on cryocoolers with cooling powers below some tens of watts. In this chapter, the state-of-the-art of these cryocoolers is reviewed and trends are discussed. The relevant parameters in this respect are cooling performance (discussed in section 3.2), mass and size (section 3.3), cost (section 3.4), reliability and lifetime (section 3.5). Trend lines for these parameters were derived and they are shown in section 3.6. Six cooler types are

distinguished in this study: Gifford-McMahon (GM), Stirling, Stirling-type or high-frequency pulse tube, GM type or low-frequency pulse tube, throttle type (i.e., fluid expansion over a flow restriction), and reversed Brayton (expansion over a turbine). A more detailed discussion on the database was published elsewhere [8]. The chapter concludes with a discussion on the cooler characteristics that can be expected for the THz demonstrator.

3.2 Cooling performance

Various ways of expressing the performance of a cryocooler exist and the definitions are confusing in this respect. A cooler lifts heat $\dot{Q}_C$ from a cold reservoir at temperature T_C at the expense of an input power P_{in} at a heat sink temperature T_H. Following common practice in thermodynamics, the coefficient of performance (COP) is defined as:

$$COP = \frac{\dot{Q}_C}{P_{in}} \tag{3.1}$$

Often also the specific power is used defined as COP^{-1}. The efficiency of a cooler is usually quoted as the ratio of the actual cooler COP to that of the ideal Carnot cycle:

$$\eta = \frac{COP_{cooler}}{COP_{Carnot}} \tag{3.2}$$

with

$$COP_{Carnot} = \frac{T_C}{T_H - T_C} \tag{3.3}$$

The non-ideal performance of a cooler is caused by various loss mechanisms such as conductive heat losses along the cooler and shuttle heat losses inside it. Relative to the required heat lift Q_C, these losses increase as the operating temperature is lowered and also when Q_C gets smaller. As a result, one may expect the percent-Carnot efficiency to be smaller at lower operating temperatures. Furthermore, at a given operating temperature, one may expect the efficiency to improve as Q_C is increased.

In order to compare the different coolers in our database in a well-founded manner, we transformed all data to the operating temperatures 4 K, 10 K, 20 K, 40 K, 80 K, and to a heat sink temperature of 300 K. Some suppliers gave specifications at slightly different temperatures such as 4.2 K or 77 K, or a heat sink at 290 K. These data points were corrected via the Carnot COP as given by equation (3.3). Data that deviated too much, e.g. 60 K performance, was not included at this point of the study.

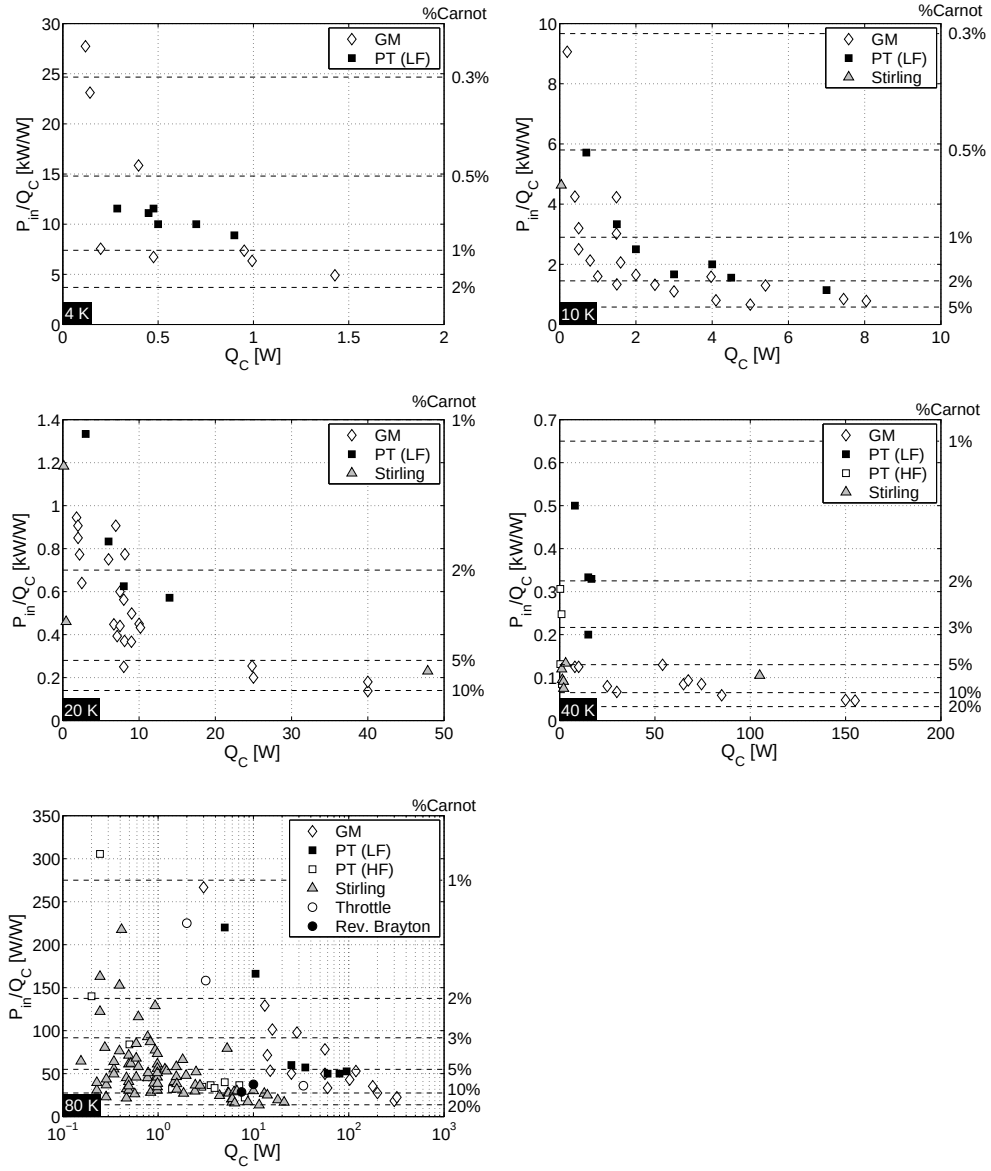

Figure 3.1: Specific power versus cooling power at 5 operating temperatures.

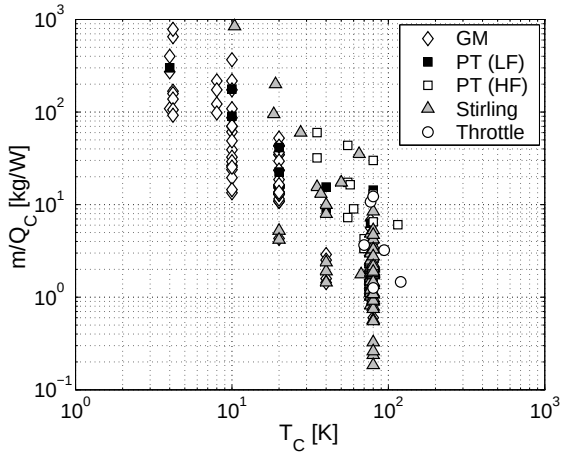

Figure 3.2: Mass per unit of cooling power versus operating temperature.

The resulting specific powers versus cooling powers are depicted in figure 3.1. As expected, a lower operating temperature gives a lower performance and at high values of Q_C the specific power tends to level off. At the lower temperatures, there is no dramatic difference between the various cooler types in terms of efficiency. At 80 K, however, a distinct difference shows up between two categories of coolers. On the one hand, coolers for the 1 W range (Stirling and Stirling-type pulse-tube coolers) and on the other hand, coolers for the 10 W-and above- range (GM and GM-type pulse-tube coolers). Below about 10 W, the former category has a much better performance than the latter. This higher performance in the 80 K range was probably driven by the demands from the infrared community and by the requirements for the HTS microwave filter systems that are being proposed for use in wireless communication base stations.

3.3 Mass and volume

The database contains mass and volume data of 153 coolers. For this data set, a linear fit was made for the cooler mass as a function of the volume. This fit corresponds to a ”cooler density” of 0.8 kg/liter. The smaller Stirling coolers are more compact, however: 1.1 kg/liter [8]. Figure 3.2 shows the mass per unit of cooling power versus the operating temperature. It turns out that Stirling coolers are relatively light, whereas high-frequency pulse-tube coolers are relatively heavy. Relating mass to

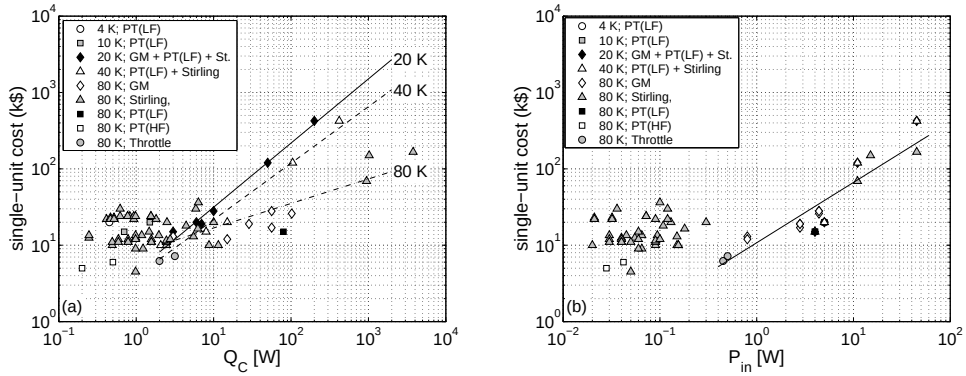

Figure 3.3: (a) Single-unit cost versus cooling power. Trend lines correspond to equation (3.6). (b) Single-unit cost versus input power. The straight line shows the trend for P_{in} according to equation (3.5).

cooling power and operating temperature, a fair fit was derived between these three parameters [8]:

$$m = \alpha(T) Q_C^{\beta(T)} \qquad \alpha(T) = 157 e^{-0.0533T} \qquad \beta(T) = 0.009T + 0.1275 \quad (3.4)$$

with mass m in kg, T in K, and Q_C in W.

3.4 Cost

The price of a cooler is determined by a number of factors. Besides political and economical factors, important parameters are the required performance (cooling power, operating temperature), the number of coolers that is needed and the maturity of the technology. The relation between cost and performance is illustrated in figure 3.3, based on 83 coolers in the database. For input powers above 400 W, a trend can be recognised as:

$$cost(k\$) = 10.78 P_{in}(kW)^{0.79} \quad (3.5)$$

When considering cost versus cooling power, the operating temperature has to be included. Trend lines can be defined for 20 K, 40 K, and 80 K, although the 80 K data contains a lot of scatter. These trends are included in figure 3.3, and are useful

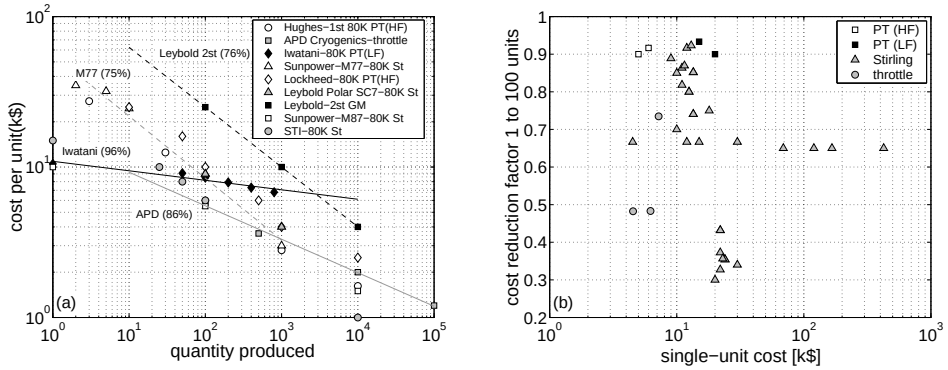

Figure 3.4: (a) Learning curves of nine coolers; STI data are from [9]; Sunpower M87 from database; Leybold data [10]; other data [11]. (b) Reduction in cost per unit for 100 units as compared to a single unit.

above a cooling power of about 2 W:

$$\begin{aligned} cost(k\$) &= 4.55 Q_C(W)^{0.84} \quad \text{T = 20 K} \\ cost(k\$) &= 3.93 Q_C(W)^{0.74} \quad \text{T = 40 K} \\ cost(k\$) &= 8.03 Q_C(W)^{0.32} \quad \text{T = 80 K} \end{aligned} \tag{3.6}$$

The cost of small-power coolers does not appear to depend on required cooling power or input power. One can imagine that the required lifetime also determines cost. This, however, appears not to be the case either [8].

The usual way to display the effect of the quantity produced on the unit cost of an item is in a so-called learning curve. The learning rate (LR) indicates how the cost is reduced when the production is doubled. For instance, an 80% learning rate means that the cost per unit drops to 80% if the quantity manufactured doubles. Learning curves of nine coolers are depicted in figure 3.4a, with four trend lines included. Except for the Iwatani pulse-tube cooler, the learning rates are between 75% and 85%. This learning-rate range seems to be valid for a wide variety of industrial products [8]. In practice, the learning rate is not a smooth curve as suggested by figure 3.4a. The major cost reductions follow revisions of cooler designs and improvements and automations of the manufacturing processes. Such a redesign process can result in a dramatic cost reduction and a step in the learning curve [9, 12, 13].

In our database, cooler prices are included for single units and lots of 100. The reductions in cost per unit for 100 units as compared to a single unit are depicted in

figure 3.4b for a dataset of 67 coolers. The average reduction to 0.64 of the single quantity price corresponds to a learning rate of only 93.5%. This reduction is quite modest. For comparison, a learning rate of 80% would imply a cost reduction to 0.23 of the unit price due to a production increase by a factor of 100.

3.5 Reliability and lifetime

There is much confusion between the terms ”lifetime” and ”reliability”. Often the word ”reliability” is used to imply that a cryocooler has a long operating ”lifetime” but, in this use, it has no quantitative meaning. The term ”lifetime” is frequently used by the supplier as the period of time that the cooler is guaranteed to operate according to the specifications. This lifetime does not mean that the cryocooler will not fail during the specified period of time; the cooler will have a finite probability of failing but, in general, the supplier is willing to replace or repair any defective cryocooler, at his expense. Reliability refers to that failure probability.

The rate at which devices under test fail is denoted by the failure rate λ(t): the number of failures per unit of time, normalised to the number of devices that is still operating at time t, see e.g. [14–16]. A typical failure rate curve is given in figure 3.5a, which due to its shape is often called the ”bathtub curve”. Early defects, causing ”infant mortality”, arise during manufacture and can be detected and removed from shipment before some predetermined number of operating hours. After shipment, most of the coolers will operate without problems and only a small number will fail because of random events (e.g. electrical damage). We assume these events to occur randomly over all period, and as a result the failure rate is constant in this period. At some point in time, wear-out mechanisms will occur and become more and more important as time evolves. In contrast to random events, wear-out will affect all coolers, e.g. wear-out of seals or leakage of helium. The pace at which these mechanisms work may vary from cooler to cooler, but all coolers suffer from this ”wear-out”. The end-of-life occurs when wear-out starts to dominate over the random defects. Usually at that point, the failure rate rapidly increases. Thus lifetime is related to the length of the random-event period, whereas the reliability is related to the failure rate in that period.

We assume that the cooler operation by the user is started after the cooler has survived the ”burn-in” during the ”infant mortality” phase. Then, in the first period of operation, λ is constant. The mean-time-to-failure (MTTF) evaluated in that period is equal to $1/\lambda$, and can simply be translated into the cumulative number of operating hours, divided by the number of failures that have occurred [8]. Two

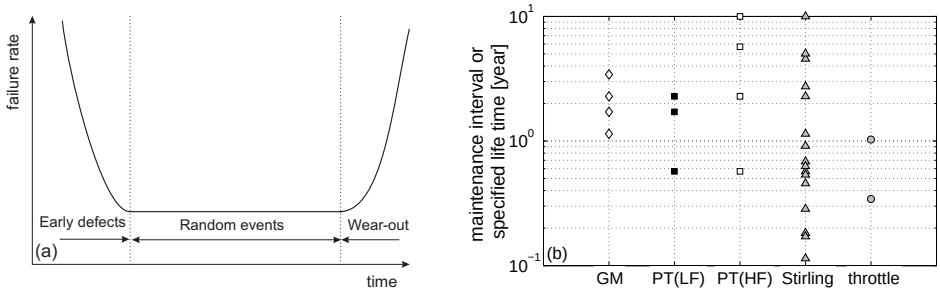

Figure 3.5: a. Typical failure rate curve. b. Distributions of maintenance intervals or specified lifetimes per cooler type.

important remarks have to be made at this point. Firstly, this MTTF should not at all be interpreted as ”the lifetime”. As discussed above, lifetime is determined by wear-out mechanisms and not by the random defects. It is far better to relate the ”random-events MTTF” to reliability. The chance that a cooler fails before its specified end-of-life is given as the lifetime divided by that MTTF. For example, in order to establish a cooler reliability of 95% (i.e. 5% failures) for a 5 year lifetime, an MTTF of 100 years (!) has to be realised in the random-events phase. Secondly, the estimates that are made may pertain only to the reliability for a time period less than or of the order of the test duration, and reliability estimates cannot be given for other time periods. For example, a test with 10,000 coolers operated for 1 year with 10 failures yields the same MTTF as a run with 1000 coolers operated for 10 years and 10 failures. But clearly the latter test MTTF is more meaningful since it gives a reliability estimate valid for 10 years instead of only for 1 year.

In our database, data is included on maintenance intervals and specified lifetimes without maintenance. This data is summarised in figure 3.5b for 149 coolers (with lots of coinciding points). The statistics for the different distributions are given in

	GM	PT (LF)	PT (HF)	Stirling	Throttle
Number of coolers	47	11	7	81	3
Average	14,400	15,900	44,700	14,200	7000
Standard deviation	7000	5800	26,300	22,800	3500
Statistical percentage $>$1 year	79%	89%	91%	59%	31%
Statistical percentage $>$5 years	0%	0%	51%	10%	0%

Table 3.1: Statistics in distributions of maintenance intervals or specified lifetimes (numbers are rounded).

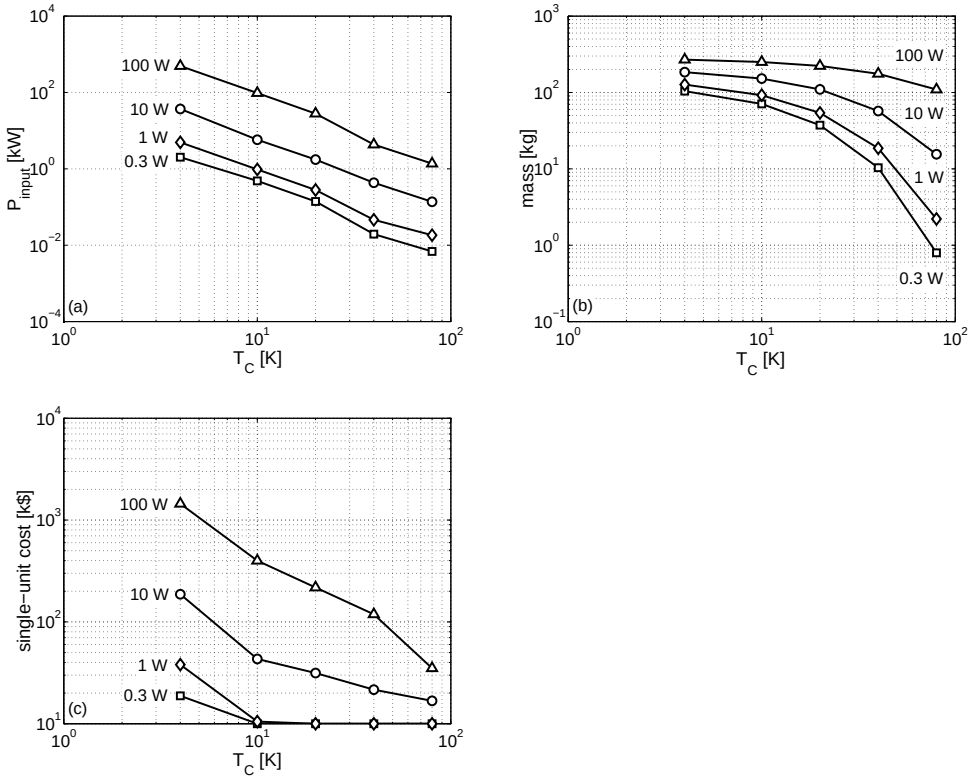

Figure 3.6: (a) Estimated input power versus operating temperature with cooling power as the parameter. (b) Estimated cooler mass versus operating temperature with cooling power as the parameter. (c) Estimated cooler cost versus operating temperature with cooling power as the parameter.

table 3.1. Two Stirling coolers with lifetimes of only 400 hours were included in the statistics but not in figure 3.5b. Obviously, large numbers of coolers are available nowadays with operating times far over 1 year, with special efforts and results in high-frequency pulse tube and Stirling coolers.

3.6 Trend lines

A trend study was performed and the results are summarised in figures 3.6a, b, and c; figure 3.6a depicts the input power versus the operating temperature, with the cooling power as a parameter varying from 0.3 to 100 W. This figure is based on currently

achievable efficiencies as depicted in figure 3.1. The cooler mass is plotted against operating temperature in figure 3.6b, based on equation (3.4). Finally, the cooler cost as a function of temperature and cooling power is given in figure 3.6c. This plot is based on the equations (3.5) and (3.6), with 10 k$ taken as a lower limit. All graphs should be used for estimate purposes only.

3.7 Cooling options for THz

In section 1.1, four cooling options for the THz demonstrator were discussed. In this section, the input power, mass, and cost of these options will be estimated based on the information in the previous sections. The cooling power requirements were discussed in chapter 2 and the results were summarised in table 2.2. The THz system has no extreme requirements with respect to vibrations or electromagnetic interference (section 2.2). Hence, lifetime will be one of the key issues in cooler selection. The cooler for the THz demonstrator should have a lifetime larger than 10 years. Intermediate maintenance is allowed. Coolers with such lifetimes, and even with lifetimes longer than 5 years, are still rare, as can be concluded from table 3.1. However, a growing number of mainly civil applications currently require a lifetime of 5 years or more. Therefore, lifetime is at the moment an important issue in cooler design and it is expected that the number of coolers with long lifetimes will grow rapidly in the near future.

To cool the semiconductor stage, Stirling and Joule-Thomson coolers are attractive as they have the highest efficiencies for the required cooling power at 80 K*, as can be seen in figure 3.1. At low input powers and at 30 K, Stirling and high-frequency pulse tube coolers have the highest COPs.

In cooling option A from section 1.1 the semiconductors are operated at room temperature and only the superconductor stage is cooled. Based on the trend lines from the previous section, the input power of the cooler would roughly equal 38 W, its mass would be about 18 kg and its price about 10 k$.

Cooling option B1 uses separate coolers for the superconductor and the semiconductor stages that each cool from ambient to the desired temperature. When the semiconductor stage is cooled to 80 K, the cooler for the superconductor stage has an input power of roughly 8 W and a mass of about 10 kg. Its price is estimated at 10 k$. The input power for the cooler of the semiconductor stage, when operated

*The survey does not include coolers for temperatures higher than 80 K. Based on the trend lines from the previous section, coolers with a higher efficiency, lower mass, and lower cost can be expected at higher operating temperatures.

at 80 K, is estimated at 210 W, the mass at 22 kg, and its price at 19 k$.

Cooling option B2 uses the cooler of the semiconductor stage also as a precooler for high-pressure gas from room temperature that is used to cool the superconductor stage. As will be set out in chapter 5, the amount of energy the precooler needs to extract from the high-pressure gas is on the same order of magnitude as the cooling power at the superconductor stage. This additional heat load is negligible compared to the load resulting from dissipation and heat leak from the environment. Then, the specifications of the cooler for the semiconductor stage are similar to that of the 80 K cooler from the second cooling option. Estimation of the specifications of the JT expansion loop that is precooled by the semiconductor stage is somewhat more complex. Application of the trend lines from the previous section will result in an overestimate of the mass and cost. From the trend lines, the mass is estimated at about 10 kg when the semiconductors are cooled to 80 K. The additional cost will be some 10 k$. The input power to the JT expansion stage depends on the selected high and low pressures. The required flow depends on these pressures and on the precool temperature. A lower precool temperature increases the amount of enthalpy that is extracted by the precooler and thus the cooling enthalpy as is discussed in chapter 5. Besides, a lower precool temperature also reduces the heat leak from the semiconductor stage to the 30 K stage. This further reduces the required flow. A temperature of 30 K can be achieved with neon with a low pressure of 2.2 bar and with hydrogen gas with a low pressure of 8 bar. A high pressure of 50 bar was taken and a compressor efficiency of 60% with respect to its pV-work was assumed. Application of neon requires a compressor input power of about 27 W when the high-pressure gas is precooled to 150 K whereas an input power of about 3 W is needed when precooled to 80 K. The use of hydrogen gives slightly lower input powers.

Cooling option B3 uses the semiconductor stage as a heat sink for a small cooler that cools the superconducting electronics. Assuming 80 K and a cooler efficiency of 2% of Carnot, 4.5 W is dumped by this small cooler. The first stage cooler then has an input power of about 270 W, a mass of approximately 27 kg, and this unit will cost around 21 k$. Contrary to the second and the third cooling option, the cooling load to the semiconductor stage now increases when the semiconductor stage is operated at 150 K instead of 80 K. The efficiency of a sorption compressor cooler with a Linde-Hampson cold stage rapidly goes down as its heat sink temperature is increased, as is illustrated in figure 3.7. This is only partly compensated by the lower heat leak from room temperature. The database as discussed in the previous sections only considers coolers that are operated from room temperature and cannot be used to estimate the specifications of the second stage cooler that is heat sunk at the temperature of the semiconductor stage. The mass of the sorber beds was therefore estimated with the

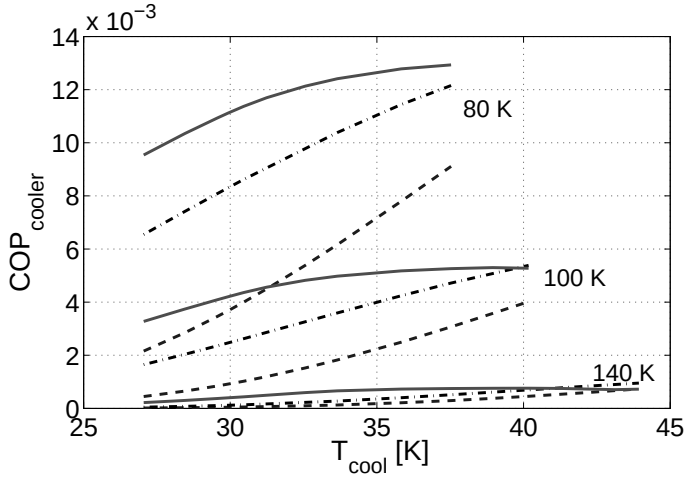

Figure 3.7: Cooler COP as a function of cold-tip temperature for three heat sink temperatures with Saran as the sorber material and neon as the working gas. Dashed lines are for a single-stage compressor, dash-dotted lines for a basic 2-stage compressor and the straight lines are for the two-stage compressor with an internal JT-precooler. External precooling is not applied. The configurations and the calculation method are described in detail in chapter 5.

help of the theory from chapter 5 applied to saran and neon as the working gas. A total mass of about 20 grams seems reasonable. Some additional mass will be needed for the sorber container, tubing, counterflow heat exchangers, and so on, but it seems that this is negligible compared to the mass of the cooler of the semiconductor stage. A single-unit cost of 10 k$ was assumed, the lowest cooler price from the database.

The estimated specifications for the discussed cooling configurations are summarised in table 3.2. Obviously, cooling option A has the lowest input power, price, and cost as in this configuration only the superconductors are cooled. In case the semiconductor stage is cooled to 80 K, the input power, mass, and cost

	option A	option B1	option B2	option B3
P_{input} [W]	38	218	213	270
mass [kg]	18	32	32	27
cost [k$]	10	29	29	31

Table 3.2: Estimated specifications of four cooling configurations for the THz ADC demonstrator. In options B1 to B3, the semiconductor stage is cooled to 80 K whereas in option A the semiconductors are operated at room temperature.

of the cooling system does not differ significantly between the three configurations considered. The values in the table of course only give a rough indication of the specifications that can be expected for the cooler.

The estimated single-unit cost for cooling option A is 10 k$. When the semiconductors are also cooled, this increases to about 30 k$. With a typical learning rate of 80% (see section 3.4), a production of more than 300,000 is needed to achieve a cooler cost of $ 500. When the ADC would be used for UMTS base stations worldwide, such a number is realistic as only in Europe, there is already a potential for about 650,000 base stations assuming that whole Europe will be covered [17]. Unfortunately, installation of these base stations has already started. However, a redesign of the selected coolers can possibly result in a step in the learning curve, thus reducing the number of units that needs to be produced to obtain a price of $ 500. A production of over 11,000 is needed to reduce the single-unit cost from 10 k$ to $ 500. The masses of the cooling configurations with cooled semiconductors exceed 20 kg, whereas the requirement was set to about 10 kg. This aspect should therefore also be an attention point in the redesign process. Based on the trend lines from the previous section, for the first three cooling options, coolers with a higher efficiency, lower mass, and lower cost can be expected when the semiconductor stage is cooled to temperatures higher than 80 K. An increase of the operating temperature of the semiconductor stage may therefore be attractive. The requirements for the cooling system as specified in section 2.2 strongly depend on the application of the ADC. Changes to these requirements influence the input power, mass, and cost of the cooling system.

References

[1] J. G. Daunt and W. S. Goree. Miniature cryogenic refrigerators. Report office of Naval Research, contracts Nonr-263(70) and N00014-67-C-0393, July 1969.

[2] A. H. Crawford. Specifications of cryogenic refrigerators. *Cryogenics*, 10:28–37, 1970.

[3] J. L. Smith Jr, G. Y. Robinson Jr, and Y. Iwasa. Survey of the state-of-the-art of miniature cryocoolers for superconducting devices. NRL Memorandum Report 5490, Naval Research Laboratory, Washington DC, 1984.

[4] T. R. Strobridge. Cryogenic Refrigerators - An updated Survey. Technical Note 655, National Bureau of Standards, 1974.

[5] J. L. Bruning, R. Torrison, R. Radebaugh, and M. Nisenoff. Survey of cryocoolers for electronic applications (C-SEA). In R. G. Ross Jr, editor, *Cryocoolers*, volume 10, pages 829–835, New York, 1999. Plenum Press.

[6] D. S. Glaister, M. Donabedian, D. G. T. Curran, and T. Davis. An overview of the performance and maturity of long life cryocoolers for space applications. In R. G. Ross Jr, editor, *Cryocoolers*, volume 10, pages 1–20, New York, 1999. Plenum Press.

[7] Naval Research Laboratory "Cryo Cooler Database Version 1.0, April 1999". Prepared by: Nichols Research, Albuquerque, NM, USA.

[8] H. J. M. ter Brake and G. F. M. Wiegerinck. Low-power cryocooler survey. *Cryogenics*, 42:705–718, 2002.

[9] V. Loung, A. O'Baid, and S. Harper. Path to low cost and high reliability Stirling coolers. In R. G. Ross Jr, editor, *Cryocoolers*, volume 9, pages 97–108, New York, 1997. Plenum Press.

[10] H. A. Häfner. Kryorefrigeratoren, eine wichtige Hilfskomponente für Supraleiteranwendungen Status und Ausblick. In *Fachtagung Supraleiting, eine Komponente zukünftiger Energieversorgung?* VWEW-Energieverlag, February 2001.

[11] M. Nisenoff. Personal communication, April 2002. Data also presented at Cryoelect. Workshop, February 1999.

[12] R. Z. Unger, R. B. Wiseman, and M. R. Hummon. The advent of low cost cryocoolers. In R. G. Ross Jr, editor, *Cryocoolers*, volume 11, pages 79–86, New York, 2001. Plenum Press.

[13] T. Nast. Potential for low cost cryocoolers incorporating pulse tube and linear motor compressor technology. Workshop on Military & Commercial Applications for Low-Cost Cryocoolers, M-Calc 3, October 25-26, 2001. Updated in personal communication, April 2002.

[14] A. E. Green and A. J. Bourne. *Reliability technology*. John Wiley & Sons, London, 2nd edition, 1977.

[15] F. R. Nash. *Estimating device reliability: assessment of credibility*. Kluwer Academic Publishers, Dordrecht, 1993.

[16] H. F. Martz and R. A. Waller. *Bayesian reliability analysis*. John Wiley & Sons, New York, 1982.

[17] Personal communication with A.L.J.M. Wiegerinck, TNO Informatie- en communicatietechnologie, Delft, The Netherlands, January 2005.

Chapter 4

A 30 K glass-tube cooler

4.1 Design of a glass cooler for reaching 30 K

One of the cooling options for the THz demonstrator is to apply a Linde-Hampson (LH) cold stage that is precooled by the cooler of the semiconductor stage. This is cooling option B2 from figure 1.1. The aim is to operate the high-T_c superconducting digitiser at about 30 K. This is in the same temperature range that is required for operating a MgB_2-SQUID [1, 2]. This chapter describes the development of a cooler that is suitable to cool such a SQUID. Such a system can e.g. be used for measuring a magnetocardiogram [3, 4].

A cooler based on the Linde-Hampson cycle seems appropriate to cool a SQUID [4–6]. The cold stage that is used in this cycle has a low vibration level, which is important to limit noise caused by vibrations of the sensor. Such vibrations result in fluctuations in the observed earth magnetic field due to tilting and field gradients. Furthermore, electromagnetic interference caused by the compressor is an important issue. The LH cycle provides an easy way for spatial separation between the compressor and the SQUID. In the work presented here, however, the cooler will be operated in an open-loop with the high-pressure gas supplied from a gas bottle. Conducting elements in the cooler can also cause disturbances because of thermal noise or eddy currents [7]. It was decided to realise the counterflow heat exchangers (CFHXs) and the precooler out of glass. This material was selected because of its relatively low thermal conductivity, reducing the heat load to the cold tip. The CFHXs were realised in a tube-in-tube configuration with the high-pressure gas flowing through the inner tube and the returning low-pressure gas flowing through the annulus, similar to the design of Holland *et al.* [8]. The latter, however, did not need

to apply a precooler. As only the high-pressure gas needs to be precooled, generally the high-pressure and the low-pressure line are split just before the precooler, as was e.g. done by Burger *et al.* [9]. It is, however, also possible to precool the high-pressure gas in the inner tube via the low-pressure gas in the annular space. This is applied in the present work because of its simplicity. The other parts of the system were also made of glass to prevent cracks caused by differences in thermal expansion. Besides, glass is not electrically conducting eliminating a potential noise source for the SQUID. To reach 30 K in a Linde-Hampson cycle, neon and hydrogen can be used (see table 1.1). Neon was selected for safety reasons as the cold stage will be driven in an open-loop configuration. Precooling will be performed by liquid nitrogen. A cryocooler was not used for this purpose because of vibrations and electromagnetic interference.

The next section gives a thermodynamic analysis of the cycle as a whole, the counterflow heat exchangers and the precooler. This information is used for dimensioning the cooler as is discussed in section 4.3. The cooler operation is described in section 4.4. The chapter ends with conclusions on the cooler design.

4.2 Thermodynamic analysis

4.2.1 Cooling cycle

The temperature-entropy (Ts) diagram of the LH cycle for neon with a low pressure of 2.2 bar, a high pressure of 100 bar, and a precool temperature of 77 K is shown in figure 4.1. With the selected low pressure, a cold-stage temperature of 30 K is achieved. The starting point in our cycle is point 2. High-pressure gas is available from a bottle at 100 bar. The isothermal compression from point 1 to 2 is included in the picture to complete the cycle. Between points 2 and 3, the high-pressure gas is cooled in CFHX 1 by the colder low-pressure gas. At point 3, the high-pressure gas enters the precooler which cools the gas to point 4. The gas is further precooled in the second CFHX before the gas is expanded isenthalpically (point 5 to 6). A part of the gas is liquefied and evaporates because of the thermal load. At point 7, gas flows back into the CFHX, cooling down the incoming high-pressure gas. A more thorough discussion on the Linde-Hampson cycle can be found in literature [6, 11, 12].

In a perfect CFHX all enthalpy change at the hot side is taken up at the cold side and there is no heat exchange with the environment. If a perfect CFHX is 100% efficient, the cooling power that is delivered by a Linde-Hampson cycle depends on the mass flow and on the enthalpy difference between the low-pressure and the high-

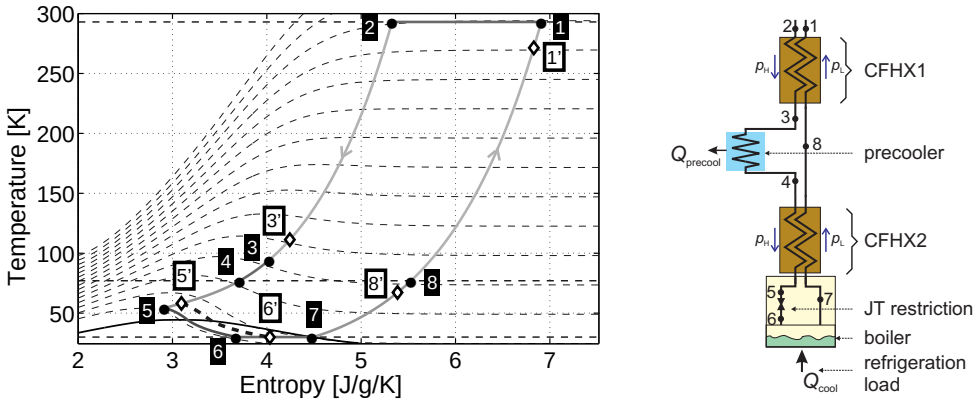

Figure 4.1: (Left) Ts-diagram of neon flowing through a Linde-Hampson cold stage with a low-pressure of 2.2 bar, a high-pressure of 100 bar, and a precool temperature of 77 K. The numbers refer to the points in the diagram on the right-hand side in case of 100% efficient CFHXs. The diamonds illustrate the shift in these points because of inefficiencies in the CFHXs. Gas properties were taken from GasPak [10]. (Right) Schematic overview of LH-cold stage. The numbers refer to the numbers in the Ts-diagram.

pressure gas at the temperature of the precooler (see also section 5.2.2)

$$\dot{Q}_{cool} = \dot{m} T_{cool} \Delta s_{67} = \dot{m} \Delta h_{67} = \dot{m} \Delta h_{48} \tag{4.1}$$

with $\dot{Q}_{cool}$ the cooling power, $\dot{m}$ the mass flow through the cold stage, s the specific entropy, and h the specific enthalpy. The numbers refer to points in figure 4.1. In practice, however, counterflow heat exchangers will not be 100% efficient. The efficiency of a CFHX can be defined as the ratio between the actual amount of enthalpy that is exchanged Δh_{actual} and the amount of enthalpy that is exchanged ideally [11]

$$\eta_{cfhx} = \frac{\Delta h_{actual}}{\Delta h_{ideal}} = \frac{\Delta h_{78'}}{\Delta h_{78}} \tag{4.2}$$

In the cycle from figure 4.1, the ideal amount of enthalpy that is exchanged in CFHX 2 is Δh_{78}. In practice, this will not be achieved and, as a result, the low-pressure gas that flows out of the counterflow heat exchanger has a temperature lower than that of point 8. Inefficiency in this counterflow heat exchanger results in a reduction of the cooling power as can be seen in figure 4.1 [11]. Less enthalpy is exchanged and gas is expanded from a higher temperature, resulting in a smaller fraction of gas that is liquefied. This inefficiency is important in the design of a

CFHX as is discussed in the next section. Note that inefficiency in CFHX 1 can be compensated by the precooler in extracting more enthalpy from the gas.

4.2.2 Model of a CFHX

For a given set of diameters for a tube-in-tube CFHX, the efficiency increases when the CFHX is made longer. The length that is required to achieve a specific efficiency can be determined with the Δh-method [13]. In this approach, the CFHX is divided in small pieces of constant enthalpy Δh. The amount of enthalpy that is exchanged in the CFHX can be determined from the temperature of the incoming high-pressure gas, that of the low-pressure gas, and the required efficiency. Then, the temperatures of the incoming and outflowing high-pressure and low-pressure gas of each infinitesimal element can be derived from the enthalpy at the boundaries of that element. The length of each infinitesimal element can be determined from the heat-transfer area that is needed to exchange the enthalpy Δh

$$\dot{m}\Delta h = \frac{1}{R_{tot}}\Delta T_{lm} \tag{4.3}$$

with R_{tot} the total thermal resistance between the high-pressure and the low-pressure gas and ΔT_{lm} the log-mean temperature difference [14]

$$\Delta T_{lm} = \frac{\Delta T_w - \Delta T_c}{\ln \frac{\Delta T_w}{\Delta T_c}} \tag{4.4}$$

with $\Delta T_w = T_{Hin} - T_{Lout}$ and $\Delta T_c = T_{Hout} - T_{Lin}$. The log-mean temperature difference can be used when the heat capacities of the high-pressure and the low-pressure gas do not vary appreciably along the length of the element and all enthalpy extracted from the high-pressure gas is taken up by the low-pressure gas. The total thermal resistance R_{tot} equals

$$R_{tot} = \frac{1}{\Delta l}\left(\frac{1}{\mathrm{Nu}_i \lambda_i \pi} + \frac{\ln \frac{D_{oi}}{Di}}{2\pi\lambda_w} + \frac{\frac{D_{oo}}{D_{oi}} - 1}{\mathrm{Nu}_{oi}\lambda_o \pi}\right) \tag{4.5}$$

with D_i the inner diameter of the inner tube, D_{oi} the inner diameter of the annulus, D_{oo} the outer diameter of annulus, dl the length of the infinitesimal element, *Nu* the Nusselt number, and λ the thermal conductivity. The subscript i refers to properties of the gas in the inner tube whereas the subscript o refers to properties of the gas in the annulus. The subscript w refers to properties of the wall. We expect maximum Reynolds numbers on the order of 1000, implying laminar flow. The Nusselt number

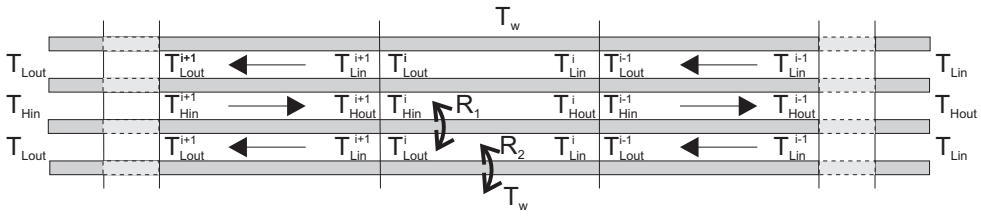

Figure 4.2: Schematic overview of temperatures and thermal resistances in tube-in-tube precooler.

for laminar flow for the inner tube was set to 4.0, the average between the values for uniform wall heat flux (Nu = 4.36) and a uniform wall temperature (Nu = 3.66) [14]. The Nusselt number on the inner surface of the annulus depends on the ratio D_{oi}/D_{oo} and is about 5 for D_{oi}/D_{oo} larger than 0.5. Also here, the average was taken between the values for a uniform wall heat flux and a uniform wall temperature [15].

For a laminar flow, the pressure drop along the lines can be calculated from [14]

$$dp = \frac{C\mu dl}{2\rho A_c D_h^2}\dot{m} \tag{4.6}$$

with C a geometry constant being equal to 64 for the inner tube and 96 for the annulus [14], A_c the cross-sectional area of the flow channel, D_h its hydraulic diameter, μ the dynamic viscosity, and ρ the density of the gas. In the current approach, the pressure drop is considered separately, whereas longitudinal heat conduction through the wall material and radiation are neglected. The resulting design is not necessarily the optimum geometry. Such an optimum design can be obtained by describing all loss sources in terms of entropy generation and minimising the total entropy production as was done by Lerou *et al* [16].

4.2.3 Model of a tube-in-tube precooler

In the tube-in-tube precooler, as schematically depicted in figure 4.2, the outer wall of the annulus is kept at a constant temperature and the log-mean temperature difference method cannot be applied. Therefore, an alternative method to determine the temperature profiles was developed. The tube-in-tube precooler was split in elements that have a fixed size. The temperature profiles were calculated starting from the temperatures at the cold side of the precooler. The temperature of the incoming gas in the low-pressure line T_{Lin} is the temperature of the gas that comes out of the cold CFHX. The temperature of the high-pressure gas that flows out of the precooler can be chosen and is a measure of the efficiency of the tube-in-tube

precooler. The temperatures at the hot end of each infinitesimal element result from the heat balances on both gas lines. When longitudinal heat conduction through the wall material is neglected, the high-pressure gas in the inner tube only exchanges energy with the low-pressure gas in the annulus

$$\dot{m}c_{pH}^{i}\Delta T_{H}^{i} = -\frac{1}{R_1}(T_{Hout}^{i} - T_{Lin}^{i}) \tag{4.7}$$

with c_{pH}^{i} the specific heat of the high-pressure gas, $\Delta T_{H}^{i} = T_{Hout}^{i} - T_{Hin}^{i}$ the temperature difference of the high-pressure gas in the element i, and R_1 the thermal resistance between the low-pressure gas and the high-pressure gas (equation (4.5)). The definition of the temperatures is illustrated in figure 4.2. The gas in the low-pressure line exchanges energy both with the high-pressure gas and with the wall, which is assumed to be at a fixed temperature T_w

$$\dot{m}c_{pL}^{i}\Delta T_{L}^{i} = \frac{1}{R_1}(T_{Hout}^{i} - T_{Lin}^{i}) - \frac{1}{R_2}(T_{Lin}^{i} - T_w) \tag{4.8}$$

with c_{pL}^{i} the specific heat of the low-pressure gas, $\Delta T_{L}^{i} = T_{Lout}^{i} - T_{Lin}^{i}$ the temperature change of the low-pressure gas in the element, and R_2 the thermal resistance between the low-pressure gas and the outer wall of the annulus. The Nusselt number Nu_{oi} now changes as the outer wall of the annulus now has a constant temperature [15]. The number is about 4.5 for D_{oi}/D_{oo} larger than 0.5. The thermal resistance R_2 between the low-pressure gas and the precooler equals

$$R_2 = \frac{1 - \frac{D_{oi}}{D_{oo}}}{\mathrm{Nu}_{oo}\lambda\pi\Delta l} \tag{4.9}$$

with Nu_{oo} the appropriate Nusselt number which is about 4 for D_{oi}/D_{oo} larger than 0.5 [15]. The elements were calculated starting from the cold side of the precooler. This is continued until the calculated temperature in the high-pressure line equals the set temperature for the incoming high-pressure gas. Note that the equations are only valid as long as the high-pressure gas is not liquefied in the precooler, which is true for neon (see figure 4.1).

4.3 Cooler design

4.3.1 Design of the cold CFHX

An important issue in the design of a CFHX is its efficiency. The length that is required to achieve a given efficiency strongly depends on the mass flow, see

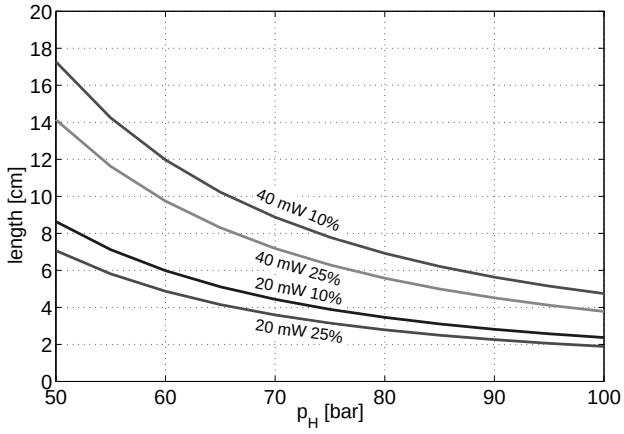

Figure 4.3: Influence of high pressure and accepted loss percentage with respect to the available enthalpy difference at the precooler on the required length of the cold CFHX for neon with a low pressure of 1 bar and inflowing high-pressure gas at a temperature of 78 K.

equations (4.3) and (4.5). The mass flow depends on the amount of cooling power that is needed. The heat load to the 30 K stage was estimated using the same approach as described in chapter 2. The major heat contributions to the 30 K stage result from heat conduction through the copper lines for the SQUID voltage read-out and possibly the conduction caused by residual gas in the vacuum. The heat load from other sources, being heat load through other wires and radiation, is estimated to be smaller than 5 mW. The contribution of radiation is small as the vacuum space around the cold CFHX is surrounded by LN_2. All other wires, e.g. to supply the SQUID bias current and the heater current, that are connected to the cold stage can be out of manganine, resulting in a heat load of a few tenths of milliwatts for each wire. Limitation of the heat conduction through the copper wires to about 10 mW appears realistic by selecting appropriate lengths and diameters. The heat conduction by the residual gas is estimated at 2.7 mW assuming an accommodation coefficient $\alpha = 0.5$ [17] and a vacuum pressure of 10^{-4} mbar. In the molecular regime, the heat load scales with the pressure (see equation (2.4)) and a sufficiently low vacuum pressure is essential. In total, a cooling power of at least about 20 mW is required.

The cold CFHX is the most crucial part in the design as inefficiencies in this CFHX directly reduce the available gross cooling power. From available tube material, the inner and outer diameters of the inner tube were selected as 250 μm and 350 μm. An inner diameter of 530 μm and an outer diameter of 670 μm was chosen for the outer tube. Application of tubes with these dimensions gave acceptable

lengths of the CFHX and an acceptable pressure drop over both the high-pressure line and the low-pressure line. At increasing values of the high pressure, the enthalpy difference between the high-pressure gas and the low-pressure gas at the cold side of the precooler becomes larger. As a consequence, a lower mass flow rate is needed and the CFHX can be shorter. The required length of the CFHX was determined for high pressures ranging from 50 bar to 100 bar. This was done for gross cooling powers of 20 mW and 40 mW. The temperature of the inflowing high-pressure gas was set to 78 K, as is discussed in section 4.3.2. The amount of enthalpy loss that was accepted in the CFHX was related to the enthalpy difference that was available at the temperature of the precooler. Calculations were performed for losses of 10% and 25% of the enthalpy difference at the precooler. Temperature and pressure dependent properties of the gas and the wall were taken from Cryodata software [10]. The required lengths of the heat exchanger are shown in figure 4.3. As expected, higher pressures on the high-pressure side result in shorter lengths of the CFHX. Besides, as the loss percentage is related to the enthalpy difference that is available at the precooler, also the required efficiency of the CFHX reduces. This also results in a reduction of the required length of the CFHX.

In order to keep the possibility open to position the cooler with vacuum space in an external glass cryostat filled with LN_2, the length of the cold CFHX and the precooler should be limited to about 15 cm. A length of 6 cm was selected for the cold CFHX. This leaves some margin with respect to non-idealities like parasitic thermal load to the CFHX or the inner tube being eccentric with respect to the outer tube [15].

4.3.2 Design of the precooler and the warm CFHX

The temperature of the high-pressure gas as it flows out off the tube-in-tube precooler is a measure of the efficiency of the precooler. The closer this temperature needs to be to the temperature of the liquid nitrogen, the longer the length of the precooler that is required. So in order to reduce this length, higher temperatures must be selected. However, a higher temperature of the outgoing high-pressure gas decreases the enthalpy difference that is available for cooling. A temperature of 78 K instead of 77.2 K gives an enthalpy loss of about 2% whereas at 80 K, this loss has increased to 8%. An outflow temperature of 78 K was selected to minimise this loss whereas the required length of the precooler remains acceptable. The efficiency of the warm CFHX determines the temperature of the high-pressure gas that flows into the precooler. The lower the efficiency of the warm CFHX, the longer the precooler needs to be. In principle, one can minimise the total length of the precooler and warm

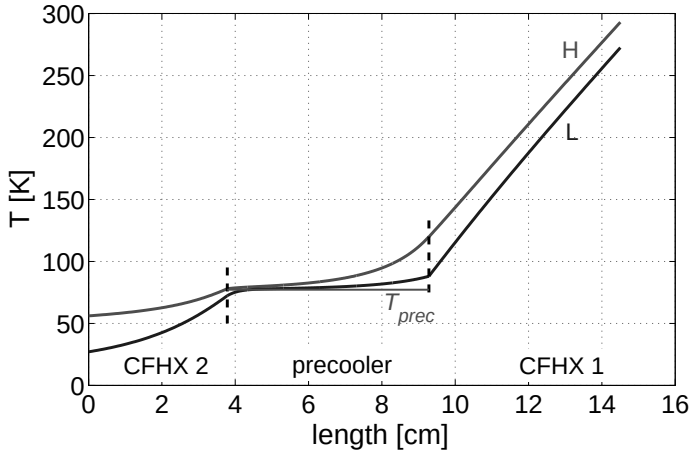

Figure 4.4: Calculated temperature profile in the high-pressure line and the low-pressure line of the tube-in-tube configuration for neon with a low pressure of 1 bar, a high pressure of 100 bar, and a flow of 2.3 mg/s. The efficiency of the warm CFHX was set to 90% whereas that of the cold CFHX was set to 89%. The net cooling power is 40 mW.

CFHX. In practice, however, this is of limited use as the evaporating nitrogen also precools the wall of the warm CFHX. This part of the tube-in-tube-configuration will also act as a precooler, possibly with a somewhat higher wall temperature. Besides, during a measurement, the level of the liquid nitrogen will go down, reducing the active length of the precooler. The temperature of the low-pressure gas that flows into the precooler is determined by the efficiency of the cold CFHX. The temperatures of the high-pressure gas and the low-pressure gas between the warm CFHX and the precooler were determined in an iterative way. The resulting temperature profile for the total system with an efficiency of 90% for the warm CFHX is shown in figure 4.4. The required lengths of the precooler and the warm CFHX resulted as 5.5 cm and 5.2 cm, respectively.

4.3.3 System lay-out

A schematic lay-out of the cooler is shown in figure 4.5. The vacuum chamber and the reservoir for the liquid nitrogen are made of two pieces of glass that are connected with a vacuum flange. This flange consists of two flat glass surfaces with an indium ring in between. The two flat surfaces are pressed onto each other by two screws. The high-pressure gas is supplied from a gas bottle and kept at a constant pressure

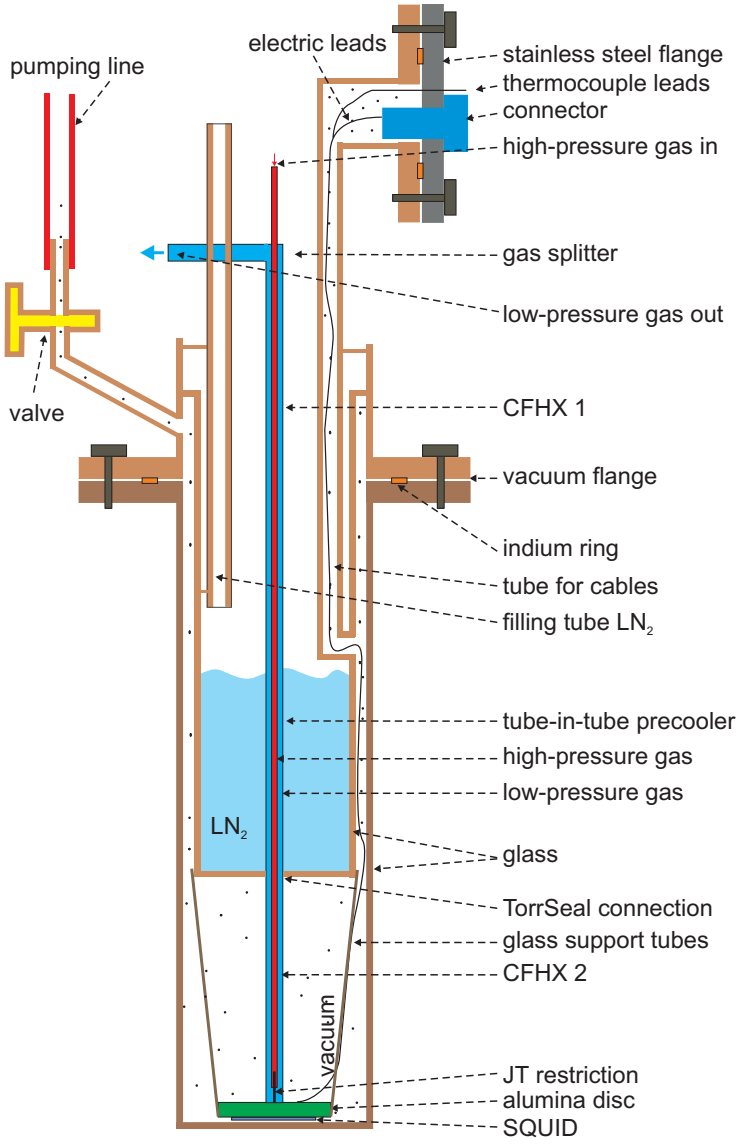

Figure 4.5: Schematic overview of the 30 K glass-tube cooler (not to scale). The glass 'insert' that is shown in the figure is placed in a cryostat made of G10 that is filled with liquid nitrogen.

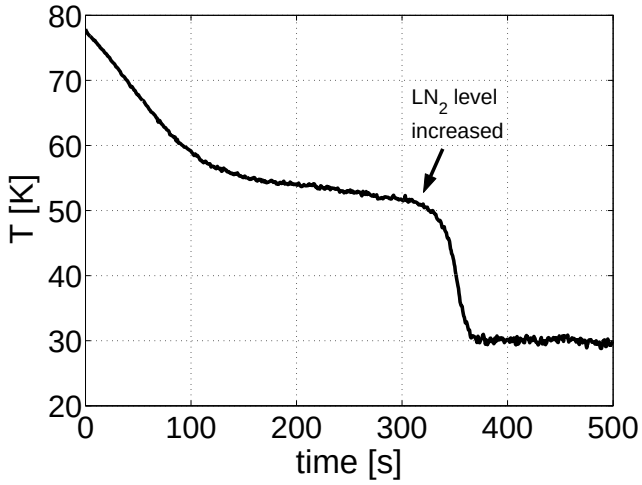

Figure 4.6: Cooldown curve for neon, precooled with liquid nitrogen and with a high pressure of 100 bar.

by means of a Bronkhorst pressure controller [18]. A splitter combines the high-pressure and the low-pressure gas lines into a tube-in-tube configuration which is first led through the LN_2 bath and then enters the vacuum space. The feedthrough of the outer glass tube through the bottom of the LN_2 reservoir is closed by means of TorrSeal [19]. The high-pressure gas is expanded over a small wire that is inserted into the inner tube [8]. The mass flow was measured in the low-pressure line with a Bronkhorst EL-FLOW type mass flow meter [18]. The cold tip was connected to an alumina disc with a diameter of 28 mm which can be used to mount the SQUID. The disc was supported with three glass tubes that are connected to the reservoir that holds the LN_2. The temperature of the cold tip was measured with an Omega E-type thermocouple [20], which was read-out with a Cryocon temperature controller [21] that applied 'cold junction compensation'. A resistor was also mounted to the cold tip to be able to heat-up the system and to determine the cooling power.

4.4 Cooler operation and characterisation

A cool down curve for a high pressure of 100 bar is shown in figure 4.6. It appeared that, upon filling the precooler with liquid nitrogen, the vacuum deteriorated. This resulted in a too large thermal load, causing the minimum temperature that could be achieved to be about 50 K as can be seen in the cool down curve around

300 seconds. When the precooler volume was completely filled with liquid nitrogen, the vacuum improved. The reduction in vacuum pressure appeared to be enough to reduce the parasitic heat load and reach a temperature of about 30 K. This effect is probably caused by a small leak in the glass structure that opens under thermal stress. Apparently, when the reservoir is only partly filled, this leak opens. When, on the other hand, the reservoir is completely filled it is closed either because the local thermal gradient is less and so are the associated thermal stresses, or because the liquid cannot pass the leak whereas nitrogen gas can. The presence of such a leak is quite likely. We found a number of small leaks at unexpected locations which were successfully repaired with a thin layer of TorrSeal.

The cooler reaches a temperature of about 30 K. The temperature sensor, an Omega E-type thermocouple [20], indicated temperatures down to 20 K which is physically not possible as the normal boiling point of neon is 27.2 K. Similar deviations were reported by Rijpma *et al.* [22] and the supplier advises not to use an E-type thermocouple for temperatures lower than -200 ℃ [20]. Application of a T- or N-type thermocouple may give better readings, despite their lower sensitivity [20]. Alternatively, other sensor types like e.g. calibrated diodes or Cernox resistance sensors are options. The measured temperatures were corrected by estimating the pressure drop over the low-pressure gas line. This pressure drop depends on the temperature profile because of the temperature dependencies of the density and the viscosity. Assuming that the warm CFHX has an adiabatic wall, a pressure drop of 2.0 bar was estimated. This would result in a cold-stage temperature of 31.3 K. When it is assumed that the wall of the warm CFHX is at 77.2 K over the whole length a pressure drop of 0.5 bar was calculated, resulting in a cold-stage temperature of 28.5 K. At liquid nitrogen temperature, the thermocouple gave a temperature reading that was 2.2 K too low. The measured temperatures were scaled based on this information and the result is shown in figure 4.6.

The available cooling power was determined by steadily increasing the heat supplied by a resistor that was also connected to the cold tip. Figure 4.7 shows the measured temperature, averaged over 10 seconds, as a function of the heating power. The net available cooling power is about 43 mW, the input power at which the temperature rapidly increases. The sudden increase of the temperature is at the point where the amount of liquid produced is too small to take up the total heat load. The temperature rise at lower input powers is probably due to the fact that the heater is positioned close to the thermocouple. Thus, the heater lifts the thermocouple temperature while the cooler remains at liquid neon temperature. The mass flow through the cold stage was about 6 mg/s. With this flow, and assuming that the high-pressure gas flows out of the precooler with a temperature of 78 K, the model

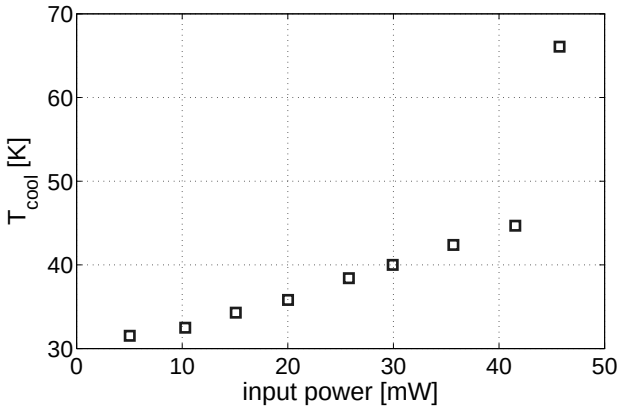

Figure 4.7: Determination of the cooling power.

gives an efficiency of 73% for the cold CFHX. This results in a gross cooling power of 51 mW. This agrees with the determined cooling power and the estimated heat load of about 5 mW for radiation and wires. The remainder will possibly be due to thermal conduction through the residual gas in the vacuum space. The copper lines for voltage read-out of the SQUID were not attached during the measurement. The realised temperature and cooling power are appropriate to cool a MgB_2-SQUID. In the near future, a MgB_2-SQUID will be mounted to the cold stage.

4.5 Conclusions

A glass cooler was realised for cooling a MgB_2-SQUID based on an open-loop Linde-Hampson cycle. The cooler consists of two counterflow heat exchangers and a precooler that were all realised in a tube-in-tube configuration. The high-pressure gas was precooled by leading the tube-in-tube configuration through a bath of liquid nitrogen. The high-pressure gas in the inner tube was cooled via low-pressure gas in the annular gap. A temperature of about 30 K was achieved with a measured net cooling power of 43 mW. This was in agreement with results from models for the counterflow heat exchangers and the tube-in-tube precooler. One or more small leaks to the vacuum are present in the current set-up that possibly result from thermal stresses. The cooling power and realised temperature are appropriate for the operation of a MgB_2-SQUID. In the near future, such a SQUID will be mounted onto the cold stage.

References

[1] A. Brinkman, D. Veldhuis, D. Mijatovic, G. Rijnders, D. H. A. Blank, H. Hilgenkamp, and H. Rogalla. Superconducting quantum interference device based on MgB_2 nanobridges. *Applied Physics Letters*, 79(15), 2001.

[2] Dragana Mijatovic. *MgB_2 thin films and Josephson devices*. PhD thesis, University of Twente, 2004.

[3] H. J. M. ter Brake, R. Karunanithi, H. J. Holland, J. Flokstra, D. Veldhuis, L. Vargas, J. W. M. Hilgenkamp, W. Jaszczuk, N. Janssen, F. J. G. Roesthuis, and H. Rogalla. A seven-channel high-T_c SQUID-based heart scanner. *Meas. Sci. Technol.*, 8:927–931, 1997.

[4] A. P. Rijpma, H. J. M. ter Brake, E. de Vries, N. Nijhof, H. J. Holland, and H. Rogalla. A high-T_c SQUID-based sensor head cooled by a Joule-Thomson cryocooler. *Physica C*, 372-376:209–212, 2002.

[5] J. Clarke and A. I. Braginski. *The SQUID Handbook*. Wiley-VCH Verlag, Weinheim, Germany, 2004.

[6] G. Walker. *Miniature refrigerators for cryogenic sensors and cold electronics*. Clarendon Press, 1989.

[7] A. P. Rijpma. *Fetal Heart Monitor, Development of a cryocooler-cooled high-T_c SQUID system for fetal magnetocardiography in unshielded environment*. PhD thesis, University of Twente, 2002.

[8] H. J. Holland, J. F. Burger, N. Boersma, H. J. M. ter Brake, and H. Rogalla. Miniature 10150 mW Linde-Hampson cooler with glass-tube heat exchanger operating with nitrogen. *Cryogenics*, 38(4):407–410, 1998.

[9] J. Burger, H. Holland and. E. Berenschot and. J. H. Seppenwoolde, M. ter Brake, H. Gardeniers, and M. Elwenspoek. 169 Kelvin cryogenic microcooler employing a condenser, evaporator, flow restriction and counterflow heat exchangers. In *Technical Digest. MEMS*, pages 418–421, 2001.

[10] Cryodata Inc., P.O. box 558, Niwot, CO 80544, USA, http://www.cryodata.com.

[11] J. F. Burger. *Cryogenic Microcooling, A micromachined cold stage operating with a sorption compressor in a vapor compression cycle*. PhD thesis, University of Twente, The Netherlands, 1987. downloadable from: http://purl.org/utwente/23470.

[12] J. Lester. Closed cycle hybrid cryocooler combining the Joule-Thomson cycle with thermoelectric coolers. In *Advances in Cryogenic Engineering*, volume 35, pages 1335–1340, 1990.

[13] H. Hausen and H. Linde. *Tieftemperaturtechnik: Erzeugung sehr tiefer Temperaturen, Gasverflüssigung und Zerlegung von Gasgemischen*. Springer-Verlag, Berlin, 2nd edition, 1985.

[14] A. Bejan. *Heat transfer*. Wiley, New York, 1993.

[15] R. K. Shah and A. L. London. *Laminar flow forced convection in ducts : a source book for compact heat exchanger analytical data*. Advances in heat transfer. Academic

Press, New York, 1978.

[16] P. P. P. M. Lerou, T. T. Veenstra, J. F. Burger, H. J. M ter Brake, and H. Rogalla. Optimization of counterflow heat exchanger geometry through minimization of entropy generation. *Submitted to Cryogenics*, January 2005.

[17] A. Roth. *Vacuum technology*. Elsevier Science, Amsterdam, 1990.

[18] Bronkhorst High-Tech B.V., Nijverheidsstraat 1A, 7261 AK, Ruurlo, The Netherlands, http://www.bronkhorst.nl.

[19] Varian, Inc., 3120 Hansen Way, Palo Alto, CA 94304-1030, USA, http://www.varianinc.com.

[20] Omega Engineering, Inc., One Omega Drive, Stamford, Connecticut 06907-0047, USA, http://www.omega.com.

[21] Cryogenic Control Systems, Inc., 17279 La Brisa St., Rancho Santa Fe, CA 92067-7012, USA, http://www.cryocon.com.

[22] A. P. Rijpma, D. J. Meenderink, H. A. Reincke, G. C. F. Venhorst, H. J. Holland, and H. J. M. ter Brake. A nitrogen triple-point thermal storage unit for cooling a SQUID magnetometer. *Cryogenics*, 45:231–239, 2005.

Chapter 5

Sorption compressor efficiency and complexity

5.1 Single-cell compressor design

This chapter addresses the efficiency and the complexity of sorption compressors that are used in combination with a LH cold stage. In this section, an alternative compressor lay-out is presented that is considerably less complex than the conventional design. In section 5.2, a method is described to accurately determine the cooler efficiency based on a separate analysis of the compressor and the cold stage. This method is extended to handle multi-stage compression that can increase the cooler efficiency. The method used assumes a quasi-static behaviour of the compressor cell and a uniform temperature in the sorber material.

A JT expansion stage requires a more or less continuous mass flow in order to obtain a continuous cooling power. Besides, the compressor should supply a constant low pressure as this pressure is directly related to the low-end temperature of the cold stage. As set out in section 1.2, a single sorption cell supplies an inherently non-continuous flow. An alternative to using multiple compressor cells to get a continuous flow is a compressor unit that uses only a single sorption compressor cell and two buffer volumes separated by passive valves. This design is shown in figure 5.1. A similar design was applied by Duband and Suhanan [1, 2], but they did not analyse the concept in detail.

During phase A of the sorption cycle, the sorber container is heated and pressure builds up in the sorber container as both check valves are closed because of the pressure differences over the valves. The high-pressure buffer supplies gas to the

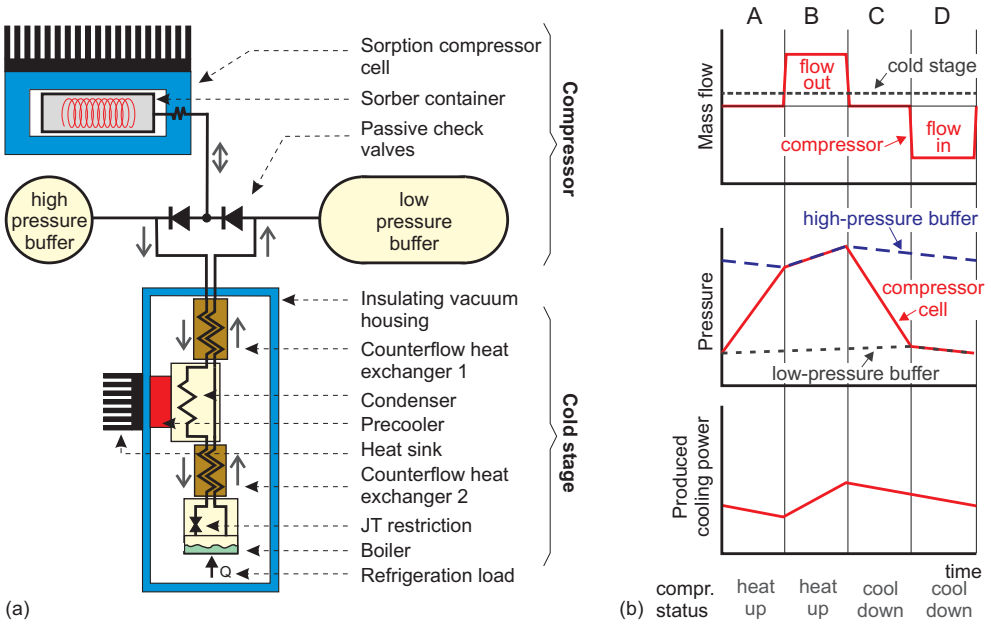

Figure 5.1: Single-cell sorption compressor combined with a LH cold stage. (a) Schematic drawing of the configuration. (b) Mass flow, pressure and produced cooling power with time.

cold stage which is taken up by the low-pressure buffer, while no gas flows to or from the compressor cell. As a consequence, the pressure of the high-pressure buffer slowly decreases while that of the low-pressure buffer steadily increases. Once the pressure in the container has become higher than that of the high-pressure buffer, the high-pressure check valve opens and a relatively large gas flow is supplied to the high-pressure buffer, causing the pressure of that buffer to rise (phase B). At the same time, some gas flows through the cold stage, increasing the pressure in the low-pressure buffer. When the container is cooled down, the pressure in the container decreases and the high-pressure check valve closes (phase C). Again, the flow through the cold stage is maintained by the buffers. When the pressure in the container has dropped below that of the low-pressure buffer, the low-pressure check valve opens and gas flows from the buffer to the cell (phase D). The pressure in the high-pressure buffer decreases because of the flow through the cold stage.

This configuration has important advantages compared to the traditional lay-out. First of all, the number of components is reduced. This increases the reliability of the compressor. Besides, controlling the cooler has become easier as only one sorption compressor cell needs to be driven. The reliability of the design can be

further increased by mounting a second compressor cell between the low-pressure and high-pressure buffers. The two parallel cells can be operated independently. If one of the compressor cells fails, the compressor can still operate (redundancy). The advantage of reduction of complexity becomes even more pronounced when multi-staged compression is applied as suggested by Bard [3]. With a two-stage compression approach, the COP of the cooler can be increased. Then, instead of two compressor units consisting of at least six sorption compressor cells and 12 check valves, only two sorption compressor cells, three buffer volumes and four check valves are needed. Besides, in the proposed lay-out no synchronisation between the different compressor cells is needed. As a result, each cell can be cycled at its optimum cycle frequency, and does not have to be tuned to others as is the case in the traditional lay-out. The cycle time will also be shorter. Therefore, the single-cell design provides a larger mass flow per cell than in the traditional design, assuming that the cell pumps the same amount of gas from the low-pressure to the high-pressure side during a cycle. A disadvantage of the proposed design compared to the traditional lay-out is the slight variation in pressure of the low-pressure buffer. This will result in some variation of the cold-stage temperature. Proper design of the low-pressure buffer can minimise this temperature variation as is discussed in section 6.1.6. Furthermore, this temperature variation can be damped passively or actively. Another disadvantage of the pressure variations in the buffers is that both the flow through the cold stage and the enthalpy of cooling will slightly vary with time as shown in figure 5.1. However, the actual cooling power of the cold stage is buffered by the evaporating liquid in the boiler. In the traditional lay-out, it is possible to recover the heat from one cell to heat up another which is not possible in the single-cell design. However, heat recovery makes the design of the traditional lay-out even more complex.

A test set-up was realised to investigate the behaviour of the proposed single-cell compressor concept. This set-up is discussed in chapter 6. In the remainder of this chapter, the efficiency of the compressor is addressed. The two-stage single-cell compressor is demonstrated in chapter 7.

5.2 Thermodynamic optimisation

The COP of a cooler results from equation (3.1). The efficiency of the compressor and that of the cold stage can also be calculated separately with the help of the exergy [4, 5]. The exergy is the maximum amount of work that can be produced theoretically from a given temperature and pressure difference. The compressor

efficiency can then be defined as

$$COP_{compr} = \frac{E}{P_{input}} \tag{5.1}$$

with E the exergy produced by the compressor and P_{input} the (electrical) input energy to the compressor. Section 5.2.1 describes the method used to determine the compressor efficiency. The analysis of the cold stage is presented in section 5.2.2.

5.2.1 Compressor analysis

Single-stage sorption compressor

In this section, the equations are presented to determine the efficiency of a single stage compressor. The method followed was based on work of Burger *et al.* [4, 6]. The compressor efficiency can be derived independent of its size and therefore the analysis is performed normalised to the sorber mass. The COP of the compressor from equation (5.1) can be rewritten as

$$COP_{compr} = \frac{m_{gas}e}{P_{input}} = \frac{\Delta x_{net}e}{p_{input}} \tag{5.2}$$

with m_{gas} the amount of gas that is delivered by the compressor during a cycle, P_{input} the total energy input to the compressor in a cycle, Δx_{net} the net amount of gas per unit of sorber material that flows out of the compressor, p_{input} the energy input during a cycle normalised per unit of sorber material and e the specific exergy of the gas. To calculate the COP of a sorption compressor cell, both the heat input and the exergy need to be determined. The exergy output depends on the amount of gas that is supplied during a single cycle and its exergy [4, 5]

$$e = \Delta h - T_L \Delta s = [h(T_L, p_H) - h(T_L, p_L)] - T_L[s(T_L, p_H) - s(T_L, p_L)] \tag{5.3}$$

with h the specific enthalpy and s the specific entropy of the gas. The subscript H refers to the conditions at the high-pressure side and an L refers to the conditions on the low-pressure side. It is assumed that the heat sink is at T_L and that the high-pressure gas is precooled to the heat sink temperature before it comes available to the cold stage. The normalised amount of gas Δx_{net} that flows out of the compressor during a cycle is the difference between the total amount of gas between points 2 and 3 in figure 5.2.

$$\Delta x_{net} = x_{tot2} - x_{tot3} = x_{tot1} - x_{tot3} = \Delta x_s + \Delta x^*_{void} \tag{5.4}$$

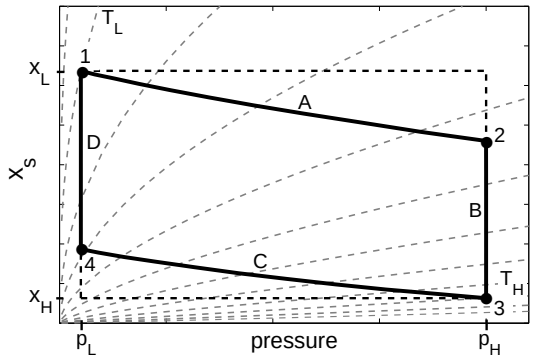

Figure 5.2: Sorption cycle. Adsorbed amount of gas x_s versus pressure. The dashed lines are isotherms ranging from the compressor low temperature T_L to a compressor high temperature T_H. A more detailed description is given in section 1.2.

with x_{tot} the sum of the adsorbed gas x_s and the free gas in the available void volume x^*_{void} normalised to the amount of sorber material, and Δx_s the difference in the adsorbed gas fraction between the points 1 and 3. Along path A, the total amount of gas in the compressor cell does not change, which explains the second equality in equation (5.4).

The difference in mass fraction of the free gas in the available void volume Δx^*_{void} is

$$\Delta x^*_{void} = x^*_{void1} - x^*_{void3} \tag{5.5}$$

The volume inside the container of a sorption cell V_{total} is filled with sorber material V_s and the remainder is the void volume V_{void}. Not all of the void volume is available to the free gas as part of it is taken up by the adsorbed gas. The part of the void volume that is available to the free gas V^*_{void} therefore equals

$$V^*_{void} = V_{void} - V_{ads}(T, p) \tag{5.6}$$

with V_{ads} the volume of the adsorbed gas. A uniform temperature is assumed in the compressor cell thoughout the sorption cycle. If the void volume fraction α is defined as

$$\alpha \equiv V_{void}/V_{total} \tag{5.7}$$

the amount of free gas normalised to the amount of sorber material x^*_{void} results as

$$x^*_{void}(T, p) = \rho_{gas}(T, p) \left(\frac{\alpha}{\rho_s(1-\alpha)} - \frac{x_s(T, p)}{\rho_{ads}} \right) \tag{5.8}$$

with ρ_s the density of the sorber material, ρ_{gas} the density of the free gas and ρ_{ads} the density of the adsorbed gas. Application of the ideal gas law yields

$$\Delta x^*_{void} = \frac{M}{R\rho_s}\frac{\alpha}{1-\alpha}\left(\frac{p_1}{T_1} - \frac{p_3}{T_3}\right) - \frac{M}{R\rho_{ads}}\left(\frac{p_1 x_{s1}}{T_1} - \frac{p_3 x_{s3}}{T_3}\right) \tag{5.9}$$

Expressions for $x_s(T,p)$ are derived at a later point in this section.

The changes in temperature and pressure throughout the sorption cycle can now be determined from the temperatures and pressures at the points 1 and 3. During paths A and C, the total amount of gas is constant whereas in phases B and D, the pressure is constant. The total heat input can be derived when the heat associated with infinitesimal changes in pressure and temperature is known and quasistatic behaviour is assumed. The total heat input $q_{heat,tot}$ consists of the heat needed to heat up both the free gas in the void volume $q_{free\ gas}$ and the adsorbed gas $q_{ads\ gas}$, that to heat up the thermal mass of the cell q_{TM}, and the heat of sorption $q_{sorption}$.

$$dq_{heat,tot} = dq_{free\ gas} + dq_{ads\ gas} + dq_{TM} + dq_{sorption} \tag{5.10}$$

The differential heat input for the adsorbed gas $dq_{ads\ gas}$ is

$$dq_{ads\ gas}(T,p) = x_s(T,p)c_{p,ads\ gas}(T,p)dT \tag{5.11}$$

with $c_{p,ads\ gas}$ the heat capacity of the adsorbed gas at constant pressure. As the total amount of gas in the available void volume does not remain constant upon changes in temperature and pressure, the heat input to the free gas is derived from the first law of thermodynamics for open systems [5]

$$dU = dQ + dW + hdm \tag{5.12}$$

Here, dU is the change in internal energy, dQ is the heat added to the free gas, dW the work performed on the free gas which is negligible, h the specific enthalpy of the added gas and dm the amount of mass that is added to the available void volume. This mass can be derived from the changes in temperature and pressure with the help of the ideal gas law. When also the equipartition theorem is applied, the differential heat per unit of sorber material results as

$$dq_{free\ gas}(T,p) = x^*_{void}(T,p)c_{p,gas}(T,p)dT - \left(\frac{\alpha}{\rho_s(1-\alpha)} - \frac{x_s(T,p)}{\rho_{ads}}\right)dp \tag{5.13}$$

with $c_{p,gas}$ the specific heat of free gas at constant pressure.

The thermal mass consists of sorber material, container, and heater. The heat capacity of the latter is neglected. The container wall should be sufficiently thick to withstand the gas pressure inside the container. According to Berndt [7]

$$t_w = \frac{p_{max} D}{2\sigma_{max}} \tag{5.14}$$

with t_w the thickness of the container wall, p_{max} the highest pressure in the cell, D the inner diameter of the container wall, and σ_{max} the maximum allowed tensile stress in the container wall material. When the mass of the top and the bottom of the container are neglected, the heat capacity of the container can be determined per unit of sorber material.

$$\mu_m \equiv \frac{m_w}{m_s} = \frac{2\rho_w}{\rho_s(1-\alpha)} \frac{p_{max}}{\sigma_{max}} \tag{5.15}$$

with m_w the mass and ρ_w the density of the wall material. The differential heat per gram of sorber material results as

$$dq_{TM}(T,p) = [c_{ps}(T) + c_{pw}(T)\mu_m]\, dT \tag{5.16}$$

with c_{ps} the specific heat of the sorber material and c_{pw} that of the wall material at constant pressure.

The heat of sorption can be derived from the isotherms as [8]

$$q_{ads} = -R \left. \frac{\partial \ln(p/p_o)}{\partial(1/T)} \right|_{x_s} \tag{5.17}$$

with p_o the standard pressure. The differential heat on a change in temperature and pressure then is

$$dq_{sorption}(T,p) = -q_{ads}\left(x_s(T,p)\right)\left[x_s(T+dT, p+dp) - x_s(T,p)\right] \tag{5.18}$$

The same terms also apply for the amount of cooling, or in other words the heat load to the heat sink, but two terms have to be added. The high-pressure gas that flows out off the compressor in phase B is cooled to heat sink temperature. Besides, gas that returns from the cold stage is colder than the cell. Upon entry in the sorber container the cold gas warms up while the sorber material cools down. The flow of cold gas reduces the amount of heat that is dumped to the heat sink. Both contributions can be determined from

$$dq_{flow}(T,p) = [x_{tot}(T+dT, p+dp) - x_{tot}(T,p)] \int_{T_L}^{T} c_{p,gas}(T',p) dT' \tag{5.19}$$

and should be added to calculate the amount of heat that is dumped to the heat sink

$$dq_{cool,tot} = dq_{free\ gas} + dq_{ads\ gas} + dq_{TM} + dq_{sorption} + dq_{flow} \tag{5.20}$$

The total heat input and the compressor efficiency can now be determined by integration over the sorption cycle.

Multi-stage sorption compressor

It appears from figure 5.2 that a considerable amount of the gas that is adsorbed in point 1 is lost in the void volume and cannot be used for expansion in the cold stage. The void volume inside a compressor cell consists of the pores inside the sorber, the interparticle volume and the external void volume caused by the line between the sorber container and the check valves. The pore size distribution in most activated carbons falls into three groups: macropores are larger than 50 nm, mesopores are between 2 and 50 nm and micropores are smaller than 2 nm in diameter [13]. The meso and macropores are mostly filled with compressed gas and the amount of adsorbed gas is small. Selection of a sorber material with a small macro and interparticle volume and a large micropore volume is attractive to reduce the amount of gas that is lost in the void volume upon compression. Typical values of void volume fractions for various charcoals are given in table 5.1. An extensive overview of sorber materials and its main characteristics can be found in the overview of Menon *et al.* [13]. Barneby-Cheney GI, Maxsorb and Saran all have relatively large micropore volumes compared to typical activated carbons when the small mesopores of Maxsorb are added to its micropore volume. Saran can be

Carbon	Typical act. carbon [3, 9]	Compressed Barneby-Cheney GI [3, 12]	Maxsorb [9, 10]	Saran [4, 11]
volume fractions [%]				
- micropores ($<$ 2nm)	17.6	38.4	12.0	35.2
- mesopores (2-50 nm)	4.4	29.0	44.4*	15.5
- interparticle volume and macropores ($>$ 50nm)	58.0		30.0	7.0
- sorber	20.0	32.6	13.6	42.3
shape	powder	powder	powder	monolith

* Mesopores of 2-4 nm especially contribute to this volume.

Table 5.1: Volume fractions in percent of voids, micropores and sorber material for various activated carbons. Table adapted from [3, 4].

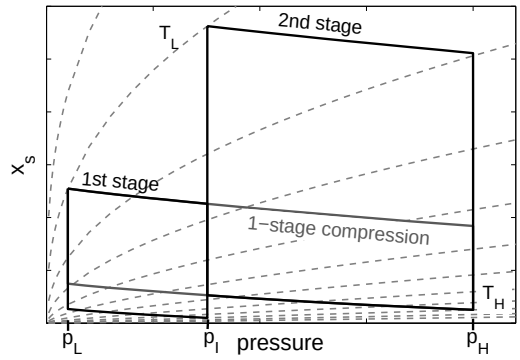

Figure 5.3: Two-stage sorption cycle. The first stage compresses the gas from the low-pressure p_L to the intermediate pressure p_I. The second stage compressor lifts the gas from p_I to the high pressure p_H. The grey line shows the cycle in case of single stage compression between the same temperatures and pressures.

produced as a monolith. This reduces the interparticle volume resulting in a lower void volume fraction. Besides, Saran can be made in arbitrary shapes which enables reduction of the external void volume. To our knowledge, of these three sorbers, only Maxsorb is currently commercially available.

Another measure to reduce the effect of the void volume that can be applied, is the use of multi-stage compression as was suggested by Bard [3]. The sorption cycle of a two-stage compressor is shown schematically in figure 5.3. The grey line shows the sorption cycle when single-stage compression is applied to reach the high pressure p_H from the low pressure p_L. When two-stage compression is applied, each compressor has a smaller pressure swing and therefore less gas is lost in the void volume, see equation (5.9). Besides, the second stage compressor starts at a higher pressure. At a higher pressure and the same heat sink temperature, the adsorbed amount of gas is considerably higher resulting from the shape of the isotherms. Therefore, more gas can be desorbed and a larger COP can be obtained. The drawback of the two-stage design is the increase in complexity.

A practical realisation of a two-stage compressor using the conventional compressor design from figure 1.3 is shown in figure 5.4a. In total 8 compressor cells and 16 check valves are needed. The gas that is supplied by a cell in the first stage compressor is taken up by a cell in the second stage. This implies that for the conventional design and for a given set of pressures p_L, p_I, and p_H with p_I the

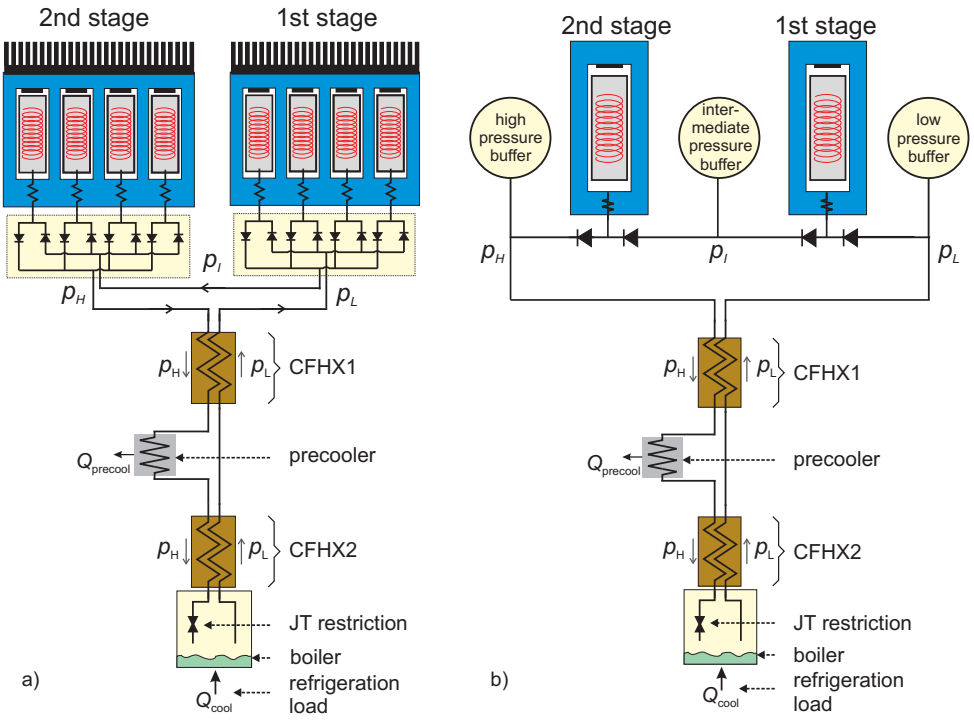

Figure 5.4: Lay-out of a two-stage sorption compressor (a) based on the conventional compressor design as shown in figure 1.3 (b) based on the single-cell design as presented in section 5.1. The operation of the cold stage is discussed in section 5.2.2.

intermediate pressure

$$m_{s1}\Delta x_{net1}(T_L, T_{H1}, p_L, p_I) = m_{s2}\Delta x_{net2}(T_L, T_{H2}, p_I, p_H) \tag{5.21}$$

Here, it is assumed that both stages have the same heat sink temperature T_L. This implies that apart from the timing, also the masses of the cells have to be matched.

It is advantageous to apply the single-cell concept as introduced in section 5.1 when two-stage compression is applied. The reduction in complexity for the single-cell design then becomes even more pronounced. The lay-out for the two-stage single-cell compressor design is shown in figure 5.4b. Now, only two compressor cells, 4 check valves and 3 buffer volumes are needed, which is a considerable reduction compared to the conventional lay-out. Burger [4] proposed to reduce the complexity of a two-stage compressor based on the conventional compressor design by combining the first and second compression stages in a single compressor cell. This is less complex than a two-stage based on the conventional design but has the

disadvantage of complexer compressor cells. Besides, the temperature T_H must be the same for both compression stages and cannot be optimised separately.

Also in two-stage operation, each compressor can be operated independent of the other as synchronisation is not needed. In principle, the intermediate pressure buffer can be left out but then synchronisation is required again. To achieve a given set of pressures p_L, p_I, and p_H the average flow that is delivered by both compression stages should be equal

$$\dot{m}_{compr1} = \dot{m}_{compr2} = \dot{m}_{cool} \tag{5.22}$$

Rewriting in terms of compressor mass, change in net amount of gas in the compressor, and cycle times gives

$$\frac{t_{cycle2}}{t_{cycle1}} \frac{m_{s1}}{m_{s2}} = \frac{\Delta x_{net2}(T_L, T_{H2}, p_I, p_H)}{\Delta x_{net1}(T_L, T_{H1}, p_L, p_I)} \tag{5.23}$$

So, for the single-cell design with given pressures, the ratio of cycle times and sorber masses should be chosen such that they match the Δx_{net}-ratio. The term on the right-hand side is fixed for given temperatures and pressures and for a given sorber-gas combination whereas the values on the left-hand side can still be chosen. The efficiency of a two-stage compressor as a whole is

$$COP_{2\ st} = \frac{m_{gas} e_{compr}(T_L, p_L, p_H)}{Q_{tot1} + Q_{tot2}} = \frac{e_{compr}(T_L, p_L, p_H)}{\frac{q_{tot1}}{\Delta x_{net1}} + \frac{q_{tot2}}{\Delta x_{net2}}} \tag{5.24}$$

Note that the efficiency is independent of the size of the individual compressor cells. It can be shown that the same result is obtained for a synchronised two-stage compressor based on the conventional design.

Adsorption isotherms

In order to determine the efficiency of a sorption compressor it is required to know the gas fractions x_s as a function of temperature and pressure. This can be obtained by fitting measured sorption isotherms. Several methods to fit measured sorption data have been developed. According to Yang [14], the potential theory, which was first described by Polanyi, gives the best results for adsorption on activated carbon. This theory assumes the existence of a characteristic curve that describes the amount of adsorbed gas as a function of the adsorption potential ϵ. The shape of this curve was determined empirically by Dubinin [14, 15] as

$$x_s(T, p) = \frac{M}{b} W_o e^{-\kappa(\frac{\epsilon}{\beta})^n} \tag{5.25}$$

Gas	Sorber	n	p_s	W_o [cm^3/g]	κ [(mol/J)^n]	error [mg/g]
N_2	Maxsorb	1.15	Dubinin	0.642	$6.33{\cdot}10^{-5}$	2.4
N_2	Saran	1.85	Maslan	0.292	$3.82{\cdot}10^{-8}$	1.2
Xe	Maxsorb	1.5	Dubinin	$1.03^{(*)}$	$1.54{\cdot}10^{-6(*)}$	22
Xe	Saran	2.85	Dubinin	0.347	$1.56{\cdot}10^{-12}$	9.4

* Values are for 300 K. See text for details.

Table 5.2: Fitting results of nitrogen and xenon gas on Maxsorb and Saran based on measured sorption data [18]. The error in the last column is the resulting average absolute error between fit and measured data.

with b the Van der Waals volume, W_o the limit volume of adsorption space, which results from fitting the characteristic curve to experimental data, and κ a fitting parameter. The value of n empirically ranges from below 1 to about 14 [16]. The affinity coefficient β was intended as shifting factor to bring the characteristic curve of all gases on the same sorbent into a single curve. This worked fine for the gas-sorber combinations investigated by Dubinin [15], but turned out to be less accurate for some others [14]. Polanyi and Dubinin assumed for the adsorption potential [14, 15]

$$\epsilon = RT \ln \frac{p_s}{p} \tag{5.26}$$

with p_s the saturated vapour pressure. A variety of modifications has been proposed to this equation, all useful for specific gas-sorber combinations in a specific regime of temperatures and pressures [14]. In a sorption compressor, adsorption is typically applied above the critical temperature of the gas and the saturated vapour pressure is undefined. Also here, a variety of relations for p_s has been suggested [14]. In this thesis, the choice was limited to the extensions originally proposed by Dubinin [15]

$$p_s = p_{cr} \left(\frac{T}{T_{cr}} \right)^2 \tag{5.27}$$

and the extrapolation of the saturated vapour pressure above the critical temperature as suggested by Maslan [14, 17]

$$\ln \left(\frac{p_s}{p_o} \right) = A + \frac{B}{T} \tag{5.28}$$

with A and B constants to fit the saturated vapour pressure with temperature.

The single-stage concept from section 5.1 was realised with Maxsorb activated carbon as the sorber material and xenon as the working gas, see chapter 6. A two-stage compressor was realised with nitrogen as the working gas and the same sorber

material, see chapter 7. To investigate the influence of the void volume fraction, the calculations of the compressor COP were performed both with Maxsorb and with Saran.

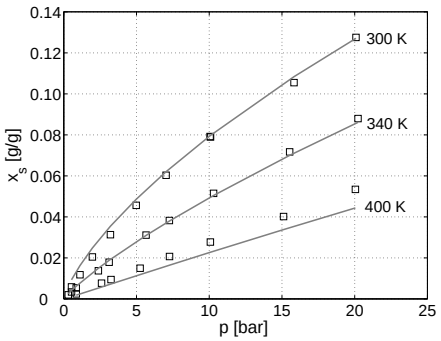

Figure 5.5: Measured sorption isotherms [18] and resulting fit for three isotherms for nitrogen gas adsorbed on Maxsorb.

Measured sorption isotherms for these gas-sorber combinations [18] were fitted using equations (5.25) to (5.28). The characteristic curve was determined for multiple values of the parameter n in equation (5.25). The fit result was compared with the originally measured data and the value of n that gave the smallest mean absolute error was selected. This procedure was followed for both the Maslan and Dubinin extensions of the saturated vapour pressure. The best of these two was selected. The affinity coefficient β was set to 1 and not changed for other gases. Only isotherms from room temperature and above were included in the fitting procedure. The fitting parameters W_o and κ were derived from the fit and the results are summarised in table 5.2. It turned out that for the current gas-sorber combinations and the current temperature and pressure regime, this fitting method did not work very well. Fair fits were obtained for all gas/sorber combinations apart from xenon on Maxsorb. For this combination, all available

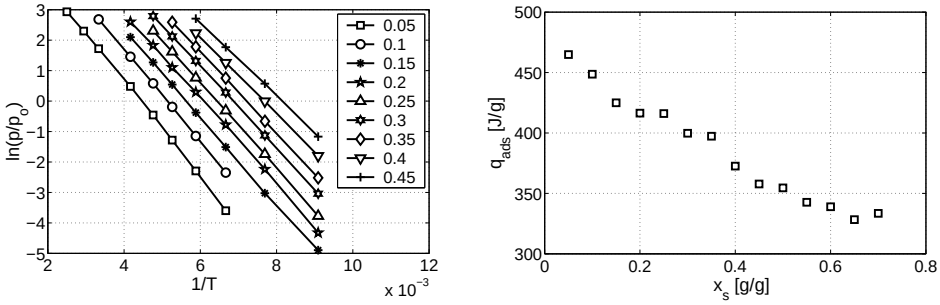

Figure 5.6: Derivation of the heat of adsorption based on equation (5.17). (Left) plots of $\ln(p/p_o)$ versus $1/T$ for various adsorbed gas fractions x_s. (Right) Resulting sorption heat as a function of adsorbed fraction x_s.

isotherms were fitted separately. The parameter n had the smallest variation. The individual isotherms were again fitted, but now with a fixed value of n = 1.5, the average over the isotherms. The fitting parameters W_o and κ were determined as a function of temperature in the range between 300 K and 600 K and resulted as $W_o = 5.67 \cdot 10^{-6}T^2 - 7.70 \cdot 10^{-3}T + 2.83$ and $\kappa = -2.41 \cdot 10^{-9}T + 2.26 \cdot 10^{-6}$. The values in the table are for 300 K. As an illustration, the measured data and resulting fits for Maxsorb/N_2 are shown in figure 5.5. Figure 5.6 shows the determination of the heat of adsorption from the measured isotherms based on equation (5.17) as a function of the adsorbed gas fraction x_s.

Optimised compressor efficiency

When a single-stage compressor is operated with fixed values of the compressor low temperature T_L, high temperature T_H and low pressure p_L, the exergy increases when the compressor high pressure is increased whereas the net amount of gas Δx_{net} decreases as results from equations (5.4) and (5.9). The total input power rises when the high pressure is increased as a thicker compressor wall is required. The combined effect is that an optimum in the compressor COP is observed as a function of the high pressure. The compressor high temperature can also be optimised for each value of the high pressure. The effect of a decrease in Δx_{net} caused by an increase in the high pressure can be partly compensated by heating the compressor to a higher temperature, resulting in more desorption. Optimised compressor efficiencies for both single-stage and two-stage compressions with Maxsorb and Saran are shown in figure 5.7. For two-stage compression, the high temperatures of the two stages and the intermediate pressure were optimised. For all graphs, the low pressure was set to 1 bar and a heat sink temperature of 293 K was taken. Stainless steel 316 was chosen as the container material. The temperature dependent heat capacity and density of stainless steel and the sorber were taken from MPBD [19]. The maximum allowable stress σ_{max} was set at half the yield strength of stainless steel. At 600 K, this yield strength equals 220 MPa [19]. The sorption heat was included as a function of the adsorbed fraction x_s by means of a linear fit of the heat of adsorption as derived in figure 5.6. Temperature and pressure dependent gas properties were taken from Gaspak [20]. For the heat capacity of the adsorbed gas that of the liquid at the critical point was taken.

The efficiency of a two-stage compressor is, as was expected, higher than that of a single-stage compressor with the same pressure swing. Besides, considerably higher pressures can be reached with only a small reduction in efficiency. A two-stage compressor with Saran can e.g. reach 45 bar with the same efficiency as a

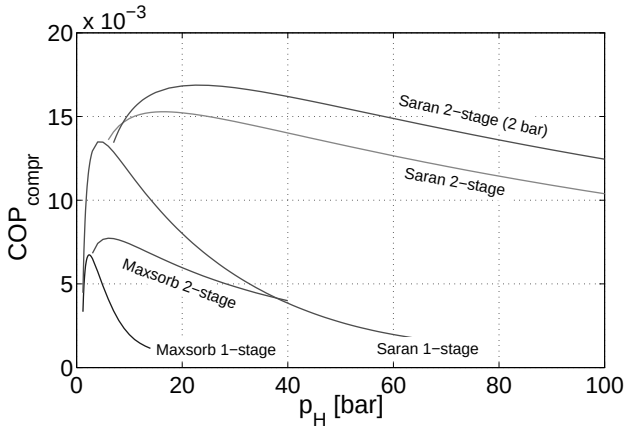

Figure 5.7: Optimised compressor efficiency for both a single-stage and a 2-stage compressor filled with Maxsorb or Saran and with nitrogen as the working fluid.

single-stage compressor with a high pressure of only about 5 bar. It is obvious that higher compressor efficiencies can be achieved when more gas is adsorbed at the selected low pressure and heat sink temperature. This is illustrated by the plot of a two-stage compressor with Saran starting from 2 bar. The majority of heat input to the compressor is used to heat up the sorber material, taking up some 85% of the input power to the first stage and some 60% of the second stage. The input to the heat capacity of the wall is about 12% for the first stage and 32% for the second stage.

Further improvement of the compressor efficiency can be achieved by reduction of the heat input to the heat capacities of the sorber and the wall. The first can be realised by a sorber material with a large adsorption capacity per mass of sorber material. Upon pressure build up in the compressor, the sorber material is heated to desorb adsorbed gas. The larger the adsorption capacity, the lower the required input to the thermal mass of the sorber per gram of gas that flows out off the compressor. The heat input to the wall can be reduced by selecting a material with a high strength and a low heat capacity [4, 21]. This is especially attractive when gas is compressed to high pressures as the contribution of the heat input to the wall becomes significant. Some candidates are aluminum, Inconel and some titanium alloys. For small compressor diameters, the wall thicknesses become extremely thin, which complicates the manufacturing.

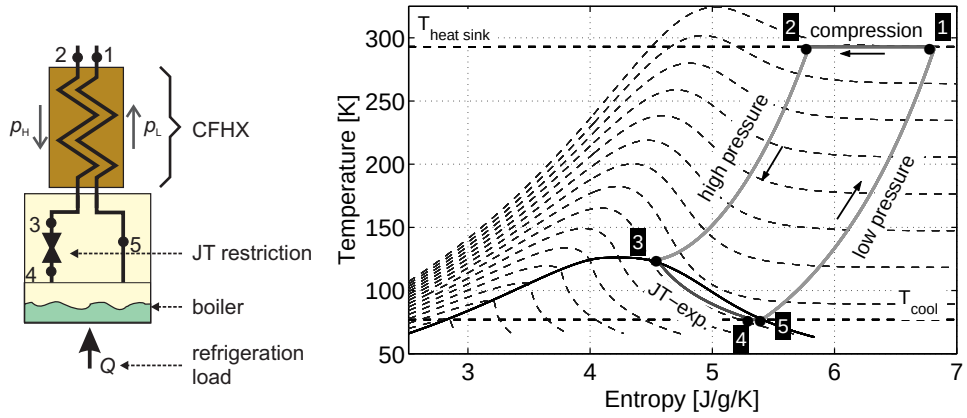

Figure 5.8: (a) Cold stage with a Joule-Thomson expansion valve. (b) Related Ts-diagram for nitrogen gas with a low pressure of 1 bar and a high pressure of 30 bar.

5.2.2 Cold stage analysis

Basic Joule-Thomson expansion

The basic form of the Linde-Hampson cold stage is drawn schematically in figure 5.8 together with the corresponding temperature-entropy (Ts)-diagram for nitrogen gas with a low pressure of 1 bar and a high pressure of 30 bar. From point 1 to 2, low pressure gas is compressed isothermally. The high-pressure gas cools down in the counterflow heat exchanger (CFHX) until point 3 is reached. Then, the high-pressure gas enters the Joule-Thomson restriction and is expanded isenthalpically. When appropriate pressures and temperatures are selected, a part of the gas liquefies (point 4). The cooling load to the boiler causes the liquid to evaporate to point 5. In this specific example, the amount of nitrogen gas that is liquefied is relatively small. The low-pressure evaporated nitrogen flows into the CFHX precooling the warmer high-pressure gas. More information on this cycle can e.g. be found in [22]. As the specific enthalpy h is a state function

$$\Delta h_{12} + \Delta h_{23} + \Delta h_{34} + \Delta h_{45} + \Delta h_{51} = 0 \tag{5.29}$$

with the numbers as in figure 5.8. In an ideal CFHX, all enthalpy extracted from the high-pressure gas is taken up by the low-pressure gas, so, $\Delta h_{23} = -\Delta h_{51}$. As the Joule-Thomson expansion is isenthalpic, $\Delta h_{34} = 0$, and for the enthalpy of cooling results

$$\Delta h_{cool} = \Delta h_{45} = -\Delta h_{12} \tag{5.30}$$

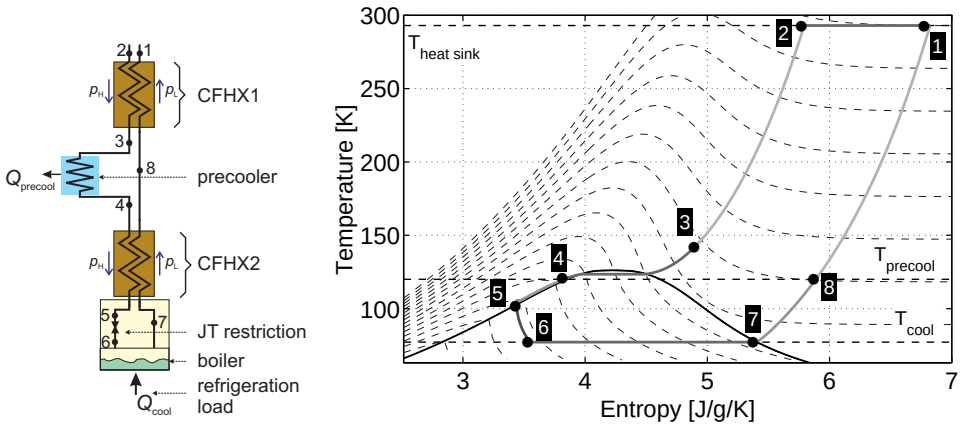

Figure 5.9: JT expansion stage with a precooler. (left) Schematic drawing of the cold stage (right) Ts-diagram for nitrogen with p_L is 1 bar, p_H is 30 bar, and a precool temperature of 120 K.

The efficiency of the cold stage equals

$$COP_{cold\ stage} = \frac{Q_{cool}}{E_{cool}(T_L, p_L, p_H)} = \frac{\Delta h_{cool}}{e_{compr}(T_L, p_L, p_H)} \equiv COP_{LH} \qquad (5.31)$$

Precooling

The efficiency of the cold stage can be increased by precooling the high-pressure gas [23]. Such a cold stage is shown schematically in figure 5.9. A precooler extracts heat from the high-pressure gas. The extracted enthalpy directly adds to the available cooling power. Assuming again ideal CFHXs, it can be derived that

$$\Delta h_{cool} = -\Delta h_{prec} - \Delta h_{compr} \qquad (5.32)$$

with $\Delta h_{cool} = \Delta h_{67}$, $\Delta h_{prec} = \Delta h_{34}$, and $\Delta h_{compr} = \Delta h_{12}$. The efficiency of the cold stage results as [4]

$$COP_{cold\ stage} = \frac{1}{\frac{e}{\Delta h_{cool}} + \frac{1}{COP_{prec}} \frac{|\Delta h_{prec}|}{\Delta h_{cool}}} \approx \frac{1}{\frac{1}{COP_{LH}} + \frac{1}{COP_{prec}}} \qquad (5.33)$$

with COP_{prec} the efficiency of the precooler. Figure 5.10 shows the effect of variation of the compressor high pressure and the precool temperature on the cold stage efficiency. To make the plot independent of the efficiency of the precooler,

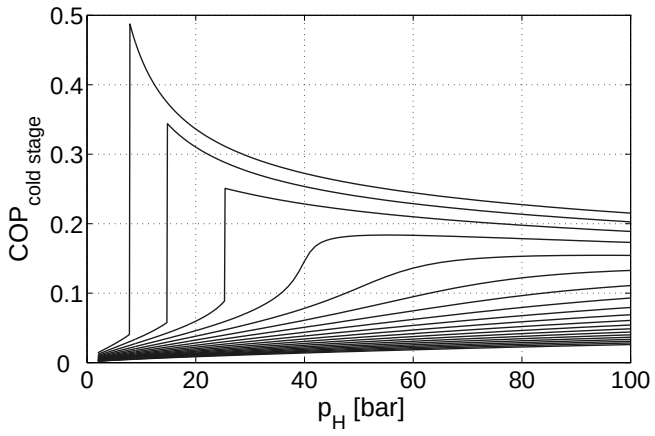

Figure 5.10: Influence of high pressure and precool temperature on the COP of a cold stage with nitrogen as the working gas, operating from 293 K and with a low pressure of 1 bar. The input power to the precooler was excluded in the calculation of the COP. The precool temperature increases from 100 K (top curve) to 290 K (bottom curve) in steps of 10 K

the input power to the precooler was excluded*. At higher pressures the cold stage efficiency increases because of the enthalpy increase upon compression at room temperature. More improvement, however, can be achieved with precooling. Precooling below the critical temperature is especially attractive as the relatively large enthalpy difference of the gas-liquid transition is added to the enthalpy of cooling. Precooling can e.g. be performed with a thermo-electric (TE) cooler.

Internal Joule-Thomson precooler

As mentioned above, it is attractive to precool the high-pressure gas in a JT cold stage to below the temperature at which the gas-liquid phase transition occurs at that pressure. For this purpose, however, a TE cooler can hardly be applied because its efficiency rapidly decreases at temperature differences larger than about 80 K [4, 24]. Such a temperature difference is not sufficient to liquefy e.g. high-pressure nitrogen, argon or krypton from room temperature. As an alternative, when two-stage compression is applied, the pressure difference over the second compression stage can be used for precooling purposes via an additional JT loop as depicted in figure 5.11. A TE cooler is included to precool the JT precooler.

*For all other calculations in this chapter, the efficiency of the precooler *is* included in the efficiency of the cold stage.

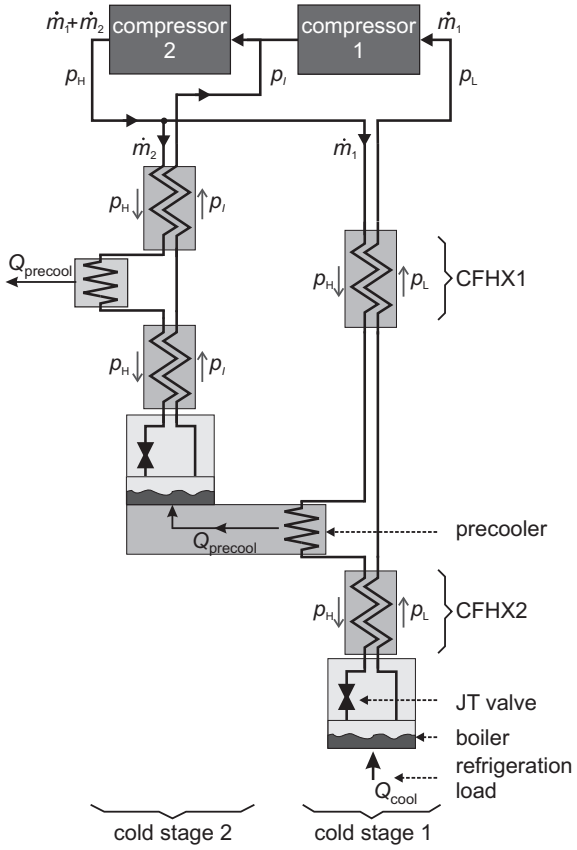

Figure 5.11: Two-stage compressor with an integrated JT precooler. The high-pressure gas p_H from the second compression stage is expanded to the intermediate pressure p_I. This expansion stage (number 2 in the figure) precools another expansion stage (number 1) in which high-pressure gas p_H is expanded to the low pressure p_L.

The enthalpies of (pre)cooling result from a similar analysis as above. In case a Joule-Thomson precooler is applied, the mass flows through both compressor stages differ. A mass flow $\dot{m}_1$ is supplied by the first stage compressor and a mass flow $\dot{m}_1 + \dot{m}_2$ by that of the second stage. These mass flows are related as the precooling of cold stage 1 is performed by cold stage 2.

$$\dot{m}_1 |\Delta h_{prec1}| = \dot{m}_2 \Delta h_{cool2} \tag{5.34}$$

The numbers refer to the numbers in figure 5.11. Rewriting of equation (5.34) yields

$$\frac{m_{s2}/t_{cycle2}}{m_{s1}/t_{cycle1}} = \frac{\Delta x_{net1}}{\Delta x_{net2}} \left(1 + \frac{|\Delta h_{prec1}|}{\Delta h_{cool2}} \right) \tag{5.35}$$

The COP of the cooler can be derived in a similar way as above and results as

$$COP_{cooler} = \frac{\Delta h_{cool1}}{\frac{p_{input1}}{\Delta x_{net1}} + \frac{p_{input2}}{\Delta x_{net2}}(1 + \frac{|\Delta h_{prec1}|}{\Delta h_{cool2}}) + \frac{|\Delta h_{prec1}|}{COP_{prec}} \frac{|\Delta h_{prec2}|}{\Delta h_{cool2}}} \tag{5.36}$$

The design from figure 5.11 is in fact a superposition of a two-stage compressor operating between p_L and p_H with a flow $\dot{m}_1$ through both compressor stages and a separate, additional, compressor stage with a flow $\dot{m}_2$ that operates from p_I to p_H and performs the precooling. The efficiency of this design can always be higher than the design with the internal JT-precooler where the intermediate pressure has a double function. It determines both the precool temperature and the compressor efficiency. The split design has an additional degree of freedom: the choice of the low pressure in the additional stage. By proper design, this results in a larger COP, at the cost of an additional compressor.

Optimum cooler efficiencies

Optimum cooler efficiencies were determined for four configurations: coolers with a single-stage compressor and a two-stage compressor both with a TE-precooled cold stage, a two-stage compressor with an internal JT precooler, and a two-stage compressor with an external precooler, i.e. a single-stage sorption compressor coupled to a LH cold stage that precools the high-pressure gas from the two-stage compressor. Nitrogen was taken as the working gas. The compressor low temperatures T_{L1} and T_{L2} were set at 293 K. The operating temperatures of the thermo-electric coolers that were used to precool the high-pressure gas were not optimised and their operating temperatures were set to 240 K. The other parameters, i.e. T_{H1}, T_{H2}, p_I and p_H were optimised. The results are shown in figure 5.12.

The adsorbed amount of gas increases when the low pressure goes up. As a result, for all configurations, the cooler efficiencies increase with increasing low pressure. For a basic two-stage compressor, the optimum high pressure increases as the low-pressure increases, resulting in a higher COP of the cold stage as can be observed in figure 5.10. In case of an internal JT precooler, the efficiency increase flattens for higher low pressures. Such an internal JT precooler is only attractive if the intermediate pressure is lower than the critical pressure. Then, the high-pressure gas p_H is liquefied in the precooler. This poses an upper limit to the intermediate pressure and the increase in cooler COP for the higher low pressures is only caused by the increase in the COP of the first compression stage caused by the higher amount of adsorbed gas and the smaller pressure swing. The COP increase of the two-stage compressor with an external precooler also flattens. A high pressure larger than the

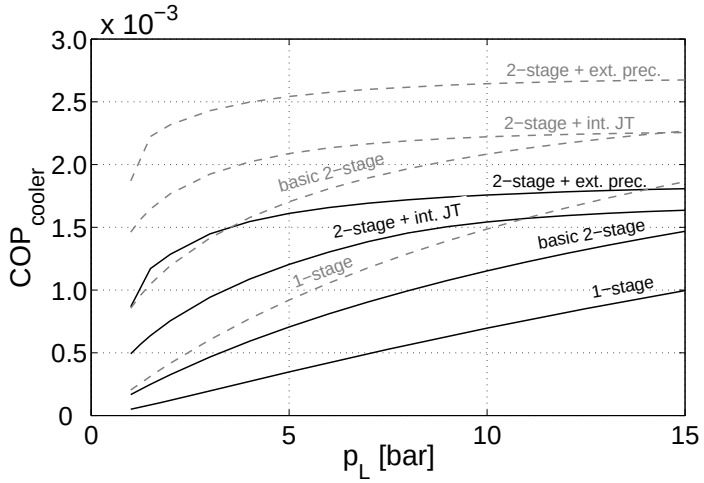

Figure 5.12: Optimised cooler efficiencies for four cooler configurations: single-stage and two-stage compression with a LH cold stage precooled with a TE cooler (denoted as 1-stage and basic 2-stage, respectively), two-stage compression with an internal JT precooler (2-stage + int. JT), and two-stage compression with an external sorption compressor with a TE-precooled LH cold stage (2-stage + ext. prec). All configurations were calculated with both Maxsorb (black straight lines) and Saran (grey dashed lines) activated carbon with nitrogen as the working gas. A heat sink temperature of 293 K was taken. The temperature of the TE cooler was not optimised and its operating temperature was set to 240 K.

critical pressure of 34 bar is not attractive. It decreases the COP of the compressor whereas the cooling power hardly increases as the majority of cooling power results from the precooling.

A low pressure of 1 bar results in a cold-stage temperature of 77.2 K. In case of Maxsorb activated carbon and single-stage compression, the cooler efficiency is only 0.014% of Carnot. Application of two-stage compression results in an efficiency increase of more than a factor 3 whereas addition of an internal JT precooler even results in an efficiency increase of nearly a factor 10 compared to the single-stage compressor. Similar efficiency improvements are obtained when Saran is used as the sorber material. With this sorber, a two-stage compressor and an external JT precooler has an efficiency of 0.53% of Carnot, nearly 40 times better than single-stage compression with Maxsorb. When compared to other types of coolers, this efficiency is still low as can be seen in figure 3.1. However, the cooler type under investigation will generally not be selected for its efficiency but for one of its other features like its low-vibration level or the possibility for scaling to small sizes.

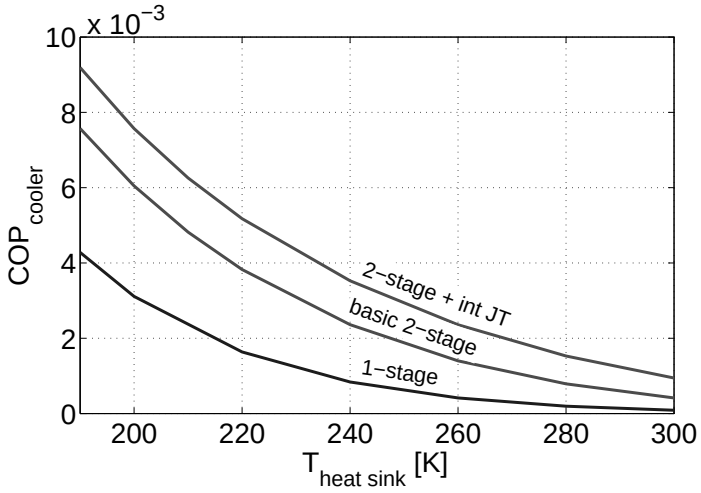

Figure 5.13: Influence of the heat sink temperature on the cooler efficiency for Saran with nitrogen as the working gas and a fixed low pressure of 1 bar. The compressor operating conditions were optimised for each heat sink temperature. External precooling was not applied.

The heat sink temperature has a large effect on the efficiency of the cooler. When the heat sink temperature is lowered, considerably more gas is adsorbed at a specific pressure, and the efficiency goes up. This is illustrated in figure 5.13. The figure shows optimised cooler efficiencies for heat sink temperatures ranging from 190 K to 300 K. Saran was taken as the sorber material and nitrogen as the working gas. The low pressure was kept fixed at 1 bar. External precooling was not applied.

5.3 Conclusions

The efficiency of a sorption compressor can be increased by two-stage compression. Each compressor has a smaller pressure swing and less gas is lost in the void volume. Besides, the second stage compressor starts at a higher pressure at which considerably more gas is adsorbed. A theoretical optimisation of the compressor efficiency showed that by application of two-stage compression considerably higher pressures can be reached compared to the single-stage design. This is beneficial as, within some limits, a higher pressure before expansion yields a higher cold stage efficiency. The efficiency of the cold stage can largely be increased by precooling the high-pressure gas, e.g. with a TE precooler. The enthalpy of precooling directly adds to the cooling

enthalpy. Precooling is therefore especially attractive when the high-pressure gas is liquefied in the precooler. For gases like nitrogen, argon and krypton, this cannot be achieved from room temperature with a TE cooler as temperatures below the critical temperature of the gas are then required. These temperatures can be achieved with a precooler that consists of a sorption compressor and a cold stage that has a low pressure smaller than the critical pressure of the working gas*. When two-stage compression is applied, this precooler can also be integrated by expanding high-pressure gas from the second stage to the intermediate pressure. This saves a sorption compressor cell at the cost of some efficiency.

At a low pressure of 1 bar, a heat sink temperature of 293 K, and use of Maxsorb as the sorber and nitrogen as the working gas, the cooler efficiency can be increased with a factor 3 by application of two-stage compression. Another factor 3 is obtained by using an internal JT precooler. Application of an external JT precooler gives a further improvement with nearly a factor 2, resulting in a 17 times larger efficiency compared to single-stage compression. Similar improvements can be achieved with Saran as the sorber material. Two-stage compression with an external JT precooler with Saran gives a 37 times larger efficiency than a single-stage compressor filled with Maxsorb.

References

[1] L. Duband. *Etude et réalisation d'une machine frigorifique à cycle de Joule-Thomson, utilisant un compresseur thermique à adsorption.* PhD thesis, USTM Grenoble, 1987.

[2] Suhanan, L. Duband, A. Ravex, and M. L. Feidt. Etude expérimentale d'un réfrigérateur Azote à cycle Joule Thomson à adsorption. In *XIXth International Congress of Refrigeration*, volume IIIb, pages 1247–1255, 1995.

[3] S. Bard. Improving adsorption cryocoolers by multi-stage compression and reducing void volume. *Cryogenics*, 26:450 – 458, 1986.

[4] J. F. Burger. *Cryogenic Microcooling, A micromachined cold stage operating with a sorption compressor in a vapor compression cycle*. PhD thesis, University of Twente, The Netherlands, 1987. downloadable from: http://purl.org/utwente/23470.

[5] A. Bejan. *Advanced Engineering Thermodynamics*. Wiley Interscience, 1988.

[6] J. F. Burger and H. J. M. ter Brake. 4 K sorption cooler for the Darwin mission - preliminary study. Final report, ESA Contract number 14957, August 2001.

[7] G. Berndt. *Taschenbuch Maschinenbau*. Verlag Technik, Berlin, 1965.

*In principle, also another working gas can be selected as long as the cold-stage temperature of the precooler is lower than the critical temperature of the working gas of the two-stage compressor.

[8] F. Rouquerol, J. Rouquerol, and K. Sing. *Adsorption by powders & porous solids: principles, methodology and applications*. Academic press, London, UK, 1999.

[9] T. Otowa, R. Tanibata, and M. Itoh. Production and adsorption characteristics of MAXSORB: high-surface-area active carbon. *Gas separation & purification*, 7(3):241–245, 1993.

[10] The Kansai Coke & Chemicals Co. Ltd., 1-1 Oh-Hama, Amagasaki, Japan 660.

[11] A. Yavrouian and H. Schember. Saran carbon sorbent development for sorption cryocooler use. Technical report, Jet Propulsion Laboratory, California Institute of Technology, Pasadena, California, USA, 1990.

[12] L. C. Yang, T. D. Vo, and H. H. Burris. Nitrogen adsorption isotherms for zeolite and activated carbon. *Cryogenics*, 22:625–634, 1982.

[13] V. C. Menon and S. Komarneni. Porous adsorbents for vehicular natural gas storage: A review. *Journal of Porous Materials*, 5:4358, 1998.

[14] R. T. Yang. *Gas separation by adsorption processes*. Imperial College Press, London, United Kingdom, 1987.

[15] M. M. Dubinin. The potential theory of adsorption of gases and vapors for adsorbents with energetically nonuniform surfaces. *Chem. Review.*, 60:235–241, 1960.

[16] R. T. Yang. *Adsorbents: fundamentals and applications*. John Wiley & Sons, Hoboken, NJ, USA, 2003.

[17] F. D. Maslan, M. Altman, and E. R. Aberth. Prediction of gas-adsorbent equilibria. *J. of Phys. Chem.*, 57:106–109, 1953.

[18] Private communication with Jet Propulsion Laboratory, Pasadena, California 91109, USA, 1992.

[19] MPDB Material Property Database, JAHM Software, Inc. 29 Valley Rd, North Reading, MA 01864-1740, USA.

[20] Cryodata Inc., P.O. box 558, Niwot, CO 80544, USA, http://www.cryodata.com.

[21] N. D. Banker, K. Srinivasan, and M. Prasad. Performance analysis of activated carbon + HFC-134a adsorption coolers. *Carbon*, 42:117–127, 2004.

[22] G. Walker. *Miniature refrigerators for cryogenic sensors and cold electronics*. Clarendon Press, 1989.

[23] J. Lester. Closed cycle hybrid cryocooler combining the Joule-Thomson cycle with thermoelectric coolers. In *Advances in Cryogenic Engineering*, volume 35, pages 1335–1340, 1990.

[24] Melcor Corporation, 1040 Spruce Street, Trenton, NJ 08648, USA, http://www.melcor.com.

Chapter 6

Single-cell compressor unit

6.1 Design of a single-stage single-cell compressor unit

A small sorption compressor operating at the cooled semiconductor stage is an attractive cooling option for the THz demonstrater as was discussed in section 1.1. For practical reasons, it was decided to explore the single-cell compressor design at room temperature. Section 6.1 describes the design of the set-up that was used to test the proposed compressor design. The buffers that will be applied can be simple 'empty' buffers. A considerable reduction in buffer sizes and pressure variations can be achieved when the buffers are filled with a sorber material. This will be discussed in detail in section 6.1.6. The operation of the compressor is described in section 6.2. The first part of this section describes the time-dependent behaviour of pressures and mass flows in the system. Also the application of several buffer types is discussed. This chapter only addresses the compressor part of the cooler. Therefore, in section 6.2.2 the expected implications of the compressor design on the cold stage will be discussed. In section 6.2.3, the single-cell design is compared with the conventional design as described in chapter 1. Besides, the results of an experimental sensitivity analysis on the most important control parameters are described. The chapter ends with conclusions on the proposed compressor design.

6.1.1 Thermodynamical set points

To investigate the operation of the single-cell sorption compressor, we selected xenon as the working gas. This gas adsorbs reasonably well on carbon at room temperature while at the same time a relatively low temperature of 165 K can be reached for a

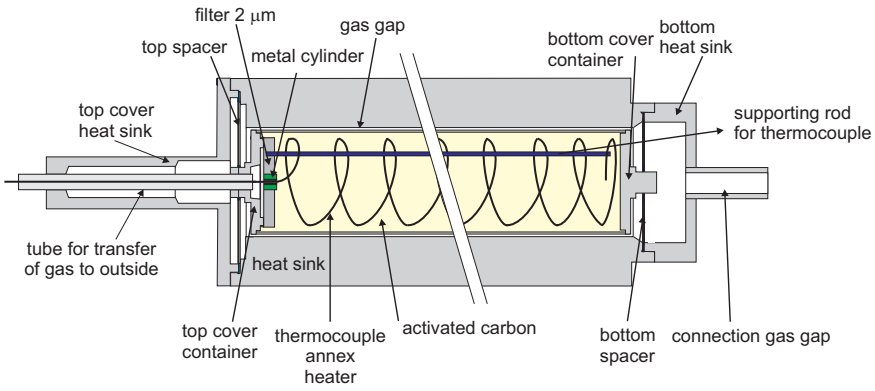

Figure 6.1: Schematic drawing of the sorption compressor cell.

compressor low pressure of 1 bar. A thermo-electric cooler can be applied to precool and condense the high-pressure gas. Such a TE cooler increases the efficiency of the sorption compressor combined with the LH cold stage without compromising its advantages over other types of coolers. Precooling of the high-pressure gas is useful as the enthalpy related to the gas-liquid phase change adds to the enthalpy of cooling (section 5.2.2). To liquefy the gas in the precooler, the high-pressure gas should be precooled below the temperature at which the gas-liquid phase transition takes place at that pressure, e.g. by means of a 2-stage TE cooler [1]. For xenon, this implies a compressor high pressure in the range of 16 - 19 bar when the gas is precooled to 235 - 240 K. Of course, the selection of the working fluid and the thermodynamic setpoints is rather arbitrary. Also other gases can be taken depending on the requirements of the cooler.

To test the compressor performance, the experiments were performed without a cold stage. Instead, a tunable needle valve was used to establish the required pressure drop. Section 6.2.2 gives a theoretical description of the expected behaviour of a LH cold stage, if it were connected to the compressor type under investigation.

6.1.2 Sorption compressor cell

The design of the compressor cell is shown schematically in figure 6.1. The cell consists of a container that is filled with a sorber material. The sorber container has an inner diameter of 9.4 mm and a length of 10 cm. It was filled with commercially available Maxsorb MSC-30 activated carbon [2]. This sorber material has a surface area of 3290 m^2/g and an apparent density of 0.28 g/ml [2, 3]. The charcoal was

filtered and particles with a diameter between 210 - 420 μm were selected. The void volume between the filter of the sorption compressor cell and the check valves is estimated at 2 cm^3. The internal void volume is about 6 cm^3. Application of other activated carbons with inherently lower void volume fractions would improve the pressure swing that can be achieved as less gas is lost in the void volume. However, such a sorber is not needed to investigate the operation of the single-cell compressor. The sorber container is closed by a 2 μm stainless steel filter. In this filter, a feedthrough for an Omega [4] E-type thermocouple was welded. This thermocouple is used both for sensing the temperature and as a heating element. While thermally cycling the sorber container, the thermocouple is switched between the heating mode and the sensing mode. The sorber container is gold-plated to reduce radiative heat loss and it is centred in a stainless steel heat sink by means of two spacers. The described compressor cells were originally designed for a different project. The same design was used as the majority of parts were readily available. For a more detailed description of the compressor cell, the reader is referred to Burger *et al*. [5].

The sorption compressor cell from figure 6.1 was heat sunk at 20 °C. The pressure in the sorber container is measured outside the cell with a low void-volume Kulite pressure sensor (type XTL-190) [6]. The temperature of the heat sink and that of the 'cold junction' of the thermocouple were monitored with Heraeus PT1000-resistors [7]. Valco filters with 10 μm screens were applied before and after the check valves [8]. They have a pressure drop of about 30 mbar with a xenon flow of 4 mg/s and an absolute pressure of about 1.5 bar.

6.1.3 Gas-gap heat switch

As is shown in figure 6.1, we applied a gas-gap heat switch in our design. The heat transfer through such a gap depends on the pressure in the gap, the dimensions of the gap and on the properties of the gas that is applied. The pressure dependence is used to switch the thermal contact [9–11]. A separate sorption compressor cell that is integrated in the gas-gap can be used as an actuator. This unit can e.g. be a metal-hydride acting as a sorber material with H_2 as the working gas [11, 12]. To test the compressor operation in a laboratory set-up, we created the pressure swing in the gas-gap by switching the gas-gap volume between a low-pressure and a high-pressure 'reservoir' with the help of two active valves. This, and the other components of the experimental set-up, is shown schematically in figure 6.2. For safety reasons, we selected helium as the working gas despite the slightly worse heat transfer characteristics compared to hydrogen. Note that the switching speed of an integrated sorption compressor unit that is used to actuate the pressure in the gas-

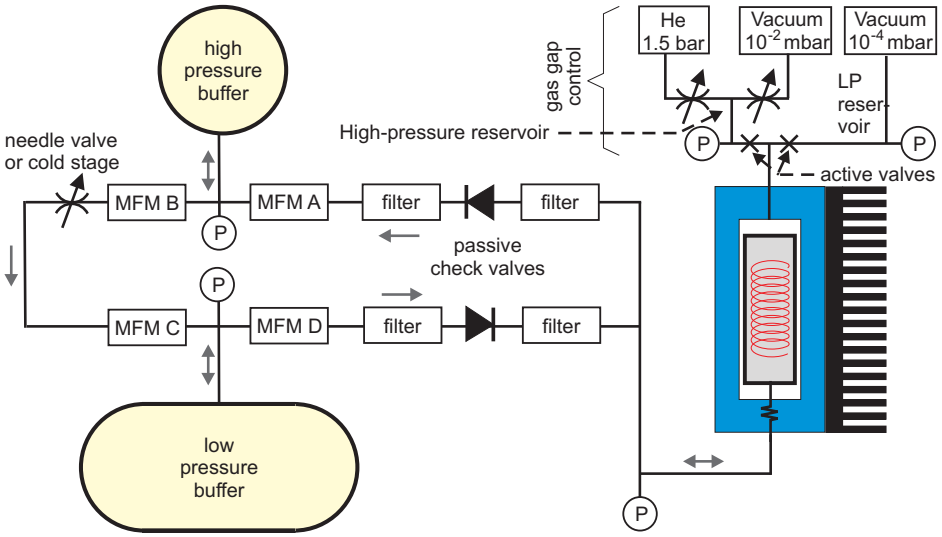

Figure 6.2: Schematic overview of the experimental set-up. See text for details. 'MFM' stands for mass flow meter, a 'P' indicates the position of a pressure sensor.

gap is probably slower than the current solution. This can substantially affect the compressor operation.

A gas-gap high pressure of 50 mbar was selected. At this pressure, the gas in the gap is nearly in the viscous regime. For the low-pressure, $5{\cdot}10^{-4}$ mbar was taken. This is the lowest pressure the vacuum pump, pumping the low-pressure reservoir, could achieve. The cooldown behaviour of the sorber container was measured for a range of pressures. From this, the pressure-dependent thermal resistance was determined. This was fitted to theory [9–11] by using the accommodation coefficient as the fitting parameter. For the selected pressures, the thermal resistance switches between $4{\cdot}10^{3}$ K/W during the heating phases and 0.5 K/W during the cooling phases. The pressures in both the high-pressure and the low-pressure reservoirs connected to the gap space were measured with MKS Baratron 627B pressure transducers [13].

6.1.4 Check valves

The check valves in the compressor should have a negligible leak compared to the amount of gas that is pumped by the compressor cell. Furthermore, the pressure drop over the check valves is not available for expansion in the cold stage and should be small. The pressure difference over the valve that is needed for it to open, is called

the cracking pressure. At the high-pressure side, the pressure in the compressor cell should be higher than the actual pressure of the high-pressure buffer plus this cracking pressure before the valve opens. Something similar happens at the low-pressure side. When the check valve has opened, the pressure difference over the valve depends on the mass flow. The check valve closes when the pressure difference becomes smaller than the so-called reseal pressure. A positive reseal pressure gives a loss as this part of the pressure difference that is created by the compressor cannot be used in the expansion. A negative reseal pressure also gives a loss as some leak will occur just before the valve closes. The reseal pressure should, therefore, preferably be zero. A stringent requirement for the cracking pressure cannot be defined. A value on the order of the pressure variations in the buffers seems appropriate. Another issue is the volume inside the valve on the side of the compressor cell. This volume adds to the void volume of that cell and reduces the efficiency of the compressor as was discussed in section 5.2.1. Application of microminiature check valves [14] can tackle this void volume problem. In the present set-up, these valves were not applied because of the time and cost of manufacturing, whereas low-void volume valves are not essential to study the behaviour of the compressor concept. It was decided to select a directly available check valve, at the cost of a relatively large void volume in the valve.

A set-up was built to characterise leak flow, pressure drop, and cracking pressure of check valves. A schematic picture of this set-up is shown in figure 6.3. To measure the cracking pressure, first a slight overpressure was created in volume 1 with respect to volume 2 to ensure that the check valve was closed. After that, the pressure in volume 2 was increased very slowly via mass flow controller A and active valve 6 while active valves 1 and 4 were kept closed. The pressure difference at which the pressure in volume 1 started to rise was taken as the cracking pressure. The measurement of the mass flow dependent pressure drop was performed with a gas flow along the dashed line in the figure. The flow through the check valve was controlled by mass flow controller B.

The two check valves in the compressor close at different absolute pressures. The leak flow may differ in these two situations because of the much higher density of the gas at the high-pressure side. The set-up can measure the leak flow at both pressures. The leak flow measurement for the valve on the low-pressure side is performed with active valve 1 and the valves in mass flow controllers C and D fully opened. The pressure in volume 1 is increased with a selectable rate by controlling the flow through mass flow controller A. The leak is measured with the very sensitive mass flow controller C. A different routine was used to test the leak flow for the check valve on the high-pressure side. Volume 1 and 2 were first filled to the required high pressure. Then, the pressure in volume 2 was reduced over active valve 3 and

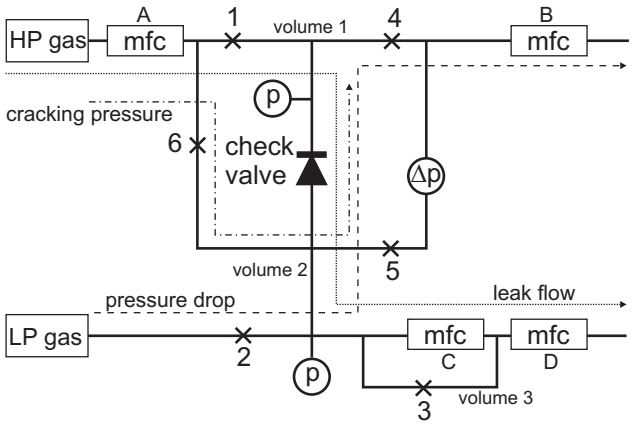

Figure 6.3: Check valve characterisation set-up that is suitable to determine cracking pressure, pressure drop and leak flow of a check valve. 'mfc' stands for 'mass flow controller' whereas 'HP gas' and 'LP gas' refer to a gas bottle operated at a high pressure and low pressure respectively. The active valves are shown by crosses. The operation of the set-up is explained in the text.

mass flow controller D in steps. After every pressure reduction, valve 3 and mass flow controller D were closed again. After stabilisation of the system, the leak flow through mass flow controller C gives a measure of the leak flow through the valve. To ensure a proper measurement of the leak flow in this situation, volume 3 is 5 times larger than volume 2. Prior to the described procedure for both types of leak flow measurements, a forward flow was fed through the check valve under test to ensure the same starting point for each measurement.

The measured values were recorded with a National Instruments data-acquisition card [15]. A custom written LabVIEW program [15] was used for data processing and to control the active valves and the mass flow controllers. In this way, reproducible measurements could be done. Druck PTX1400 sensors [16] were used for the absolute pressure measurements whereas a SensorTechnics HCX series pressure transducer [17] was applied to measure the differential pressure over the valve. The used mass flow controllers were of Bronkhorsts EL-FLOW series [18].

Some promising Swagelok [19] check valves were tested and the Swagelok 6L-CW4S4 valves turned out to have the smallest leak in combination with a low cracking pressure. These are all-welded check valves with a fluorocarbon coating on the poppet. The cracking pressure was measured with nitrogen gas. A back pressure of 0.2 bar was realised prior to the measurement. The pressure on the forward side of the valve was increased with 1.3 mbar/s. A cracking pressure of 12 mbar was found.

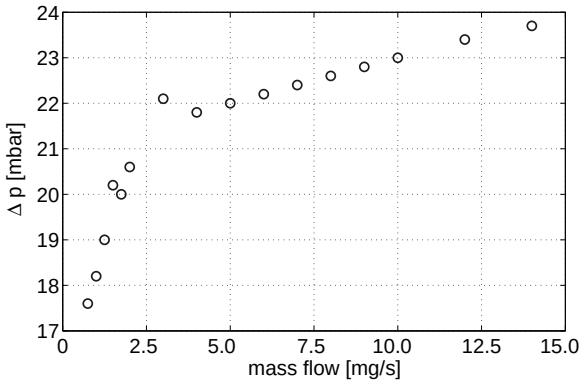

Figure 6.4: Mass flow dependent pressure drop over the Swagelok 6L-CW4S4 check valve for typical flows in the sorption compressor set-up for xenon gas with an absolute pressure around 1.5 bar.

The pressure drop was measured with xenon gas with an absolute pressure of about 1.5 bar. The results are shown in figure 6.4. The maximum error of the sensor is 2 mbar. The values are considerably smaller than the pressure difference created by the compressor and is thus acceptable. The pressure drop over the valve at the high-pressure side will be even smaller as for a given geometry the pressure drop scales with μ/ρ [20]. This implies a pressure drop that is about a factor 18 lower [21].

The pressure of the compressor cell rises with a rate of about 0.075 bar/s during phase A of the sorption cycle. At this rate, in total 0.3 mg gas leaks through the valve before the leak flow falls below 1 μg/s, the noise level of the mass flow meter. This leak is acceptable compared to the total forward flow during a cycle, which is a few hundred milligrams. In phase C, the check valve on the high-pressure side closes when the pressure in the cell drops. Also here, the leak flow is smaller than the noise level of the sensor. Probably, a small amount of gas leaks through the valve before it closes. This initial leak could not be measured with the current set-up, but as the check valve seems to close, it is reasonable to assume that also this leak is negligible compared to the forward flow. The void volume on the compressor side of the check valve was filled with metal, reducing it from about 0.5 cm^3 to about 0.2 cm^3 for each valve.

6.1.5 System control algorithm and instrumentation

To obtain the maximum achievable pressure difference for a fixed value of the flow restriction, the compressor cell should pump as much as possible gas from the low-pressure buffer to the high-pressure buffer in an as short as possible cycle time. The heating phases can be speeded up by increasing the compressor input power and the duty cycle, i.e. the fraction of time in the heating phases during which the heater is turned on. However, as the thermal conductivity of charcoal powder is low, fast heating implies a considerable temperature profile over the heater. It results from figure 1.2a that $\partial^2 x_s/\partial T^2$ is positive, with x_s being the amount of gas adsorbed per gram of sorber material. Then, a temperature profile over the sorber material results in less desorption compared to the case of a uniform temperature with the same energy input to the sorber. Although a temperature gradient is not necessarily problematic for the pressure swing, it can reduce the compressor efficiency dramatically. If one aims at a maximum pressure difference, the compressor should be switched to the cooling mode when the additional amount of gas flown to the high-pressure buffer does not compensate the additional cycle time that is needed. This is definitely the case when the flow to the high-pressure buffer becomes lower than the flow through the restriction. For a compressor design with a gas-gap heat switch, the fastest cool down rate is obtained when the gas in the gap is in the viscous state. Similar to the heating phases, the cooling should be continued until the additional amount of gas that flows to the cell does not compensate the additional time needed.

In our set-up we use a single spirally-wound heater. To limit the temperature profile and to perform the heating phase as fast as possible, the control algorithm initially heats the sorber container with a duty cycle of 85%. Each time the thermocouple is switched to the sensing mode, the observed temperature reduces rapidly as the energy distributes more uniformly over the sorber material. When the set maximum temperature is reached, the duty cycle is reduced with 5%. When the heater is switched on again, it will take some time before the set maximum temperature is reached again as the duty cycle has been reduced. Then, the duty cycle is again reduced with 5% and so on. The compressor is switched to the cooling mode when the flow to the high-pressure buffer has become smaller than a factor f_{BC} times the flow through the needle valve. During the cooling phase, the heater is switched off and the gas-gap is switched to the selected high pressure. Similar to the heating phase, the cooling is continued until the flow from the low-pressure buffer to the cell has become lower than a factor f_{DA} times the flow through the needle valve.

The control algorithm was implemented in a LabVIEW programme [15]. The pressures of the high and low-pressure buffers are measured with Druck PTX1400

sensors [16]. The mass flows between the buffers and the sorption compressor cell and between the buffers and the flow restriction are measured with Bronkhorst EL-FLOW mass flow meters [18]. The data are sampled with a National Instruments multiplexer board connected to an E-series DAQ-card [15]. Each channel is sampled with 100 Hz and averaged over 50 samples before the data was further processed. The thermocouple data form an exception to this, as the moment the thermocouple is switched between the heating and the sensing mode is not synchronised with the start of the averaging intervals.

6.1.6 Buffer volumes

Basic buffers

The simplest buffer type is an 'empty' volume. The pressure variations in such buffers connected to the compressor cell depend on the mass flow through the needle valve, the cycle time and the volume as expressed in equation (6.1).

$$\Delta p = \frac{\dot{m}_{cool} RT}{VM}(t_{cycle} - t_{flow}) \tag{6.1}$$

Here, Δp is the pressure variation in the buffer, $\dot{m}_{cool}$ the average mass flow through the needle valve, R the universal gas constant, T the absolute temperature of the buffer, V the buffer volume, M the mole mass of the working fluid, t_{cycle} the cycle time and t_{flow} the period during which there is a gas flow between the compressor cell and the buffer under consideration. This formula only holds for relatively small pressure variations. Furthermore, the flow through the restriction should not exceed the flow between the cell and the buffer. A volume of 300 cm^3 was selected for the low-pressure buffer whereas for the high-pressure buffer a volume of 50 cm^3 was taken. A cycle time of 10 minutes with 2.5 minutes for each flow phase and a flow $\dot{m}_{cool}$ of 0.5 mg/s then results in a pressure variation in the low-pressure buffer of 0.14 bar and 0.86 bar for the high-pressure buffer.

Sorption-based buffers

To reduce the pressure variation or to reduce the size of the buffers, it is beneficial to use buffers that are filled with a sorber material. When an amount of gas flows into a buffer that is filled with an adsorbent, the pressure in the buffer tends to rise, disturbing the equilibrium between the amount of gas that is adsorbed and the amount of gas in the void volume. As a reaction, the sorber will start adsorbing gas. This counteracts the pressure increase and at the same time the temperature

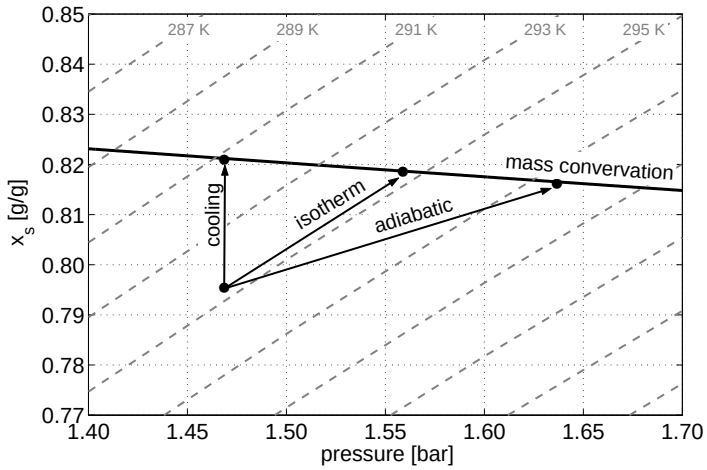

Figure 6.5: Behaviour of a sorption-based buffer upon an incoming amount of gas. The dashed lines are sorption isotherms. See text for details.

rises as heat becomes available in the adsorption process. This continues until a new equilibrium is reached. This process is shown graphically in figure 6.5. Consider the low-pressure buffer at the end of phase D (see figure 1.2a) of the sorption cycle, so the buffer is at its minimum pressure and the low-pressure check-valve has just closed. Assume that, initially, the pressure is at 1.47 bar and the buffer is at a temperature of 294.5 K. During phase A to C, a certain amount of gas flows into the buffer. The end point of temperature and pressure will be somewhere on the mass conservation line, the straight line in the figure. The temperature at the end of phase C depends on the thermal contact of the buffer with the surroundings. The two extreme cases, isothermal and adiabatic, are drawn with arrows. It is clear that the isothermal case is preferable as this gives the smallest pressure variation. During phase D, a nett amount of gas flows out of the buffer and the reverse process happens.

In the isothermal case, the heat of adsorption is directly given off to the environment. The pressure variation in the buffer can be determined from the mass balance

$$m_s x_s(T_i, p_i) + \frac{p_i[V^*_{void}(T_i, p_i) + V_{extern}]M}{RT_i} + m_{gas,in} = m_s x_s(T_f, p_f) + \frac{p_f[V^*_{void}(T_f, p_f) + V_{extern}]M}{RT_f} \tag{6.2}$$

In this equation, m_s is the mass of the sorber material in the buffer, x_s is the amount

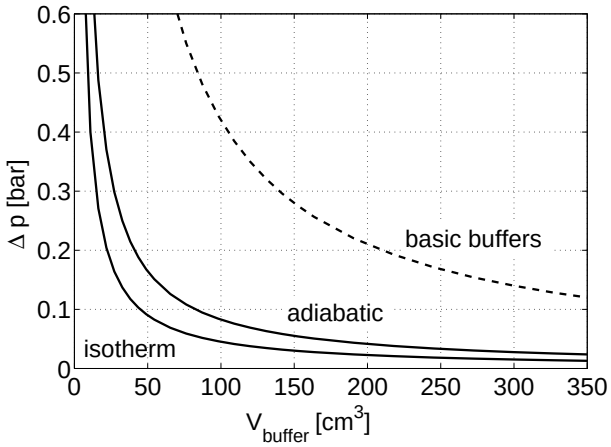

Figure 6.6: Comparison between basic buffers and sorption-based buffers for the low-pressure side. For assumptions, see text.

of gas that is adsorbed per gram of sorber material, and $m_{gas,in}$ the amount of gas that flows into the buffer. The subscript i refers to the initial situation whereas an f refers to values directly after the gas has flown to the buffer. The first term on both sides of the equal sign describes the amount of gas that is adsorbed, as described in chapter 5. The second term describes the mass in the void volume, obeying the ideal gas law. This is the external volume V_{extern} due to the tubing and the internal void volume V^*_{void} in the buffer, corrected for the volume of the adsorbed gas. For the isothermal case, the temperature does not change and the pressure variation can be determined from the mass balance only.

In the adiabatic limit, the heat of adsorption is completely used to increase the temperature of the buffer. Combination of equations (5.11), (5.16), and (5.18) and rearranging terms yields

$$m_s[x_s(T_f, p_f) - x_s(T_i, p_i)]q_{ads} = [m_s(c_{ps} + x_s(T_i, p_i)c_{p,adsgas})](T_f - T_i) \quad (6.3)$$

Because of the bad thermal conductivity of the sorber material, it is expected that the heat loss to the buffer wall is small. Therefore, the heat capacity of the wall was not included. The contribution from the free gas, equation (5.13), was neglected as this contribution is considerably smaller than the other terms. This also holds for the heat contribution resulting from temperature differences between the sorber and the incoming gas (equation (5.19)). The temperature and pressure dependencies of the heat capacities and the heat of adsorption were neglected.

Figure 6.6 compares the volume dependent pressure variation between a basic

buffer and a sorption-based buffer filled with Maxsorb activated carbon with a void volume fraction of 92%, an incoming gas of 225 mg, and an external volume of 12.5 cm^3. An initial pressure of 1.47 bar and an initial temperature of 294.5 K were assumed. The specific heat capacity of the sorber was taken as 690 J/kg/K and that of the adsorbed gas as 143 J/kg/K. The heat of sorption was determined from the isotherms according to equation (5.17) and resulted as 107 kJ/kg.

It was decided to select buffer sizes that have pressure variations comparable to those of the basic buffers, but then with a much smaller volume. An alternative would have been to leave the buffer sizes unaltered. Application of sorption-based buffers would then have resulted in a reduction of the pressure variation, as can be seen in figure 6.6. For the basic buffers, the pressure variation in the low-pressure buffer was estimated at 0.14 bar whereas that of the high-pressure buffer was estimated at 0.86 bar. A volume of 50 cm^3, 6 times smaller than that of the basic buffer, is appropriate for the low-pressure buffer (see figure 6.6). A 15 cm^3 buffer was taken for the high-pressure side whereas the volume of the basic buffer was 50 cm^3. Commercially available Swagelok stainless steel buffers were applied [19]. An Omega E-type thermocouple [4] was positioned inside the sorber material of each buffer whereas a Heraeus PT-resistance [7] was mounted on the outside of each buffer.

Active sorption-based buffers

The pressure in the sorption-based buffer can be kept constant by actively cooling the sorber when gas flows in, as is shown in figure 6.5, and by heating when gas flows out. Slight fluctuations in the high-pressure buffer are in general not problematic as the cooling power is buffered by the boiler. Application of an active buffer to the high-pressure side would needlessly degrade the compressor COP. Therefore, an active buffer approach was only considered for the low-pressure buffer.

The rates of cooling and heating have to be tuned to the incoming and outgoing gas flow rate. The drawback of such an active buffer is the additional input power to the system, reducing the efficiency of the cooler. The added input power was estimated assuming a cylindrical buffer with a length-to-diameter ratio η and a volume V that is cooled and heated from the outside with a thermo-electric (TE) cooler. The temperature decrease that is required for a given amount of gas that flows into the buffer can be derived from equation (6.2). The gas in the external void volume, mainly consisting of tubing, will not vary much in temperature due to the heating and cooling of the buffer. As the pressure is kept constant, the amount of gas in the tubing does not change. The result is that the external void volume does not

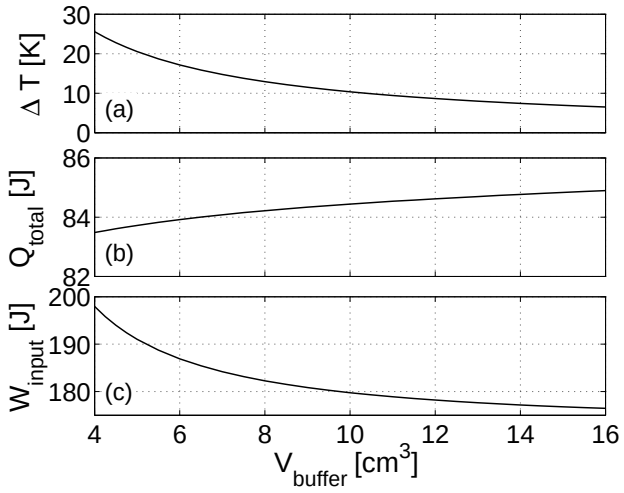

Figure 6.7: Required temperature swing (top), extracted energy (middle), and input power (bottom) for an active sorption-based buffer with varying volumes. For assumptions, see text.

influence the required temperature variation of the buffer. The larger the buffer, the more sorber material is present and the smaller the required temperature variation. This is illustrated in figure 6.7a. The same assumptions as in the previous section were taken.

Upon cool down, both the sorber material and the buffer have to be cooled. The heat capacity from the wall must therefore be added to equation (6.3). The wall and cover should withstand the internal pressure. The minimum required wall thickness t_w results from equation (5.14). The requirement on the thickness of the cover is [22]

$$\frac{t_c}{D} = \sqrt{\frac{3}{16}\frac{p_{max}}{\sigma_{max}}} \tag{6.4}$$

The heat capacity of the container is

$$C_{pc} = \rho_c c_{pc}\left[\pi t_w D^2 \eta\left(1+\frac{t_w}{D}\right)+\frac{\pi}{2}D^2 t_c\left(1+\frac{4t_w}{D}\right)\right]+2\pi t_c t_w^2 \approx \rho_c c_{pc}\pi D^3\left(\frac{\eta p_{max}}{2\sigma_{max}}+\frac{1}{8}\sqrt{\frac{3p_{max}}{\sigma_{max}}}\right) \tag{6.5}$$

When the sorber is cooled down, gas is adsorbed. The related heat that comes available also needs to be withdrawn from the buffer. The total amount of heat that needs to be extracted is

$$Q_{extract} = (C_{pc}+m_s[c_{ps}+x_s c_{p,adsgas}])\Delta T + m_s[x_s(T_f,p_f)-x_s(T_i,p_i)]q_{ads} \tag{6.6}$$

Heat loss to the environment is neglected. The variation of the total energy that needs to be removed from the buffer to achieve the required temperature variation is shown in figure 6.7b. In this calculation, the ratio p_{max}/σ_{max} was set to $2.5 \cdot 10^{-2}$ and results in wall thicknesses on the order of a few tenths of a millimeter. Lower values are sufficient to withstand the internal pressure but would make fabrication much more complex. The amount of energy that needs to be removed hardly changes with the buffer size. Apparently, the additional energy extraction because of the larger buffer size is compensated by the smaller required temperature difference.

A thermo-electric cooler will be used to cool and heat the buffer. In the cooling mode, the input to the TE cooler is

$$W_{in,cooling} = \frac{Q_{extract}}{COP_{cooler}(T_{hot}, T_{cold})} \tag{6.7}$$

whereas the input in the heating mode is

$$W_{in,heating} = \frac{Q_{extract}}{1 + COP_{cooler}(T_{hot}, T_{cold})} \tag{6.8}$$

with T_{hot} the warm side of the TE cooler and T_{cold} its cold side. The efficiency of the TE cooler strongly depends on the temperatures of the hot and cold sides [1, 23]. Upon cool down, this temperature difference increases and the COP of the cooler goes down rapidly. The model assumes that the hot end of the TE cooler is perfectly heat sunk at the initial temperature of the buffer (294.5 K). The reduction in COP is accounted for by assuming that the amount of heat that needs to be extracted is linear with the temperature difference. The temperature dependent COP-data were derived from data of recent Marlow TE coolers [1]. The total heat input to the TE cooler during one cycle as a function of buffer size is shown in figure 6.7c.

A buffer volume size of 10 cm^3 was selected. According to figure 6.7c, the required heat input reduces only slightly for larger buffers. This size is also comparable to that of the compressor cell. For practical reasons, a commercially available stainless steel Swagelok buffer volume with an outer diameter of 25 mm was applied [19]. This had the disadvantage of an extremely thick wall of 1.7 mm. The buffer was put into an aluminum block of 30 x 30 x 30 cm^3 to ensure a good thermal contact to a Marlow DT6-4 20 W TE cooler [1] which was mounted on top. The cooler was heat sunk with a force cooled Marston heat sink with a thermal resistance of 0.2 K/W [24]. The temperature on the inside of the buffer was again measured with an Omega E-type thermocouple [4]. The temperature on the outside of the aluminum was measured with a Heraeus PT-1000 sensor [7]. For the high-pressure buffer, the passive buffer from the previous section was applied.

Buffer type	Volume [cm^3]	
	low-pressure	high-pressure
basic	300	50
passive sorption-based	50	15
active sorption-based	10	n.a.

Table 6.1: Overview of selected buffer sizes for the different buffer types.

Conclusions

The most simple buffers that can be used in the single-cell design are 'empty' volumes. The disadvantage of this buffer type is that the required sizes to keep the pressure variations at an acceptable level are very large compared to the compressor volume of about 8 cm^3. The sizes of the buffers can be reduced by filling them with a sorber material. Alternatively, application of a sorber in the buffers and unchanged buffer sizes will result in smaller pressure variations. In this thesis, the buffer sizes of the passive sorption-based buffers were selected in such a way that the pressure variations would be similar to that of the basic buffers with reduced buffer volumes. The pressures in the buffers can be kept constant by application of active sorption-based buffers at the cost of some additional input power. Slight fluctuations in the high-pressure buffer are in general not problematic as the cooling power is buffered in the boiler. Therefore, an active buffer will only be applied to the low-pressure side. A summary of the used buffer types and its sizes is given in table 6.1

6.2 Results and discussion

6.2.1 Compressor operation

Compressor operation with basic buffers

The compressor was operated for more than 200 cycles with f_{BC} set to 1.0, f_{DA} set to 1.2, a peak heater input power of 7.0 W, and a set maximum temperature of 700 K. As defined in section 6.1.5, f_{BC} is the ratio between the mass flow to the high-pressure buffer and that through the cold stage at which the heater is turned off and the compressor is switched to cooling mode. The factor f_{DA} was defined in a similar way for the low-pressure buffer. The flow restriction was set at such a value that the high pressure was above 16 bar, the pressure needed to condense the gas in the precooler. We aimed at a value close to atmospheric pressure for the low-pressure side. The behaviour of the system during 4 typical cycles is shown in figure 6.8. The heat input

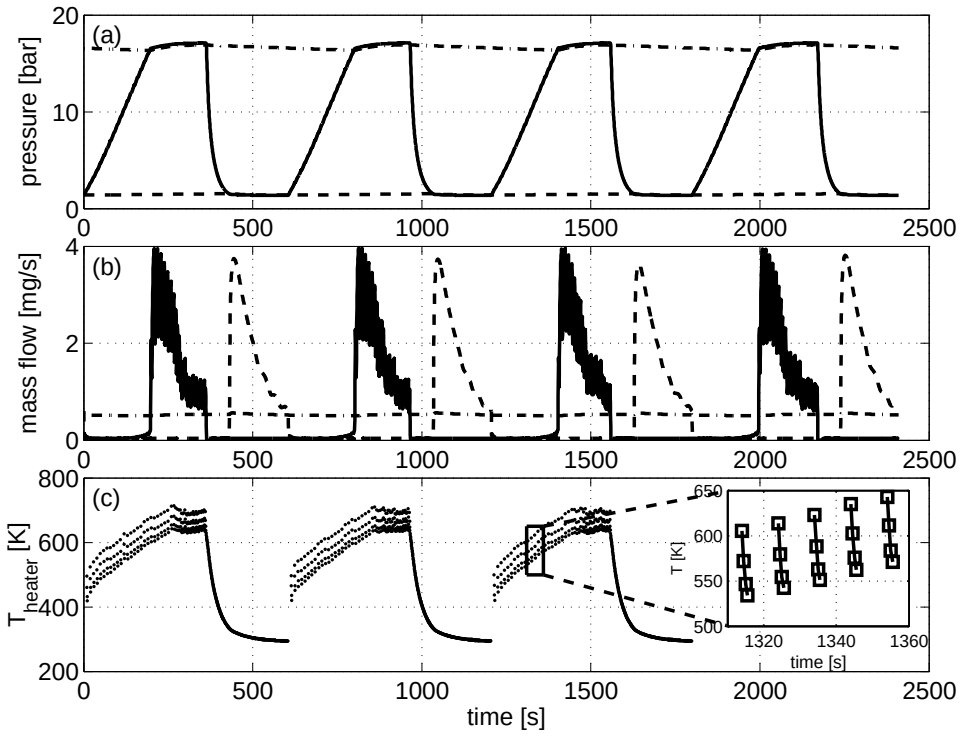

Figure 6.8: Operation of a single-cell compressor (a) Pressure versus time; p_{cell} (solid), $p_{LP,buffer}$ (dashed), $p_{HP,buffer}$ (dash-dotted). (b) Mass flow versus time; cell to HP$_{buffer}$ (solid), flow through restriction (dash-dotted), LP$_{buffer}$ to cell (dashed). (c) T_{heater} versus time. The measured temperatures are shown as dots (see inset). In the heating mode, the temperature cannot be measured. In the sensing mode, the temperature of the thermocouple decreases because heat flows to the surrounding charcoal.

averaged over the total cycle was 3.2 W. The pressure in the container alternated between 1.35 and 17.2 bar. The high-pressure buffer fluctuated between 16.4 and 17.0 bar and that of the low-pressure buffer varied between 1.39 bar and 1.53 bar. These pressure values varied less than 2% over the 200 cycles. The temperature of the heat sink around the compressor cell was kept constant at 293 K. The temperature of the other components varied slightly because of temperature fluctuations in the laboratory. The average mass flow through the flow restriction was 0.52 mg/s. The broad band in the mass flow from the cell to the high-pressure buffer is caused by the intermittent heating during phase B. The average times of the phases in stable operation are 199 s for phase A, 159 s for phase B, 72 s for phase C and 168 s for

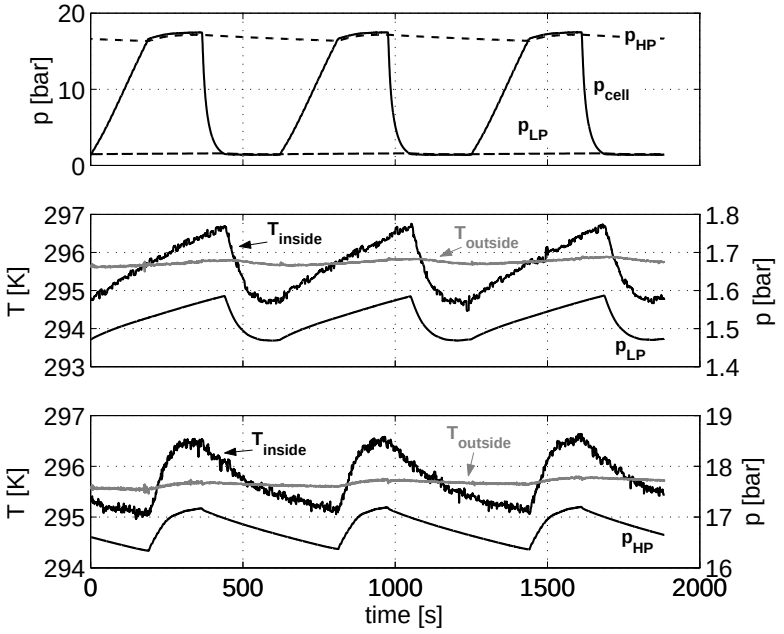

Figure 6.9: Typical measurement result for a compressor with passive sorption-based buffers. (Top) Pressure of the cell p_{cell}, high-pressure buffer p_{HP}, and low-pressure buffer p_{LP} versus time. (Middle) Zoomed view of the pressure in the low-pressure buffer, the temperature on the inside of the buffer and that on the outside (Bottom) Pressure and temperatures in the high-pressure buffer.

phase D. When applying equation (6.1) to these times a pressure variation in the high-pressure buffer of 0.63 bar results and 0.14 bar for the low-pressure buffer. This agrees well with the measurements.

Compressor operation with passive sorption-based buffers

The basic buffers were replaced by the smaller passive sorption-based buffers. The compressor was operated with the same settings and the measurement results are shown in figure 6.9. The restriction was tuned in such a way that flow and pressures were comparable to those of the measurements with basic buffers. As was expected from the argumentation in section 6.1.6, the temperature on the inside of the buffer follows the pressure. The observed pressure variation averaged over 10 cycles was 0.12 bar for the low-pressure buffer and 0.82 bar for the high-pressure buffer, as

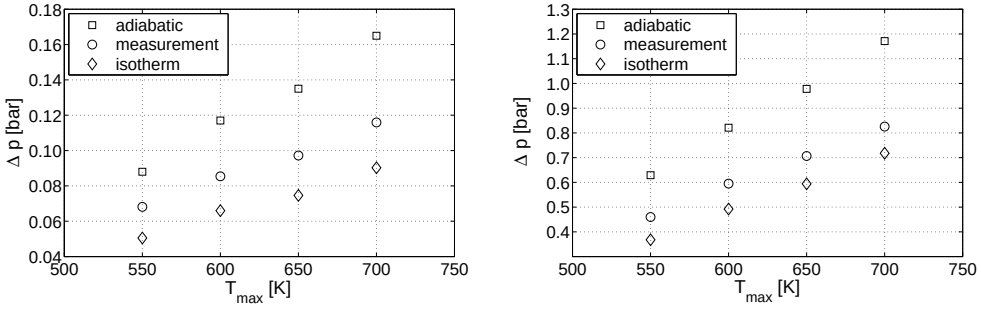

Figure 6.10: (left) Measured pressure variation in the low-pressure buffer compared to the theoretical limits (right) The same for the high-pressure buffer.

expected about the same as in the case of the larger empty buffer volumes. The temperature fluctuation of the buffer wall, measured on the outside of the buffer, was about 0.1 K for both buffers. This is considerably smaller than that of the inside, which was 2.1 K for the low-pressure buffer and 1.6 K for the high-pressure buffer. The temperature gradient over the sorber material will be small as it is governed by the heat of adsorption instead of by a heater as is the case in the compressor cell. The incoming gas, and thus the pressure increase, distributes much faster over the buffer than heat is conducted through the porous sorber material. Therefore, the temperature profile over the sorber bed will be small.

The measured pressure variations in both buffers were compared with the theoretical isothermal and adiabatic limits. To make a comparison for more than one set of control parameters, the compressor was operated with maximum temperatures ranging from 550 K to 700 K in steps of 50 K. The result is shown in figure 6.10. The measured pressures fall between the two theoretical extremes. The pressure variation in the current passive buffer design can be reduced by shifting its operation to the isothermal limit. This can be accomplished by better heat sinking of the sorber material. An option is the application of a conducting matrix structure within the buffer. This can for instance be an aluminum or copper foam [25]. This improves the thermal contact with the buffer wall and also adds heat capacity to the buffer. An alternative is to increase the length-to-diameter ratio which also reduces the thermal path to the wall. A good conducting buffer material can be useful in improving the thermal contact with an external heat sink, e.g. a cooled platform that is kept at a fixed temperature or the heat sink of the compressor cell. Sorber materials with lower void volume fractions or a monolith will have a larger effective thermal conductivity. However, when the adsorption capacity per gram of sorber material is unchanged, the

heat of adsorption is generated in a smaller volume, which counteracts this effect.

Compressor operation with active sorption-based buffers

The passive sorption-based buffer on the low-pressure side was replaced by an active buffer as described in section 6.1.6. The set point of the PID-control algorithm was set to 1.43 bar, which is the lowest pressure in the buffer without PID control. The PID settings were determined according to the closed-loop Ziegler-Nichols method, see e.g. [15, 26]. The restriction was set in such a way that, with the PID control switched off, the flow through it and the pressure swing of the cell were similar to the measurements with basic and passive sorption-based buffers. The compressor was operated with the same set of control parameters as in the previous sections and the results are shown in figure 6.11. During phases A to C, the Peltier element cools the buffer at moderate input powers to compensate for the incoming flow from the restriction. When the pressure in the cell becomes lower than that of the low-pressure buffer, the check valve on the low-pressure side opens and the pressure tends to drop at a fast pace. The control algorithm steadily increases the heating power as the difference with the set point becomes larger. This continues until the maximum allowed voltage over the Peltier element is reached. After some time, the pressure difference reduces and the controller reduces the input power. Finally, the pressure in the buffer becomes equal to the set point again. Another, but smaller, disturbance occurs when the low-pressure check valve closes. The pressure variation averaged over 10 cycles resulted as 57 mbar. This is a factor of two lower than for the passive sorption-based buffers whereas the buffer volume is 5 times smaller.

After the low-pressure check valve opens, the PID-control algorithm gradually increases the heating power as the difference between the pressure of the low-pressure buffer and its set point becomes larger. It takes some time before the heat that is put in by the TE element arrives at the sorber material because of the thermal resistance and the heat capacity of the buffer wall and the aluminum block. It can be predicted from the nature of the compressor that a considerable heat input is needed as soon as the low-pressure check valve opens. The pressure variation of the present low-pressure buffer can be reduced further by heating the buffer at full power as soon as the low-pressure check valve opens. The algorithm was therefore adapted, such that the PID control is used during the majority of time, but just before the low-pressure check valve opens, the PID control is overruled and the Peltier element is set to heating at full power. The PID control is switched on again when the pressure difference between the low-pressure buffer and the set point has passed its maximum. The measurement results with this overruled PID control algorithm are shown in

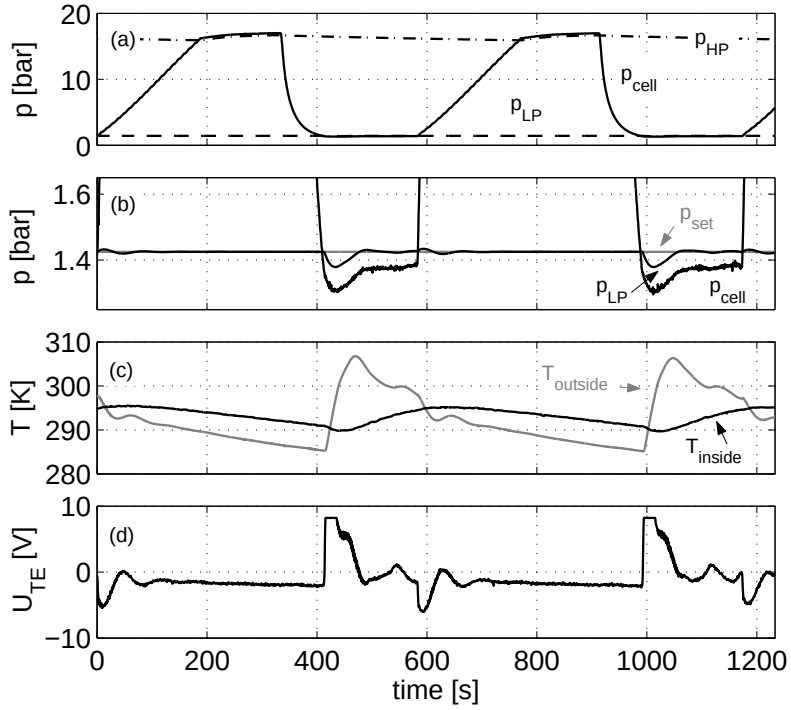

Figure 6.11: Typical behaviour of the active sorption-based buffer with PID control applied to the pressure in the low-pressure buffer. (a) Pressure in the cell (p_{cell}), the high-pressure buffer (p_{HP}), and the low-pressure buffer versus time (p_{LP}). (b) Detailed view of the low-pressure side. (c) Temperature on the inside (T_{inside}) of the low-pressure buffer and on the aluminum $T_{outside}$ (d) Voltage across the Peltier element. A positive voltage implies heating of the buffer whereas a negative voltage means cooling.

figure 6.12. The pressure variation of the low-pressure buffer now reduces to 21 mbar, which is nearly a factor 3 lower than with PID control only. A further reduction in pressure variation can probably be achieved by applying a control system that uses physical information of the system to predict its behaviour and to forecast the required control value.

The input power to the active buffer in the present set-up is considerably higher than the amount calculated in section 6.1.6. This is because the wall thickness of the buffer is several times thicker than assumed in the model and the aluminum block, which is not present in the model, contributes considerably to the total heat capacity. Furthermore, there is a huge temperature gradient over the sorber material

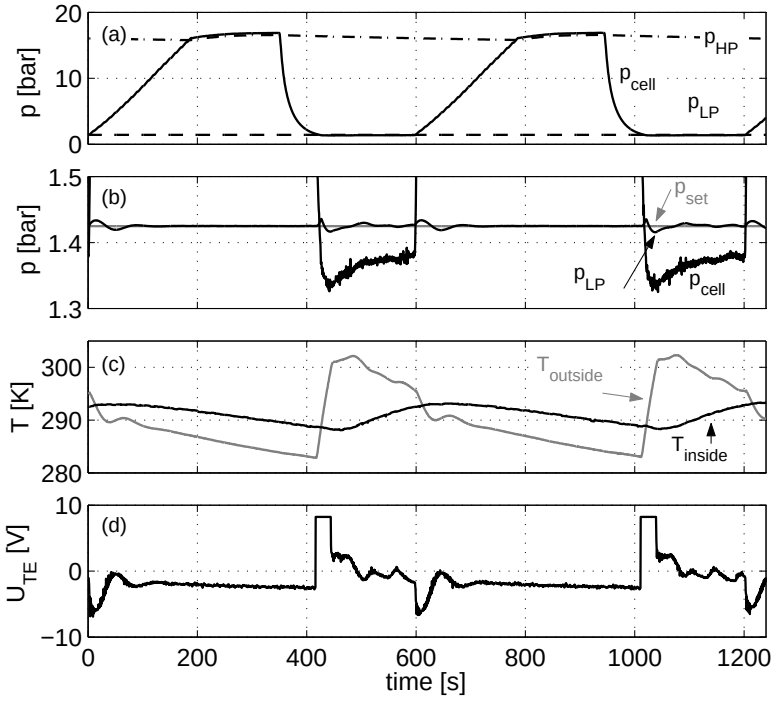

Figure 6.12: Typical behaviour of the active sorption-based buffer with overruled PID control as discussed in the text. (a) Pressure in the cell (p_{cell}), the high-pressure buffer (p_{HP}), and the low-pressure buffer versus time (p_{LP}). (b) Detailed view of the low-pressure side. (c) Temperature on the inside (T_{inside}) of the low-pressure buffer and on the aluminum $T_{outside}$ (d) Voltage across the Peltier element. A positive voltage implies heating of the buffer whereas a negative voltage means cooling.

as the effective thermal conductivity of the charcoal is about two orders of magnitude lower than that of the stainless steel buffer. This is also illustrated by the measured temperature variations. This variation in the centre of the buffer is about 5 K whereas that in the aluminum block is about 20 K. The amount of energy that needs to be extracted to cool the buffer was determined from the measured temperature variations and the heat capacity of the materials. A total energy of 1.2 kJ resulted. The determination of the input power to the TE cooler is somewhat more complicated as only the voltage across the thermo-electric cooler was measured. Therefore, the input power was estimated from the COP of the TE cooler. This efficiency is strongly dependent on the temperature difference between the hot and the cold side. A fixed

cooler COP of 0.5, independent of the temperature difference between the hot and cold side, was assumed. An input power to the TE of 3.3 kJ resulted. This is about a factor 2 higher than the input to the sorption cell of 1.8 kJ. When there would be no temperature gradient, the input power to the Peltier element reduces to 1.3 kJ.

Much more reduction in input power can be achieved by a redesign of the buffer. It is beneficial to reduce the thermal resistance between the equipment that performs the heating and cooling element and the sorber material. This reduces not only the temperature gradient over the buffer, and hence the input power, but will also enable a faster response to changes in the pressure. A reduction in the heat capacity also has these two advantages. An option is to put the heater inside the sorber, similar to the design of the compressor cell. The energy that is dissipated is completely used for desorption of gas, counteracting the pressure decrease. A uniform temperature in the sorber bed is preferable from the shape of the isotherms as was discussed in section 6.1.5. Cooling on the inside of the buffer is more difficult to achieve. However, the low-pressure buffer only requires fast heating whereas the required cooling rates are lower. Application of a good conducting matrix material improves the thermal contact within the sorber and to the buffer wall, at the cost of some additional heat capacity. The energy savings due to the reduction in temperature profile should be larger than the additional energy needed to cool the additional heat capacity. Application of a sorber material with a lower void volume fraction is also attractive. The internal thermal resistance is reduced, whereas the heat capacity remains roughly unaltered. Besides, the buffer can be smaller in size, reducing the distance between the heating and cooling element and the charcoal. To reduce the heat capacity of the container, it is beneficial to use a material with a low $\rho c_p/\sigma_y$-ratio. Aluminum, Inconel, silicon carbide, and some titanium alloys are candidates. Of these materials, aluminum has the highest thermal conductivity, which can further reduce the thermal resistance between the sorber and the cooling element, if situated on the outside of the buffer. The disadvantage of these materials is that for small sizes, the wall thicknesses become extremely small. This, and the nature of the material, may make realisation much more complicated compared to stainless steel. When a stainless steel buffer is used, a good-conducting layer can be coated on the surface to improve the thermal contact. Note that the model calculations, performed with stainless steel, give a total heat input on the order of 10% of the input power to the compressor cell. A completely different approach is to actively heat the buffer and to perform the cooling passively. This saves the input power of cooling. A difficult issue in the design will be to match the rate of cooling to the amount of gas that flows in. Of course, active cooling and passive warm-up is also possible but is less attractive for two reasons. First, a relatively large heating rate is needed to keep the

Buffer type	Volume [cm^3]	Δp [bar]	ΔT_{boiler} [K]
Low-pressure buffer			
basic	300	0.14	1.9
passive sorption-based	50	0.12	1.7
active sorption-based, PID	10	0.057	0.76
active sorption-based, partly overruled PID	10	0.021	0.29
High-pressure buffer			
basic	50	0.63	
passive sorption-based	16	0.82	

Table 6.2: Summary of applied buffer types and resulting pressure variations. The fourth column gives the theoretical values of the temperature variations of the liquid in the boiler if a LH cold stage would be connected to the compressor.

pressure constant upon opening of the low-pressure check valve and will be difficult to achieve. Besides, the COP for cooling will in general be lower than that of heating and from the view point of input power, passive cooling is more attractive.

Conclusions with respect to buffer types

A summary of the applied buffer types and volumes with the resulting pressure variations is given in table 6.2. The measured pressure variations in the low-pressure buffer were also converted to the variation of the temperature of the liquid in the boiler as will be discussed in the next section. Application of passive sorption-based buffers can reduce the buffer sizes considerably compared to basic buffers with comparable magnitudes of the pressure variations. The size of the low-pressure buffer was reduced with a factor 6 and that of the high-pressure buffer with a factor 3. The difference in the volume reduction is caused by the flatter shapes of the isotherms at higher pressures. Alternatively, leaving the buffer volumes unchanged in size and filling them with a sorber would have resulted in smaller pressure variations. Actively heating and cooling of a sorption-based buffer can reduce the pressure variations further at the cost of additional input power. In the experiments, such an active buffer was only applied at the low-pressure side. The aim in these experiments was to reduce both the pressure variations and the buffer size. The latter was reduced to 10 cm^3, which is comparable to the size of the compressor cell and 30 times smaller than the initial volume. The pressure variation was reduced to 21 mbar. Model calculations give, for the current buffer size, an additional input power of about 10% of that of the compressor.

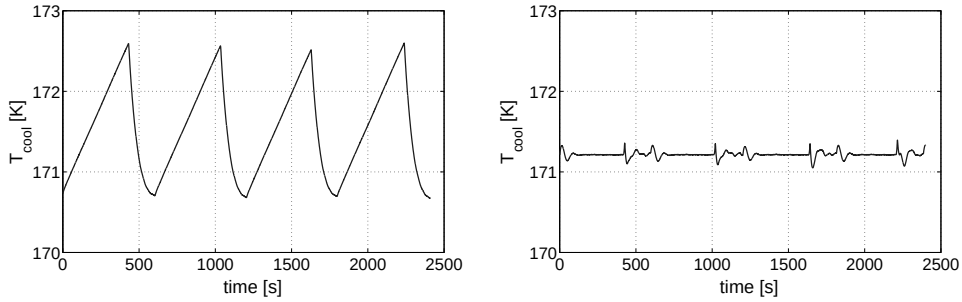

Figure 6.13: Calculated temperature of the liquid in the boiler of a cold stage as derived from the pressure in the low-pressure buffer when a basic buffer of 300 cm^3 is applied (left) and when an active buffer with a volume of 10 cm^3 is used with partly overruled PID control (right).

6.2.2 Implications for the cooler

When the compressor is connected to a LH cold stage, the variation of the pressure in the low-pressure buffer affects the temperature of the liquid in the boiler of the cold stage. The measured pressures from the low-pressure buffer were converted to the temperature of the liquid within a boiler using GasPak [21]. The left-hand side of figure 6.13 shows the temperature variation for the case that basic buffers were applied. The temperature varies between 170.7 K and 172.6 K, a variation of nearly 2 K. The right-hand side of the figure shows the temperature variation in case of an active buffer with partly overruled PID control. The temperature variation has reduced with more than a factor of 6 to 0.29 K whereas the buffer size is reduced with a factor of 30. The last column of table 6.2 gives the theoretical temperature variations for the other buffer types that were applied. A further reduction in the temperature variation can be achieved by a redesign of the active buffer. Some design suggestions were made in the previous section. Apart from methods to reduce the pressure variation in the low-pressure buffer, also common techniques to control a coolers cold-tip temperature can be applied.

Also the cooling power will vary somewhat because of the time-dependent flow through the cold stage and the pressure-dependent enthalpy of cooling. This will result in a variable liquid production rate, which in general is not a problem. Assuming a precool temperature of 235 K and ideal counterflow heat exchangers, the configuration with basic buffers would give an average cooling power of 42 mW at about 172 K if a cold stage with ideal heat exchangers would be connected to the compressor.

6.2.3 Comparison between 1-cell design and conventional design

If the compressor cell from this set-up would be applied in a traditional compressor configuration using 4 cells, the cycle time would increase to 796 s because of the synchronisation. Each cell would then, on average, deliver a flow of 0.39 mg/s to the restriction, assuming that the amount of gas that is pumped by the cell during a cycle does not change. The total flow through the restriction would be 1.56 mg/s, three times that of the single-cell design. To get the same flow out off the single-cell design, 3 cells of the same size should be put in parallel. This saves one cell compared to the traditional lay-out. An alternative is to use a single cell that is three times larger. This is simpler and more reliable compared to using three cells in parallel. When we assume that the chance of failures is determined by the compressor cells, the chance that the configuration with one large cell fails during its lifetime is three times smaller than that of the configuration with 3 parallel cells. One can increase the reliability even more by placing a fourth cell in parallel. Now two cells must fail before the compressor cannot meet its specifications anymore. When the chance that the compressor with 3 parallel cells fails during its lifetime is K, the chance that 1 of the 4 cells fail is $\frac{4}{3}K$, whereas the chance that two cells fail is $\frac{4}{3}K^2$. If K is e.g. 3%, then the failure chance reduces with a factor 25 when an additional cell is placed.

6.2.4 Sensitivity analysis

A sensitivity analysis was performed experimentally with the compressor with basic buffers to investigate the effect of variations in the control parameters on the compressor behaviour. Four control parameters were investigated: f_{BC} and f_{DA} as described in section 6.1.5, the maximum temperature set for the compressor cell and the compressor peak input power. The switching time of the heat switch is also an important parameter, but could not be varied in the current set-up. The setting for each control parameter was varied while the other parameters were kept constant. For each setting, the compressor was operated for at least 18 cycles. Only the last 10 cycles, during which the compressor was in stable operation, were taken into account.

The maximum amount of power that can be obtained from the created pressure difference, or the exergy rate, is [27]

$$\dot{W}_{max} = -\frac{d(U - T_{HS}S)}{dt} + \dot{m}_H(h_H - T_{HS}s_H) - \dot{m}_L(h_L - T_{HS}s_L) \qquad (6.9)$$

with U the internal energy and S the entropy of the gas in the system to which the pressure difference is applied, T_{HS} the heat sink temperature, $\dot{m}$ the mass flow,

h the specific enthalpy and s the specific entropy of the gas. The subscript H refers to conditions of the gas at the high-pressure side, whereas an L refers to the low-pressure side of the compressor. We calculated the average of the maximum available power during a cycle by summation of the averages of the individual terms of equation (6.9). As the compressor is in stable operation, the mean of the first term right to the equal sign is zero. For the calculation we assumed that the high-pressure gas is cooled to the heat sink temperature before it comes available to a system that converts the pressure difference to work or cooling power. For $\dot{m}_H$ the mass flow through mass flow meter B (see figure 6.2) was taken whereas the flow measured by mass flow meter C was taken for $\dot{m}_L$. Note that the position of the mass flow sensors, or in other words the boundary of the system that converts the available pressure difference to work, affects the values that are obtained for the exergy. The sizes of the volumes between the flow sensors and the restriction affect the flow through the sensors even when the volumes of the buffers remain unaltered. This influences the rate of exergy as the pressures in the buffers are not constant during a cycle.

The compressor COP results from

$$\mathrm{COP} = \frac{\overline{\dot{W}_{max}}}{\overline{P_{input}}} = \frac{\int\limits_{cycle} \dot{m}_H(h_H - T_{HS}s_H)dt - \int\limits_{cycle} \dot{m}_L(h_L - T_{HS}s_L)dt}{\int\limits_{cycle} P_{input}dt} \tag{6.10}$$

Only the input power for the heater was taken into account. The power needed to actuate the gas-gap was excluded.

Variation of f_{BC}

The compressor cell was operated with f_{BC} set to values between 0.5 and 3. The other settings were as described in section 6.2.1. Figure 6.14 shows the variation of pressures, mass flows, rate of exergy and compressor COP with f_{BC}. The effective value of f_{BC} is not the same as the factor that was set in the control software. The intermittent heating causes an oscillating flow from the cell to the buffer. The software switches the heater off as soon as the flow drops below $f_{BC} \cdot \dot{m}_{restr}$. This will always be near the minimum of the oscillations. The *average* flow to the high-pressure buffer at this moment will be higher. Besides, when the software detects that heating should be stopped, it takes some time before the compressor cell starts cooling down and the high-pressure check valve closes. We are interested in the factor f_{BC} just before this happens. To take these effects into account, the 'effective' value of f_{BC} was estimated by averaging the flow between the cell and the high-pressure buffer during the last two oscillations and dividing this over the flow through the

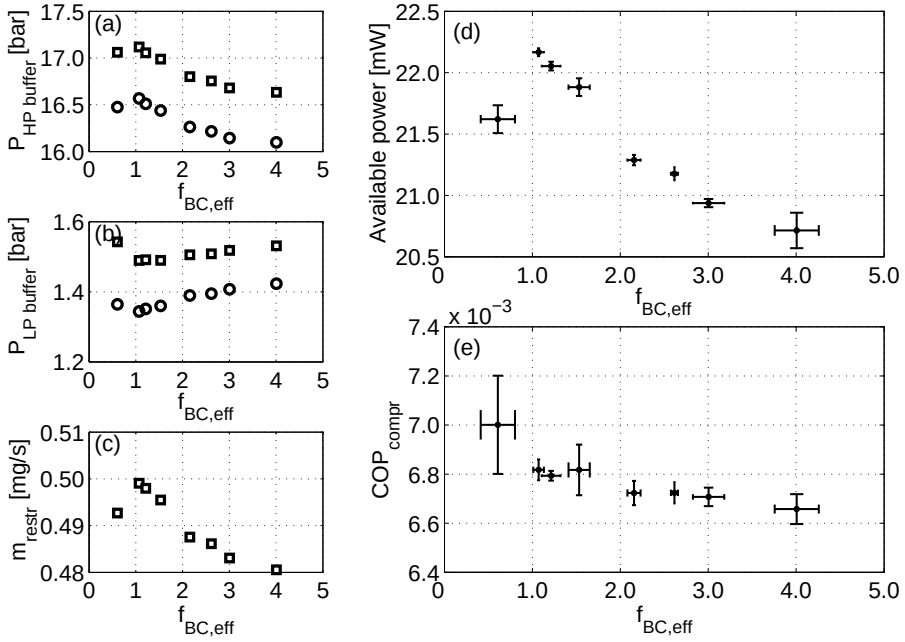

Figure 6.14: Behaviour of sorption compressor cell with variation of f_{BC}. The standard deviations in pressures and mass flows are smaller than 1%. (a) Maximum and minimum observed pressure in the high-pressure buffer. (b) Similar for the low-pressure buffer. (c) Mass flow through the restriction. (d) Available power, averaged over a cycle. (e) Compressor efficiency.

restriction. The values for the individual cycles were averaged. In the figure, the standard deviation was plotted as the error.

When increasing f_{BC}, i.e. switching sooner, both the amount of gas that flows from the cell to the high-pressure buffer during a cycle and the cycle time reduce. The pressure swing of the compressor, i.e. the difference between high pressure and low pressure, depends on the amount of gas the compressor pumps per unit of time. At low values of f_{BC}, the pressure swing increases with increasing f_{BC}, because the cycle time reduces more rapidly than the amount of gas. When f_{BC} is increased further, the amount of gas reduces faster than the cycle time, resulting in a decreasing pressure swing. Note that the change in pressure swing caused by the variations in f_{BC} is relatively small. The difference between the minimum and maximum pressures in the low-pressure buffer decreases with increasing values of f_{BC}. The cycle time goes down, mainly due to the shorter duration of phase B, while the length of phase D remains fairly constant. This results in a reduction in the pressure variation

in the low-pressure buffer (see equation (6.1)), whereas the pressure variation in the high-pressure buffer is about constant.

The mass flow through the restriction depends on the pressure difference between the high- and low-pressure buffers. During a cycle, the fluctuations in mass flow, high pressure and low pressure are relatively small. In the regime the compressor is operating, xenon is a near-ideal gas. Then, $|\Delta h| << |T\Delta s|$ and the available power roughly equals $-\dot{m}T_{HS}\Delta s$. A larger pressure swing results in both a larger flow and a larger entropy difference between the gas that flows out off and into the compressor. So, the rate of exergy increases as the pressure difference increases. Note that the effect of f_{BC} on the magnitude of the available power is small. From figure 6.14e it turns out that the compressor COP slightly decreases for increasing values of f_{BC}. Apparently, the input power decreases slower than the exergy. The maximum pressure difference is achieved for f_{BC} is equal to or slightly larger than 1.

Variation of f_{DA}

The compressor is switched from the cooling mode to the heating mode when the flow from the low-pressure buffer to the cell falls below $f_{DA} \cdot \dot{m}_{restr}$. The effect of a change in f_{DA} on the compressor operation was investigated. The results are shown in figure 6.15. When the software switches the compressor to the heating mode, it takes some time before the pressure in the cell builds up and the low-pressure check valve closes. As we are interested in the flow just before the check valve closes and not in f_{DA} at the moment the software performs the switch, a correction on f_{DA} is needed. As there are no oscillations in the relevant flows, the correction factor is much smaller than for f_{BC}. At the moment the check valve closes, there is a distinct discontinuity in the derivative of the flow. The effective value of f_{DA} was calculated by dividing the mass flow to the cell by the mass flow through the restriction just before this discontinuity. The standard deviations of the thus obtained effective values are smaller than 3%.

Similar to the study of changes in f_{BC}, an increase in f_{DA} reduces both the cycle time and the amount of gas that is pumped by the compressor during a cycle. For low values of f_{DA}, the cycle time reduces faster than the amount of gas that is pumped. For larger values, the amount of gas reduces faster as the length of phase D becomes small compared to the lengths of the other phases. The latter hardly change with f_{DA}. This also explains why the pressure variation in the low-pressure buffer is barely affected by a change in f_{DA}, whereas the variation in the high-pressure buffer changes considerably.

The total amount of exergy (in Joules) that is produced during a cycle decreases

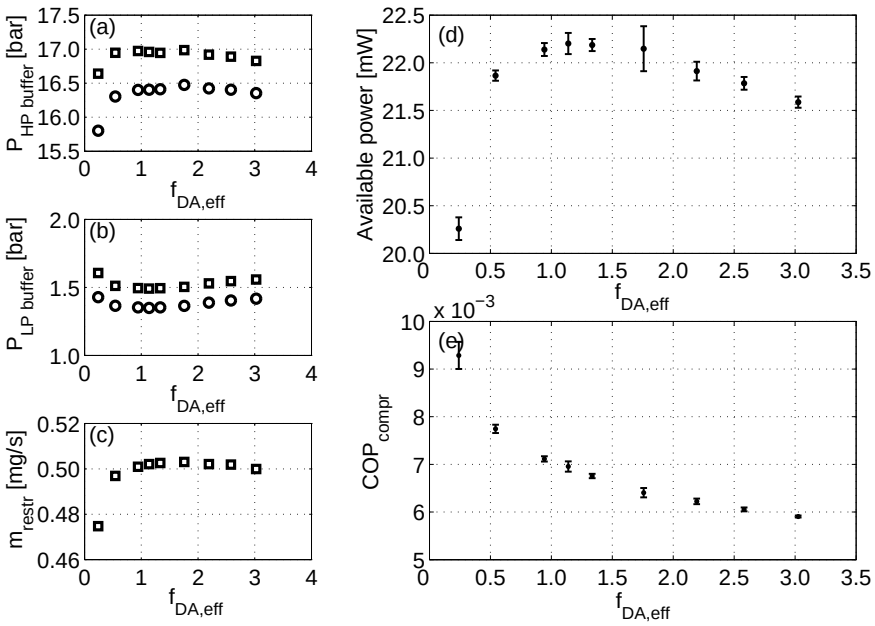

Figure 6.15: Behaviour of sorption compressor cell with variation of f_{DA}. The standard deviation is smaller than 1% for all pressures and mass flows. (a) Maximum and minimum observed pressure in the high-pressure buffer. (b) Similar for the low-pressure buffer. (c) Mass flow through the restriction. (d) Maximum available power, averaged over a cycle. (e) Compressor efficiency.

for increasing values of f_{DA}: the *average* rate of exergy hardly changes (see figure 6.15d) whereas the cycle time reduces dramatically. The total amount of heat input for each cycle is roughly constant as f_{BC} is fixed. Therefore, the compressor COP reduces as f_{DA} increases as is confirmed by figure 6.15e.

Variation of input power

The compressor peak input power was changed by varying the voltage over the thermocouple in the heating mode. The control algorithm was not changed. The results are shown in figure 6.16. For the lowest input powers that were applied, the compressor cell does not reach the set maximum temperature and an increase in heating power results in an increase in the highest temperature the compressor cell reaches. This has a positive effect on the amount of gas that comes off the sorber.

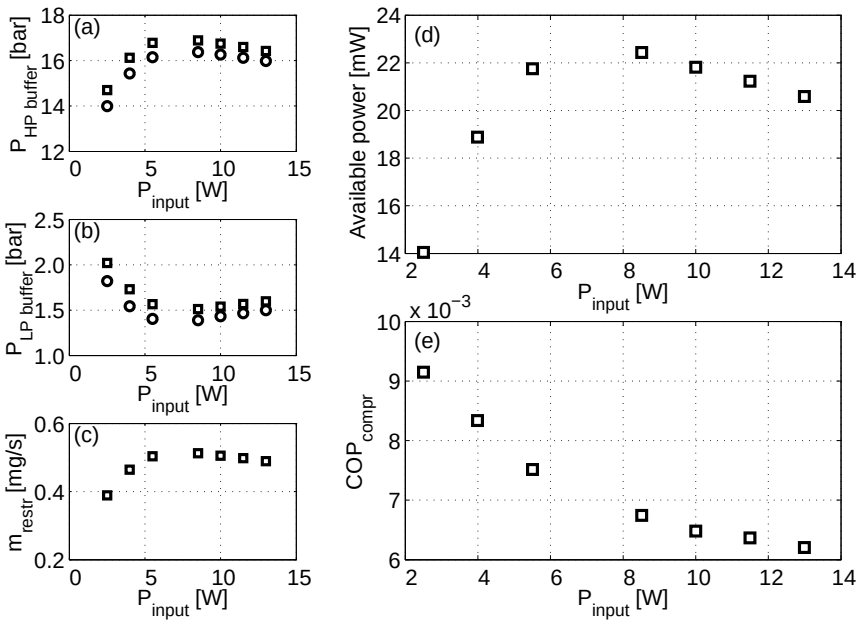

Figure 6.16: Effect of variation in the peak heater input power on: (a) Pressure in high-pressure buffer. (b) Pressure in the low-pressure buffer. (c) Mass flow through the restriction. (d) Maximum available power, averaged over a cycle. (e) compressor COP. The standard deviations are smaller than 1% for all pressures and mass flows.

On the other hand, also the temperature gradient over the sorber material becomes larger. As $\partial^2 x_s/\partial T^2$ is positive, this has a negative effect on the total amount of gas that is desorbed. The combined effect is that the amount of gas that is pumped in a single cycle reduces slightly for increasing input powers. A larger input power also reduces the length of the heating phases. For low input powers, the heating phases are dominant in the cycle time, so the total cycle time reduces significantly when the heating power is increased. As the cycle time reduces faster than the total amount of gas that is pumped during a cycle, the pressure swing increases.

For input powers of 5.5 W and above, the compressor cell reaches the set maximum temperature of 700 K and the control algorithm reduces the time-averaged input power during the heating phase. It turns out that less gas is pumped from the cell to the buffer while at the same time the cycle time goes down. The reduction in the cycle time is comparable to the reduction in the amount of gas that is pumped. The overall effect is a moderate reduction of the pressure swing. To achieve a high

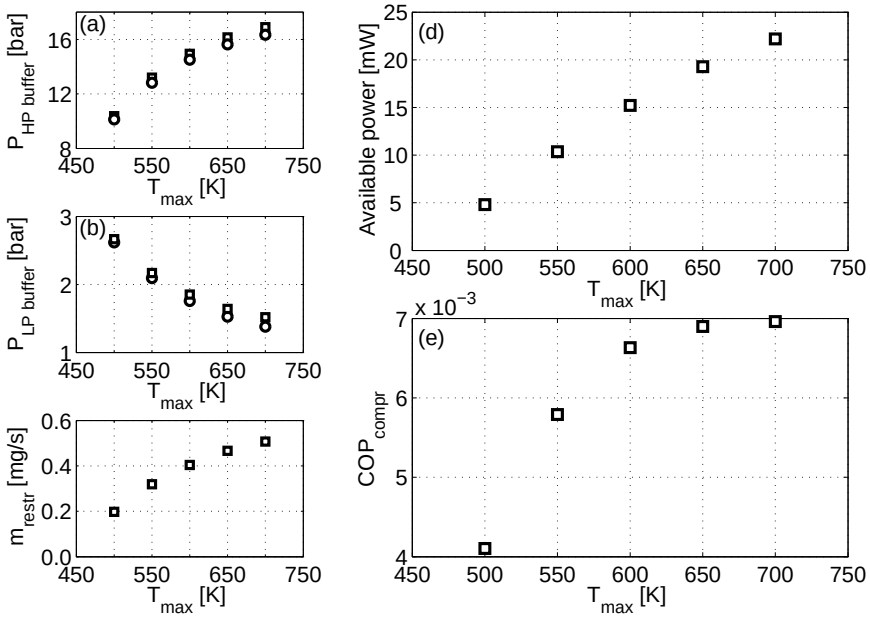

Figure 6.17: Effect of variation on the set maximum temperature on: (a) Pressure in high-pressure buffer. (b) Pressure in the low-pressure buffer. (c) Mass flow through the restriction. (d) Maximum available power, averaged over a cycle. (e) compressor COP. The standard deviations are smaller than 1% for all pressures and mass flows.

compressor COP, a low input power is beneficial because of the lower temperature profile.

Variation of set maximum temperature

The set maximum temperature was changed from 500 K to 700 K in steps of 50 K. The results are shown in figure 6.17. A higher maximum temperature implies a larger heat input. As the heating power is not changed, the heating phases take longer, resulting in longer cycle times. A higher cell temperature also means that more gas comes off the sorber. As a result, the amount of mass that is cycled per unit of time increases when the maximum temperature is increased. The pressure swing increases less than linear with the set maximum temperature as $\partial^2 x_s/\partial T^2$ is positive. So, the increase in amount of desorption goes down, whereas the cycle time increases about linearly. The total heat input increases somewhat faster than the gain in available

power. From the figure, it turns out that the optimum compressor COP is obtained for a set maximum temperature of about 700 K.

Conclusions of sensitivity analysis

For the given compressor design and control algorithm, the maximum pressure swing is obtained for effective values of f_{BC} and f_{DA} slightly above 1, a peak input power of about 7 W and a set maximum temperature above 700 K. The effect of a change in the set maximum heater temperature and the input power on the achieved pressure swing is much larger than that of a change in f_{BC} or f_{DA}. The optimum in the maximum available power roughly coincides with the maximum in the pressure swing. An optimum compressor COP is achieved for low values of f_{BC} and f_{DA}, a low input power and a set maximum temperature of about 700 K.

6.3 Conclusions

An alternative sorption compressor design, consisting of a single compressor cell, two check valves and two buffer volumes, was investigated. Such a design is easier to operate than a compressor consisting of multiple cells that operate out of phase. It is less complex and increases the reliability of the cooler. Furthermore, more mass flow can be delivered by a single cell as no synchronisation between the phases is needed. The principle was tested using a set-up with a sorption compressor of about 8 cm^3 that was filled with Maxsorb activated carbon. Xenon was used as the working gas. A continuous flow of 0.52 mg/s was established with a pressure swing of 1.39 to 17.0 bar. If the compressor would be connected to a JT expansion stage, a cooling power of about 42 mW at 172 K is expected.

Several types of buffers were applied. The simplest type was an empty volume. The disadvantage of these buffers is that the required volumes are much larger than that of the compressor. Filling the buffers with a sorber material increases its storage capacity. In this way, the pressure variations or the sizes of the buffers can be reduced. It was demonstrated experimentally that a 6 times smaller low-pressure buffer and a 3 times smaller high-pressure buffer that were filled with Maxsorb gave similar pressure variations at a comparable pressure swing of the cell and flow through the restriction. A further reduction in both size and pressure variation was achieved by actively controlling the pressure in the low-pressure buffer by heating and cooling of the sorber material. The disadvantage is the additional input power that is needed. A non-optimised buffer volume of 10 cm^3, 30 times smaller than the basic buffer, that was cooled with a thermo-electric cooler positioned on the outside already reduced

the pressure variation to 21 mbar, giving a theoretical variation of the temperature of the liquid in the boiler of 0.29 K. Model calculations for this buffer size give an additional input power of about 10% of that of the compressor. Optimisation of both the thermal design of the buffer and the control algorithm can further reduce the pressure variation and size.

The effect of the control parameters f_{BC}, f_{DA}, the maximum heater temperature, and the peak input power on the compressor operation were experimentally investigated. From the sensitivity analysis, it appears that the effect of the set maximum heater temperature and the input power on the achieved pressure swing is much larger than that of a change in f_{BC} or f_{DA}. An optimum compressor COP is achieved for low values of f_{BC} and f_{DA}, a low input power and a set maximum temperature of about 700 K. The switching time of the heat switch can substantially impact the timing and thus the COP. This effect could not be determined with the current set-up.

References

[1] Marlow Industries, Inc. 10451 Vista Park Road, Dallas, Texas, USA. http://www.marlow.com.

[2] The Kansai Coke & Chemicals Co. Ltd., 1-1 Oh-Hama, Amagasaki, Japan 660.

[3] T. Otowa, R. Tanibata, and M. Itoh. Production and adsorption characteristics of MAXSORB: high-surface-area active carbon. *Gas separation & purification*, 7(3):241–245, 1993.

[4] Omega Engineering, Inc., One Omega Drive, Stamford, Connecticut 06907-0047, USA, http://www.omega.com.

[5] J. F. Burger, H. J. M. ter Brake, H. J. Holland, J. W. Berenschot, M. Elwenspoek, and H. Rogalla. A 170 K microcooler with a thermal sorption compressor and a micromachined cold stage. *submitted to Cryogenics*, 2005.

[6] Kulite Semiconductor Products, Inc., One Willow Tree Road, Leonia, NJ 07605, USA, http://www.kulite.com.

[7] Heraeus Sensor Technology GmbH, Reinhard-Heraeus-Ring 23, D-63801, Kleinostheim, Germany, http://heraeus-sensor-technology.de.

[8] VICI AG (Valco International), Parkstrasse 2, CH-6214 Schenkon, Switzerland, http://www.valco.com.

[9] R. J. Corruccini. Gaseous heat conduction at low pressures and temperatures. *Vacuum*, VII & VIII:19–29, 1957-1958.

[10] A. Roth. *Vacuum technology*. Elsevier Science, Amsterdam, 1990.

[11] J. F. Burger, H. J. Holland, H. van Egmond, M. Elwenspoek, H. J. M. ter Brake, and

H. Rogalla. Fast gas-gap heat switch for a microcoolers. In *Cryocoolers 10*, pages 565–574, New York, 1999. Kluwer Academic/Plenum Publishers.

[12] M. Prina, J. G. Kulleck, and R. C. Bowman Jr. Assessment of Zr-V-Fe getter alloy for gas-gap heat switches. *Journal of Alloys and Compounds*, 330-332:886–891, 2002.

[13] MKS Instruments, 90 Industrial Way, Wilmington, Massachusetts 01887, USA, http://www.mksinst.com.

[14] J. F. Burger, M. C. van der Wekken, E. Berenschot, H. J. Holland, H. J. M. ter Brake, and H. Rogalla. High pressure check valve for application in a miniature cryogenic sorption cooler. In *Twelfth IEEE International Conference on Micro Electro Mechanical Systems*, pages 183–188, 1999.

[15] National Instruments Corporation, 11500 N MoPac Expwy, Austin, TX 78759-3504, USA, http://www.ni.com.

[16] Druck Ltd., Fir Tree Lane, Groby, Leicester, LE6 0FH, England, http://www.druck.com.

[17] Sensortechnics GmbH, Boschstr. 10, 82178 Puchheim, Germany, http://www.sensortechnics.com.

[18] Bronkhorst High-Tech B.V., Nijverheidsstraat 1A, 7261 AK, Ruurlo, The Netherlands, http://www.bronkhorst.nl.

[19] Swagelok Company, 29500 Solon Road, Solon, OH 44139, USA, http://www.swagelok.com.

[20] A. Bejan. *Heat transfer*. Wiley, New York, 1993.

[21] Cryodata Inc., P.O. box 558, Niwot, CO 80544, USA, http://www.cryodata.com.

[22] G. Berndt. *Taschenbuch Maschinenbau*. Verlag Technik, Berlin, 1965.

[23] Melcor Corporation, 1040 Spruce Street, Trenton, NJ 08648, USA, http://www.melcor.com.

[24] HS Marston Aerospace Limited, Wobaston Road, Fordhouses, Wolverhampton, WV10 6QJ, England, http://www.hsmarston.co.uk.

[25] ERG, Materials and Aerospace Corp., 900 Stanford Avenue, Oakland, CA 94608, USA, http://www.ergaerospace.com.

[26] N. K. Sinha. *Control systems*. John Wiley & Sons, 1994.

[27] A. Bejan. *Advanced Engineering Thermodynamics*. Wiley Interscience, 1988.

Chapter 7

Two-stage single-cell compressor unit

7.1 Design of a cooler using a two-stage compressor unit

This chapter describes the design and measurement results of a two-stage compressor based on the single-cell concept as introduced in chapter 5.

Selection of working gas Similar to the single-stage single-cell compressor, xenon could be used as the working gas. The compression from about 1 to 17 bar would then be performed with a higher compressor efficiency. As shown in section 5.2.1, also much higher pressures can be achieved when two-stage compression is applied at the cost of some reduction in the compressor COP. Compression of the gas to a somewhat higher pressure has, in the case of xenon, the advantage that the required precool temperature to liquefy the high-pressure gas increases. The thermo-electric precooler can operate with a higher efficiency at the cost of a slightly lower compressor COP. The optimum settings can be determined by an optimisation as performed in chapter 5.

Cryogenic temperatures can, in principle, be reached when krypton, argon or nitrogen is used as the working gas, see table 1.1. Helium, hydrogen, and neon even give lower cold stage temperatures but have a negligible adsorption on carbon at room temperature. Nitrogen was selected as the working gas as it can reach the lowest temperature and still has some adsorption on carbon at room temperature. Besides, nitrogen is convenient to work with and cheap.

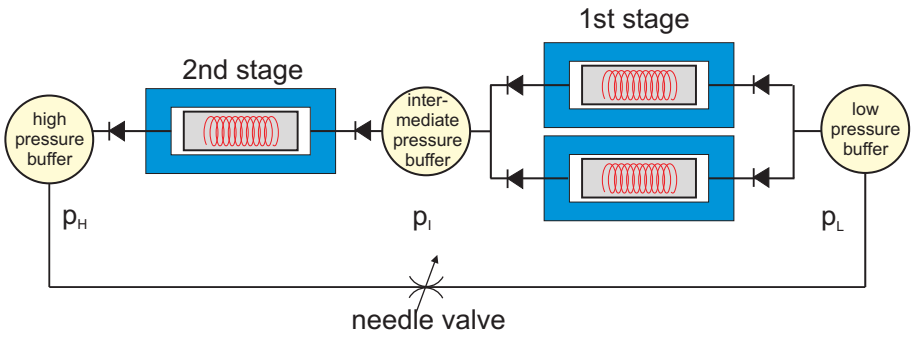

Figure 7.1: Schematic lay-out of the two-stage single-cell set-up with two parallel compressor cells for the first stage and a single compressor cell for the second stage.

Compressor unit At room temperature and low pressures, the adsorbed amount of nitrogen gas on carbon is small. Consequently, not much gas can be desorbed and the pressure swing that can be realised starting from room temperature will be small. The adsorbed amount of gas at room temperature increases when a higher low pressure is selected, at the cost of a higher cold stage temperature. To demonstrate the two-stage compressor, a compressor low pressure of 10 bar was, somewhat arbitrary, selected. The room temperature isotherm increases rapidly with pressure (see figure 5.5), so the amount of gas that is adsorbed at the heat sink temperature in the second stage will be considerably larger than that of the first stage. To increase the flow through the restriction that can be realised, two parallel compressor cells were used for the first stage. This is shown schematically in figure 7.1.

The three compressor cells had the same size and were identical to the compressor cell that was described in section 6.1.2. The void volumes of the cells, including the volume between the check valves and the sorber bed, was measured by pressurising them with helium at room temperature. The volumes were comparable for the three cells and varied between 8.0 cm^3 and 8.2 cm^3.

The compressor cells shared a single heat sink. This was a large aluminum block that was kept at 20 °C by means of a Peltier element with forced air-cooled cooling fins mounted on top. The gas-gap heat switch was realised in the same way as for the single-cell compressor (see section 6.1.3). The gas-gap high pressure was set to 50 mbar whereas a low pressure of $5 \cdot 10^{-4}$ mbar was taken, similar as was done for the single-stage compressor. The three cells also shared the connection to the gas-gap high-pressure and low-pressure 'reservoir'. This results in losses in two ways. If one cell is heating up, while the gas-gap pressure of another cell is switched from the high pressure to the low pressure, a considerable amount of gas is dumped to

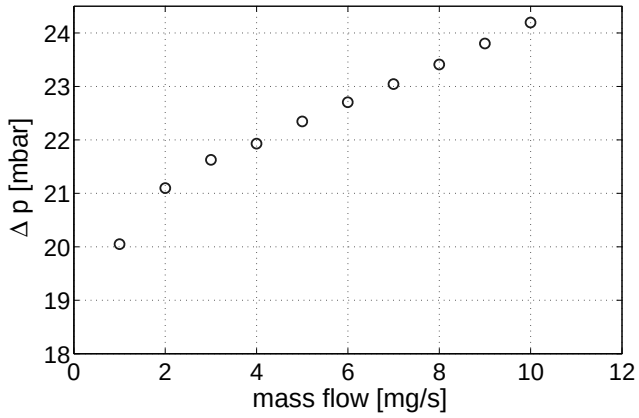

Figure 7.2: Mass flow dependent pressure drop over the Swagelok 6L-CW4S4 check valve for typical flows in the sorption compressor set-up for nitrogen gas with an absolute pressure around 1.3 bar.

the low-pressure reservoir, which is a vacuum pump. This results in a temporarily higher pressure in the gas-gap and hence a better thermal contact for all cells that are connected to the low-pressure reservoir at that moment. Upon switching the valves, the measured pressure in the gap increases to more than 1 mbar resulting in a thermal resistance smaller than about 3 K/W [1, 2]. Within about 3 seconds, the pressure drops to $3 \cdot 10^{-2}$ mbar, increasing the thermal resistance to about 70 K/W. After about 80 seconds, the original gas-gap pressure is restored with an estimated thermal resistance of $4 \cdot 10^{3}$ K/W. So, although the effect on the thermal resistance is considerable, the period with a low thermal resistance of 3 K/W is limited to a very short period. Nevertheless, a split gas-gap heat switch would prevent this loss. In cooling mode, a similar but reverse process occurs. However, the pressure change in the high-pressure reservoir is less dramatic, about 13 mbar, and the effect on the thermal resistance is small as the gas in the gas-gap is close to the viscous regime. At 37 mbar, the lowest value of the high pressure in the gas-gap, the thermal resistance increases to 0.46 K/W compared to 0.45 K/W at the initial pressure of 50 mbar.

Check valves The Swagelok 6L-CW4S4 check valves [3], that were used in the single-stage set-up, were also applied to the two-stage design. The pressure drop over the valve and the leak flow were also tested with nitrogen gas using the set-up from figure 6.3. The pressure drop for mass flows up to 10 mg/s was measured at a low pressure of about 1.3 bar. The result is shown in figure 7.2. Again, the

pressure drop is negligible compared to the pressure swing of the compressor cell. The determination of the cracking pressure is described in section 6.1.4 and resulted as 12 mbar. The check valves also appear to close very well with nitrogen as the working gas. The leak flow, if any, is smaller than the noise level of the sensor of 0.02 μg/s. The total leak through the valve upon closure at low pressure was 0.1 mg. This is considerably lower than the amount of gas that is pumped during a cycle, which is on the order of tens of milligrams.

Buffer volumes The buffer volumes for the two-stage set-up were selected from the available set of buffers used in chapter 6. For the low-pressure buffer, the empty volume of 300 cm^3 was taken. The 50 cm^3 that was filled with activated carbon was used as the intermediate-pressure buffer. For the high-pressure buffer, a thick-walled tube with an internal volume of 25 cm^3 was taken.

Control algorithm The same control algorithm as applied in the previous chapter was used, see section 6.1.5. In this algorithm, the compressor is switched from the heating to the cooling mode when the flow out off the compressor falls below $f \cdot \dot{m}_{restr}$ with f a constant and $\dot{m}_{restr}$ the flow through the restriction. In a similar way, the end of the cooling phase was determined. The reference to $\dot{m}_{restr}$ is not correct in case two compressor cells are operated in parallel. In case of identical cells, each cell provides half the flow of that compression stage. For the first stage, the flow to and from each individual compresor cell was therefore compared to $\frac{1}{2}\dot{m}_{restr}$.

When a cell is supplying gas, the flow out off the cell drops to nearly zero when the heater is switched from the heating mode to the sensing mode. In some cases, the phase during which gas is supplied by the cell would be equal to only one heating interval. Therefore, an additional requirement compared to the algorithm applied to the set-up from chapter 6 was that the flow out off the cell should be lower than $f \cdot \dot{m}_{restr}$ for more than 5 seconds before the compressor is switched from the heating mode to the cooling mode. This eliminates the problem.

Equipment The used equipment was for a large part the same as for the single-cell compressor set-up and was described in section 6.1. Here, only the additional equipment is discussed. The pressures in and the mass flows to and from all three compressor cells were measured with Kulite low-void volume pressure sensors [4] and Bronkhorst EL-FLOW type mass flow meters [5], respectively. The pressures in the low-pressure buffer and the high-pressure buffer were measured with Druck PTX1400 sensors [6], whereas an Econtronic pressure sensor [7] was used to monitor

the pressure in the intermediate-pressure buffer. The temperatures on the outsides of the buffers were measured with Heraeus PT1000-sensors [8]. Only the temperature on the inside of the intermediate-pressure buffer was measured. This was done with an Omega E-type thermocouple [9] that was read-out with a Cryocon temperature controller that applied 'cold junction compensation' [10].

7.2 Results and discussion

7.2.1 System operation

To experimentally determine the effect of two-stage compression on the compressor efficiency, the compressor was operated with a fixed low pressure of 10 bar and varying high pressures. The compressor was also operated in single-stage mode for reference purposes. As an illustration of the operation of a two-stage compressor, this section discusses the operation of a two-stage compressor operating between 10 bar and 76 bar. The efficiency is discussed in the next section.

The two-stage compressor was operated for 29 cycles in stable operation with peak input powers of about 7 W. Having the same power-supply voltage, the actual input powers to the three cells differ up to 15% because of different lengths of the thermocouples in each of the cells and on top of that different thermocouple resistances per unit length. The compressor maximum temperature was set to 700 K. The factors f in the control algorithm, as discussed on the previous page, were set to 1. The flow restriction and the filling pressure were chosen at such values that the compressor low pressure was 10 bar and the compressor high pressure was 76 bar. The behaviour of pressures, mass flows, and temperatures of the thermocouples in the compressor cells with time are shown in figure 7.3.

The pressure in the low-pressure buffer varied between 9.99 bar and 10.1 bar whereas that of the high-pressure buffer varied between 75.0 bar and 76.1 bar. The pressure in the intermediate-pressure buffer sets itself in such a way that, on average, the mass flow to the buffer coming from the compressor cells in the first stage equals the mass flow to the second compression stage. The average pressure in this buffer resulted as 30.7 bar. The pressure swing in the second compression stage, consisting of only a single compressor cell, is considerably higher than that of the first stage, that had two compressor cells. The cause is the shape of the isotherms. At the low pressure, considerably less gas is adsorbed than at the intermediate pressure, as can be seen in figure 5.5. The average mass flow through the restriction equals 0.079 mg/s with a standard deviation of 2.4%. The average input powers to the two compressor cells in the first compression stage were 4.8 W and 4.9 W, respectively, whereas that

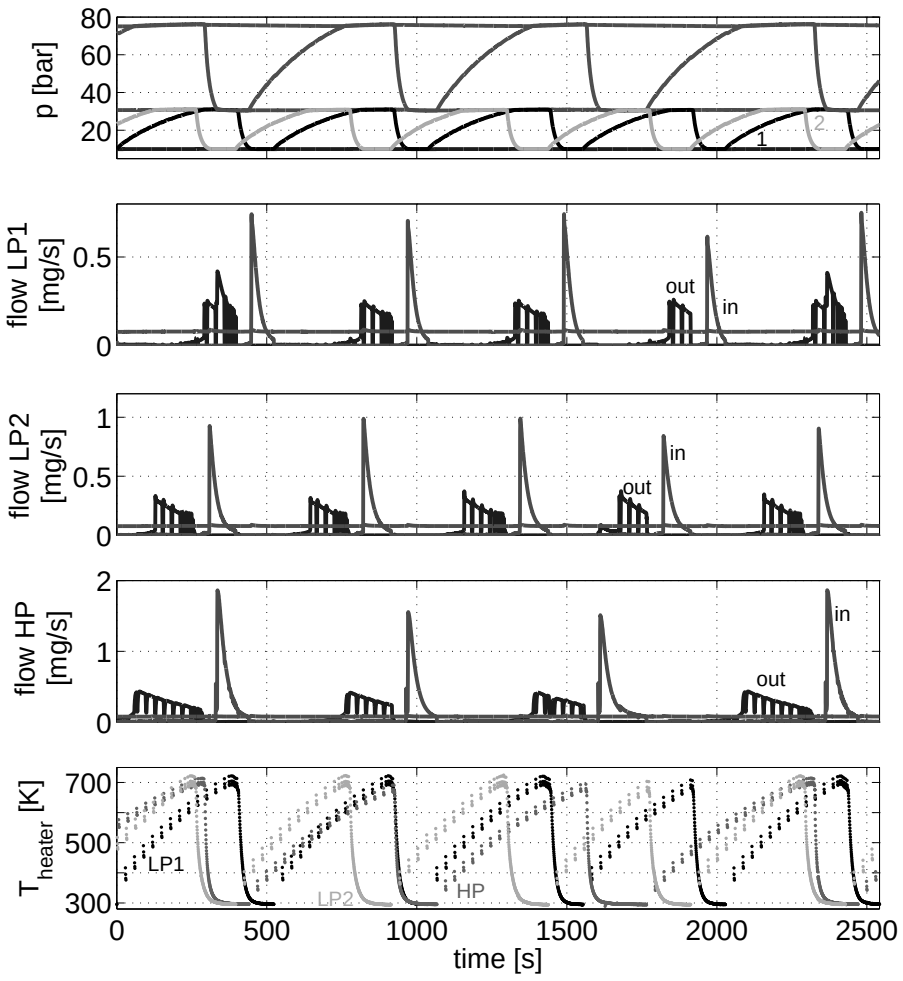

Figure 7.3: Pressures, mass flows, and temperatures of the thermocouples in the cells with time for a two-stage compressor with two parallel cells in the first stage (LP1 and LP2) and a single cell in the second stage. The irregularities in the curves of temperature and out flow are caused by switching the thermocouples between the sensing and heating modes.

to the second-stage compressor was 4.0 W.

The cells were controlled independent of each other. A consequence of the applied control algorithm then is that the cycle times and the magnitude of the flows vary over the cycles. As an example, the period the gas flows out off the second-stage compressor is in the fourth cycle that is shown in figure 7.3 longer than in the second and third cycle. Relative to the previous cycles, more gas is delivered to the intermediate-pressure buffer as low-pressure cell 2 supplies two times gas compared to one time in the other cycles. Hence, more gas is adsorbed by the second-stage compressor. As a consequence, more gas can be delivered to the high-pressure buffer before the outgoing flow becomes lower than the flow through the restriction. The average cycle times of the two compressors in the first compression stage were nearly equal, 502 s and 504 s, and both had a standard deviation of 22 s. The average cycle time of the second-stage compressor was 675 s with a standard deviation of 34 s.

7.2.2 Compressor efficiency

The improvement in compressor efficiency was determined by operating the compressor between 10 bar and 30 bar with different compressor configurations: single-stage compression with one cell and with two parallel cells, two-stage compression with one cell in the first stage and one cell in the second stage, and two-stage compression with two parallel cells in the first stage and a single cell in the second compression stage. This latter configuration was also operated with higher values of the high pressure to investigate the influence on the compressor efficiency. The compressor efficiencies were determined by applying equation (6.9) and neglecting the first term to the right-hand side of the equal sign. Strictly spoken, this is only allowed for stationary or periodic systems. As the fluctuations in pressures and mass flows are small, the errors will be small. The results are shown in figure 7.4.

At a high pressure of 30 bar, the efficiency of the two-stage designs is considerably higher than those of the single-stage designs. The efficiency of the single-stage designs is about $0.9 \cdot 10^{-3}$. The efficiency is somewhat higher when two parallel cells are used instead of one. Perfectly identical cells would have resulted in the same efficiencies. The cell that is included for the measurement with two parallel cells provides more flow than the other cell at comparable input powers. It appears that the cell that is used in both experiments has a larger heat loss to the environment. Furthermore, the relative error in the measured mass flows in case a single compressor cell is used, is about 10% since in that case the flow is in the lower operating range of the sensor [5]. This can also partly contribute to the observed difference in efficiencies.

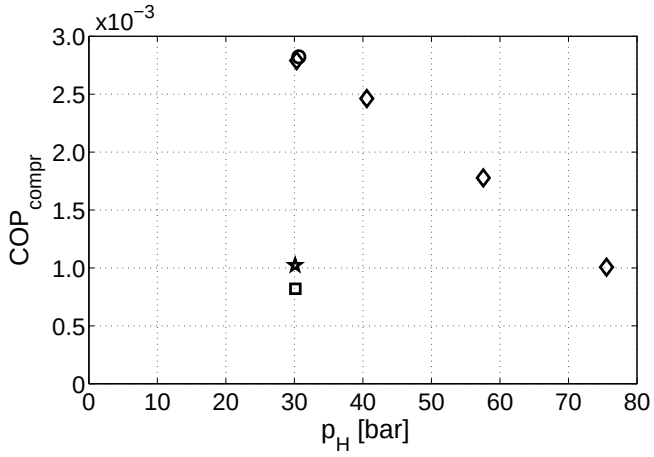

Figure 7.4: Compressor efficiency for various compressor configurations. Diamonds: two-stage compression with two parallel cells in the first stage and a single cell in the second stage, Circle: two-stage compression with a single cell in both compression stages, Square: single-stage compression with a single compressor cell, Star: single-stage compression with two parallel cells.

When two-stage compression is applied, the efficiency increases to $2.8 \cdot 10^{-3}$, an increase with about a factor 3 compared to the single-stage compressor. The efficiency of the design with two parallel cells in the first compression stage roughly coincides with that of a single cell in the first stage. In case of two parallel cells in the first stage, the intermediate pressure is 20.5 bar whereas that pressure is 17.6 bar in case one cell is applied at that stage. A higher intermediate pressure results in a less efficient first-stage compressor and in a more efficient second-stage compressor. For the current design of the compressor cells, working gas, and operating conditions, comparable overall efficiencies result.

The optimised compressor efficiencies based on calculations as discussed in section 5.2.1 for a two-stage compressor with Maxsorb as the sorber material and nitrogen as the working gas is shown in figure 7.5. The low-pressure was set to 10 bar, the same as in the measurements, and the heat sink temperature was set to 293 K. At 30 bar, the absolute value of the measured efficiency is about a factor of 4 lower than the optimised value determined by the model. This difference is caused by the fact that the compressor cells and their operating parameters which were applied in the experiment were not optimised for efficiency and this can explain the discrepancy with the model. The compressor cells that were used in the set-up have much thicker walls than assumed by the model. Besides, the model neglects the

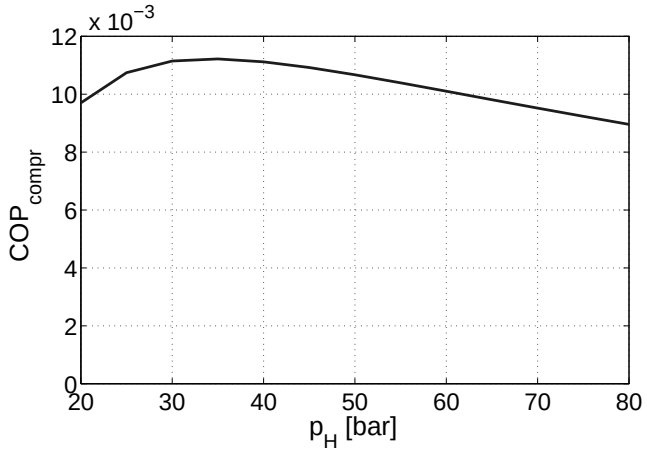

Figure 7.5: Theoretically optimised compressor efficiencies for a two-stage compressor with Maxsorb as the sorber material and nitrogen as the working gas. A low pressure of 10 bar was taken and a heat sink temperature of 293 K was assumed.

end caps. This results for the model in a heat capacity of the sorber and container of 1.9 J/K per gram of sorber material whereas that for the cells from the experimental set-up is 4.0 J/K per gram of sorber material. Besides, the model optimises the value of the intermediate pressure for each value of the high pressure. This results in a COP difference of about 10% at a high pressure of 30 bar. Another aspect is the void volume. The compressor cells that were used have a relatively large external void volume whereas the model only takes into account the intrinsic void volume of the sorber material. At a high pressure of 30 bar, the effect on the efficiency is about 20%. Heat losses from the sorber container to the heat sink are ignored by the model but will be present in the cells that were used. On top of that, the model optimises the temperature to which the cells are heated whereas in the measurements the compressor set maximum temperature was fixed at 700 K. It is quite well probable that the combination of the latter two gives an additional effect of 40%, yielding an overall effect by a factor of 4.

When the high pressure is increased, the compressor efficiency reduces. However, the COP in figure 7.5 reduces less rapidly with increasing pressure than in the measurements because each point in that figure represents an optimised configuration. An important difference is in the set maximum temperature. In the experiments, this temperature was kept fixed for all measurements whereas it is optimised for each pressure in the calculated COP values presented in figure 7.5. Heating the cell to a higher temperature can partly compensate a loss in Δx_{net} due

to the larger pressure difference. Furthermore, the intermediate pressure, or in other words the ratio $\Delta x_{net2}/\Delta x_{net1}$, was optimised in the calculations whereas the ratio of the compressor masses m_{s1}/m_{s2} was obviously fixed in the measurements. At a high pressure of 76 bar, the measured efficiency of the two-stage compressor is comparable to that of a single-stage compressor that compresses the gas to 30 bar.

7.3 Conclusions

A two-stage compressor set-up with two parallel cells in the first compression stage and a single cell in the second stage was realised. Nitrogen was used as the working gas. A low pressure of 10 bar was selected to increase the flow that could be realised compared to operation with a low pressure of 1 bar at the cost of a higher cold-stage temperature. The compressor was operated with various configurations, i.e. single-stage compression with one cell and with two parallel cells and two-stage compression with a single cell and with two cells in the first stage. Two-stage compression showed a three times larger efficiency than the single-stage compressor for a high pressure of 30 bar and a set maximum compressor temperature of 700 K. When the two-stage compressor is operated with increasing high pressures, the compressor efficiency decreases. At a high pressure of 76 bar, the efficiency of the two-stage compressor is comparable to that of a single-stage compressor that compresses the gas to 30 bar. The compressor efficiency that was measured for a two-stage compressor with a high pressure of 30 bar was consistent with simulation results.

In the measurements, the compressor cells and their operation were not optimised for efficiency. The selected compressor high temperatures were the same for all high pressures and the wall thicknesses were thicker than assumed by the model from chapter 5. The wall thicknesses and the ratio between Δx_{net2} and Δx_{net1} can be optimised when the compressor is designed for a fixed high pressure. Reduction of the (external) void volume further improves the efficiency.

References

[1] G. F. M. Wiegerinck, J. F. Burger, H. J. Holland, E. Hondebrink, H. J. M. ter Brake, and H. Rogalla. Improvements in sorption compressor design. In R. G. Ross, Jr., editor, *Cryocoolers 13*, pages 513–522, New York, USA, 2004. Springer Science+Business Media.

[2] A. Roth. *Vacuum technology*. Elsevier Science, Amsterdam, 1990.

[3] Swagelok Company, 29500 Solon Road, Solon, OH 44139, USA, http://www.swagelok.com.

[4] Kulite Semiconductor Products, Inc., One Willow Tree Road, Leonia, NJ 07605, USA, http://www.kulite.com.

[5] Bronkhorst High-Tech B.V., Nijverheidsstraat 1A, 7261 AK, Ruurlo, The Netherlands, http://www.bronkhorst.nl.

[6] Druck Ltd., Fir Tree Lane, Groby, Leicester, LE6 0FH, England, http://www.druck.com.

[7] Econosto Nederland B.V., Cypresbaan 63, 2908 LT, Capelle aan de IJssel, Postbus 8988, 3009 TJ Rotterdam, The Netherlands, http://www.econosto.nl.

[8] Heraeus Sensor Technology GmbH, Reinhard-Heraeus-Ring 23, D-63801, Kleinostheim, Germany, http://heraeus-sensor-technology.de.

[9] Omega Engineering, Inc., One Omega Drive, Stamford, Connecticut 06907-0047, USA, http://www.omega.com.

[10] Cryogenic Control Systems, Inc., 17279 La Brisa St., Rancho Santa Fe, CA 92067-7012, USA, http://www.cryocon.com.

Chapter 8

Conclusions and outlook

8.1 Cooling options for the THz demonstrator

The cooling options for an ADC that consists of a high-T_c superconducting digitiser and semiconductor electronics to decimate and further process the high-speed data were explored. The aim is to cool the digitiser to about 30 K. The semiconductors are possibly also cooled and a temperature between 80 K and 150 K seems likely. The cooling load was estimated for three options to realise the ADC demonstrator that differ in the way high-speed data is transported from the superconductor stage to the semiconductor stage. The temperature of the semiconductor stage affects the performance of the semiconductors, the efficiency, mass, and size of the cooler and the heat load to both stages. The heat load at the cooled semiconductor stage was estimated at 15 W and mainly consists of dissipation. The heat load to the superconductor stage depends on the temperature of the semiconductor stage and was estimated at 50 mW, 100 mW, and 250 mW for temperatures of the semiconductor stage of 80 K, 150 K, and room temperature, respectively. When the semiconductors are operated at room temperature, it is attractive to use an optical fibre from the viewpoint of cooling load. There are no significant differences in the load to the superconductor stage between the three configurations when the semiconductors are cooled. Optimisation of the set-up can reduce the cooling load further once more details about the set-up become available. Attention points are reduction of the load caused by conduction through the high-speed data wires and through the support structure.

Four cooling options were identified to realise the cooling of the ADC. In the first option, only the superconductor stage is cooled. In the other three options, the

semiconductor stage is also cooled. An option is to use two separate coolers that each cool from room temperature to the desired temperature. A third option is to use the powerful cooler for the semiconductor stage to precool high-pressure gas that is compressed at room temperature and will be expanded in a Joule-Thomson restriction to cool the superconductors. Since the required cooling powers at the two temperature stages differ significantly, a much more elegant solution would be to mount a small cooler onto the powerful cooler, next to the semiconductor electronics. This cooler should cool from the temperature of the semiconductor stage to that of the superconductor stage. For this purpose, a sorption compressor in combination with a Linde-Hampson cold stage can be used.

A database with 'low-power' cryocoolers was compiled and trends were derived. These were used to estimate input power, mass, and cost of coolers that are suitable for cooling the ADC. To cool the semiconductor stage, Stirling and Joule-Thomson coolers are attractive as they have the highest efficiencies for the required cooling power at 80 K. At low input powers and at 30 K, Stirling and high-frequency pulse tube coolers have the highest COPs. If only the superconductor stage is cooled, the estimated input power is 38 W, the cooler mass is about 18 kg, and a single-unit will cost about 10 k$. There is not much difference in the estimated specifications for the cooling system when the semiconductors are also cooled. When the semiconductor stage is cooled to 80 K, the input powers are about 230 W, the masses about 30 kg, and the coolers will cost some 30 k$. A production of more than roughly 300,000 pieces will reduce the price of the cooling system to below 500 €. The mass of the cooling system is larger than 10 kg, the requirement that was set for the mass. A redesign process is needed to reduce this to lower values. Lower input powers, masses, and prices are expected when the semiconductor stage is cooled to 150 K. An exception is the cooling option that uses a small sorption cooler to cool the superconducting electronics from the temperature of the semiconductor electronics. The efficiency of such a cooler reduces dramatically when its heat sink temperature is increased. As cooler specifications at 150 K were not included in the database, it is difficult to give well-founded estimates of the expected specifications of the cooling system for this operating temperature.

8.2 A 30 K glass-tube cooler

One of the cooling options for the THz demonstrator is to apply a LH cold stage that is precooled by the cooler of the semiconductor stage. The aim is to operate the high-T_c superconducting digitiser at about 30 K. This is in the same temperature range that is required for operating a MgB_2-SQUID. A glass-tube cooler was developed for

cooling a MgB_2-SQUID based on an open-loop Linde-Hampson cycle. The cooler consists of two counterflow heat exchangers and a precooler that were all realised in a tube-in-tube configuration. The high-pressure gas was precooled by leading the tube-in-tube configuration through a bath of liquid nitrogen. The high-pressure gas in the inner tube was cooled via low-pressure gas in the annular gap. A temperature of about 30 K was achieved with a measured nett cooling power of 43 mW. This was in agreement with results from models for the counterflow heat exchangers and the tube-in-tube precooler. One or more small leaks to the vacuum are present in the current set-up that possibly result from thermal stresses. The cooling power and the realised temperature are appropriate for the operation of a MgB_2-SQUID. Mounting of such a SQUID to the set-up will be done in the near future.

8.3 Sorption compressors for cryogenic cooling

Coolers that consist of a sorption compressor with a LH cold stage have several advantages. They are thermally driven and have no moving parts, apart from some valves. As a consequence, they can be scaled to small sizes and can operate with a low vibration level. Besides, wear-related issues hardly play a role giving the potential for a long cooler lifetime. A disadvantage of this cooler type is the relatively complex compressor design. As more complicated components in a system increase the risk of failures, a reduction of complexity would increase the reliability of the cooler. Another drawback of a sorption compressor combined with a LH cold stage is that, in many cases, the cooler is relatively inefficient compared to other types of coolers. Every time the container is to be pressurised, the complete container needs to be heated. The contribution of this heat capacity compared to the heat needed to desorb the gas is significant. Furthermore, a considerable amount of gas is lost in the void volume of the sorber material.

Both the issue of complexity and that of efficiency were addressed. In a traditional compressor lay-out, three or more compressor cells are used that are operated with a fixed phase difference. In chapter 5, an alternative sorption compressor design, consisting of a single compressor cell, two check valves and two buffer volumes, was introduced. Such a design is easier to operate than the traditional lay-out as only one cell needs to be driven and no synchronisation between the phases or with other cells is needed. As there is no need for synchronisation, the cycle time of the compressor can be reduced and more mass flow can be delivered by a single compressor cell compared to the traditional lay-out. The reduction in complexity also results in an improvement of the reliability of the compressor, assuming that the chance of failures is determined by the compressor cells. In that case, the chance that

a single-cell compressor fails is a factor 4 lower compared to a traditional lay-out with four compressor cells.

The single-cell compressor principle was tested using a set-up with a sorption compressor of about 8 cm^3 that was filled with Maxsorb activated carbon. Xenon was used as the working gas. A continuous flow of 0.52 mg/s was established with a pressure swing of 1.39 to 17.0 bar. If the compressor would be connected to a JT expansion stage, a cooling power of about 42 mW at 172 K is expected.

A feature of the single-cell compressor concept is that the pressures in both buffers vary with time. The pressure of the low-pressure buffer is directly related to the temperature of the liquid in the boiler and a variation in this pressure will result in some fluctuation of this temperature. Pressure fluctuations in the high-pressure buffer affect both the flow through the cold stage and the enthalpy of cooling. However, the actual cooling power of the cold stage is buffered by the evaporating liquid in the boiler. Proper design of the buffers can minimise the pressure variations.

The most simple buffers that can be used are 'empty' volumes. However, with this buffer type, the required sizes to keep the pressure variations at an acceptable level are very large compared to the compressor volume of about 8 cm^3. The sizes of the buffers can be reduced by filling them with a sorber material. Alternatively, application of a sorber in the buffers and unchanged buffer sizes will result in smaller pressure variations. In this thesis, the buffer sizes of the passive sorption-based buffers were selected in such a way that the pressure variations would be similar to those of the basic buffers. Comparable pressure variations were achieved with a reduction in the volume of the low-pressure buffer by a factor of 6 whereas a factor 3 of reduction was obtained for the high-pressure buffer. The smaller reduction for the high-pressure buffer results from the flatter shapes of the isotherms at higher pressures.

A further reduction in both size and pressure variation was achieved by actively controlling the pressure in the low-pressure buffer by heating and cooling of the sorber material. A disadvantage is the additional input power that is needed. A non-optimised buffer of 10 cm^3 that was cooled with a TE cooler positioned on the outside was applied. This buffer volume is 5 times smaller than that of the passive-sorption based buffer and 30 times smaller than that of the basic buffer. This non-optimised active buffer already reduced the pressure variation to 21 mbar compared to 0.14 bar for the basic buffer and the passive sorption-based buffer. This pressure variation gives a theoretical variation of the temperature of the liquid in the boiler of 0.29 K. Model calculations for this buffer size give an additional input power of about 10% of that of the compressor. Optimisation of both the thermal design of the buffer and the control algorithm can further reduce the pressure variations and sizes. Apart from

techniques to reduce the pressure variation in the low-pressure buffer, the temperature of the cold tip can also be controlled passively or actively.

The efficiency of a sorption compressor can be increased by applying two-stage compression instead of single-stage compression. Each compressor stage has a smaller pressure swing and less gas is lost in the void volume. Besides, the second-stage compressor starts at a higher pressure at which considerably more gas is adsorbed. A theoretical optimisation of the compressor efficiency showed that by application of two-stage compression considerably higher pressures can be reached compared to the single-stage design. This is beneficial as, within some limits, a higher pressure before expansion yields a higher cold stage efficiency. The efficiency of the cold stage can largely be increased by precooling the high-pressure gas, e.g. with a TE cooler. The enthalpy of precooling directly adds to the cooling enthalpy. Precooling is therefore especially attractive when the high-pressure gas is liquefied in the precooler. For gases like nitrogen, argon, and krypton, this cannot be achieved from room temperature with a TE cooler as temperatures lower than the critical temperature of the gas are then required. These temperatures can be achieved with a precooler that consists of a sorption compressor and a cold stage that has a low pressure smaller than the critical pressure of the working gas. When two-stage compression is applied, this precooler can also be integrated by expanding high-pressure gas from the second stage to the intermediate pressure. This saves a sorption compressor cell at the cost of some efficiency.

A two-stage compressor set-up with two parallel cells in the first compression stage and a single compressor cell in the second stage was realised. Nitrogen was used as the working gas and a low pressure of 10 bar was selected. The compressor was operated in both single-stage and in two-stage mode. Two-stage compression showed a three times larger efficiency than the single-stage compressor for a high pressure of 30 bar and a set maximum compressor temperature of 700 K. The compressor efficiency that was measured for a two-stage compressor with a high pressure of 30 bar was consistent with simulation results. When the two-stage compressor is operated with increasing high pressures, the compressor efficiency decreases. At a high pressure of 76 bar, the efficiency of the two-stage compressor is comparable to that of a single-stage compressor that compresses the gas to 30 bar.

In the measurements, the compressor cells and their operation were not optimised for efficiency. The selected compressor high temperatures were the same for all high pressures and the wall thicknesses were thicker than assumed by the model from chapter 5. The wall thicknesses and the ratio between Δx_{net2} and Δx_{net1} can be optimised when the compressor is designed for a fixed high pressure. Reduction of the (external) void volume further improves the efficiency.

8.4 Outlook

As indicated in section 3.7, there is a growing demand for coolers that have long lifetimes, typically on the order of 5 to 10 years. Attention points related to lifetime for a cooler consisting of a sorption compressor with a Linde-Hampson cold stage are failure of the check valves and the heater and the prevention of clogging of the Joule-Thomson flow restriction [1]. Another issue, about which not much seems to be known, is intrinsic degradation of the physical adsorbent. Two degradation mechanisms seem likely. First of all, fracturing of the coal may occur that is caused by rubbing of the charcoal particles. Fracturing may also result from the subsequent adsorption and desorption of gas. This effect is not likely to occur at small adsorbed fractions but may occur at larger fractions. The latter type of fracturing is observed in chemical sorbers [2]. However, the chemisorption process has a different nature and absorption can result in extremely large lattice expansions of up to about 40%. Fracturing of the coal in a compressor may block the filter at the outlet of the compressor and could limit internal gas flow through the sorber. Fracturing does not reduce the surface area. However, not all surface area may remain accessible. More information on the intrinsic coal degration is needed to provide reliable long-life compressor operation.

For the cooling of non-dissipating devices to cryogenic temperatures, like e.g. low-noise amplifiers, infrared detectors or SQUIDs, standardly available cooling systems are much too large and provide far too much cooling power. For these devices, it would be attractive to make a very small (or 'invisible') cooler, probably integrated with the sensor. Efforts to miniaturise the LH cold stage have been performed in the past and are currently ongoing [3–5]. Sizes smaller than 0.1 cm^3 seem realistic. For such an application, it would be nice, and challenging, to realise a compressor that can drive such a cold stage with a compressor of a comparable size. Alternatively, a relatively large compressor can be used to drive a number of these small cold stages to get cooling on localised spots where it is needed.

A practical issue that is important in the design and optimisation of sorption compressors is the availability of reliable sorption data. Application of two-stage compression especially stresses the need for sorption data at higher pressures as isotherms that are currently available are typically measured up to 10 to 20 bar. The fitting methods as described in chapter 5 do not seem to work fine in our operating regime, i.e. far from the critical point. A better fitting method can improve this. Alternatively, measured sorption isotherms up to the temperatures to which a sorption cell is heated can also solve this problem as interpolation then becomes a reliable option.

The thermal conductivity of adsorbents is generally low and large temperature gradients can occur during cycling. This can largely deteriorate the amount of gas that is desorbed and, as a result, the compressor efficiency. A dynamic model that takes into account thermal and hydraulic effects within the compressor cell would be useful in the design. Such a model gives information on the amount of gas that is supplied, the input power, the compressor efficiency, and the cycle time. With such a model, a compressor design can be made that heats the sorber with a near uniform temperature at a fast pace. This reduces the cycle time, possibly increases the net amount of gas that is cycled and this can largely increase the efficiency of the compressor cell.

References

[1] J. A. Jones and P. M. Golben. Design, life testing, and future designs of cryogenic hydride refrigeration systems. *Cryogenics*, 25:212–219, 1985.

[2] L. Schlapbach, editor. *Hydrogen in intermetallic compounds*, volume 63 and 67 of *Topics in applied physics*. Springer-Verlag, Berlin, 1992.

[3] J. F. Burger. *Cryogenic Microcooling, A micromachined cold stage operating with a sorption compressor in a vapor compression cycle*. PhD thesis, University of Twente, The Netherlands, 1987. downloadable from: http://purl.org/utwente/23470.

[4] P. P. P. M. Lerou, H. Jansen, G. C. F. Venhorst, J. F. Burger, T. T. Veenstra, H. J. Holland, H. J. M. ter Brake, M. Elwenspoek, and H. Rogalla. Progress in micro Joule-Thomson cooling at Twente University. In R. G. Ross, Jr., editor, *Cryocoolers 13*, pages 489–496, New York, USA, 2004. Springer Science.

[5] W. A. Little. Microminiature refrigeration. *Rev. Sci. Instrum*, 55(5):661–680, 1984.

Summary

Coolers that consist of a sorption compressor with a Linde-Hampson (LH) cold stage are thermally driven and have no moving parts, apart from some check valves. As a consequence, they can be scaled to small sizes, can operate with an absolute minimum vibration level and wear-related issues hardly play a role, giving the potential for a long cooler lifetime. As a result, sorption cooling was considered an attractive option to be used for cooling a superconducting AD-convertor. As part of the thesis work, the cooling options were explored of such a convertor consisting of a high-T_c superconducting digitiser and semiconductor electronics to decimate and further process the data. The digitiser should be cooled to 30 K whereas the semiconducting electronics are cooled to between 80 K and 150 K, or are operated at room temperature. An elegant solution to cool the digitiser would be to mount a small sorption cooler onto the relatively large cooler for the semiconductor stage. Unfortunately, sorption coolers have a relatively complex compressor design and have a low efficiency compared to other types of coolers. Both issues were addressed in this work.

To reduce the complexity, an alternative sorption compressor design, consisting of a single compressor cell, two check valves and two buffer volumes, was introduced. This design is easier to operate, can deliver more mass flow with a single compressor cell, and has a higher reliability compared to the traditional lay-out. A property of this novel compressor concept is that the pressures in both buffers vary with time. A variation of the pressure in the low-pressure buffer results in a variation of the cold-tip temperature. Pressure variations in the high-pressure buffer are in general not problematic. Proper design of the buffers can minimise the pressure variations.

Three buffer types were applied: 'empty' volumes, passive sorption-based buffers, and active sorption-based buffers. The sizes of the 'empty' buffers required to keep the pressure variations at an acceptable level are large compared to the compressor volume. The sizes and the pressure variations can be reduced by filling

the buffers with a sorber material. In principle, the pressure variations can be totally suppressed when the pressure of the sorption-based buffer is actively controlled by heating and cooling the sorber material at the cost of additional input power. A non-optimised active buffer already reduced the buffer volume 30 times compared to an 'empty' volume and had a 7 times smaller pressure variation. Model calculations gave an additional input power of about 10% of that of the compressor.

The efficiency of a sorption compressor can be increased by applying two-stage compression instead of single-stage compression. Each compressor stage has a smaller pressure swing and less gas is lost in the void volume. Besides, the second compressor stage starts at a higher pressure at which considerably more gas is adsorbed. A two-stage compressor can also reach considerably higher pressures compared to the single-stage design at comparable compressor efficiencies. This is beneficial as a higher pressure before expansion yields a higher cold-stage efficiency. The efficiency of the cold stage can largely be increased by precooling the high-pressure gas. This is especially attractive when the high-pressure gas is liquefied in the precooler. Two-stage compression gives, in some cases, the opportunity to integrate the precooler by expanding high-pressure gas from the second stage to the intermediate pressure. This saves a sorption compressor cell compared to an external sorption cooler used as a precooler at the cost of some efficiency. A model was developed to determine the efficiency of a sorption compressor. This model was combined with a description of the cold stage to accurately determine and optimise the cooler efficiency. A two-stage compressor set-up was realised. The compressor efficiencies that were measured for this two-stage compressor were consistent with model results.

An alternative cooling option for the ADC is to apply a LH cold stage that is precooled by the cooler of the semiconductor stage. This approach can also be used to cool a MgB_2-SQUID. For this purpose, a glass-tube cooler was developed based on an open-loop LH cycle. The cooler consists of two counterflow heat exchangers and a precooler that were all realised in a tube-in-tube configuration. The high-pressure gas was precooled by leading the tube-in-tube configuration through a bath of liquid nitrogen. The high-pressure gas in the inner tube was cooled via low-pressure gas in the annular gap. A temperature of about 30 K was achieved with a measured net cooling power of 43 mW. This was in agreement with results from models for the counterflow heat exchangers and the tube-in-tube precooler. The cooling power and the realised temperature are appropriate for the operation of a MgB_2-SQUID. Mounting of such a SQUID to the set-up will be done in the near future.

Samenvatting (Summary in Dutch)

Koelers die bestaan uit een sorptiecompressor met een Linde-Hampson (LH) koeltrap worden thermisch aangedreven en hebben, op enkele kleppen na, geen bewegende delen. Daardoor kunnen ze verkleind worden, hebben ze een laag trillingsniveau en speelt slijtage slechts een beperkte rol. Dit geeft de potentie voor een lange levensduur. Sorptiekoeling is daarom een aantrekkelijke optie voor het koelen van een supergeleidende AD-omzetter. Als onderdeel van het proefschrift zijn de koelopties verkend voor zo'n omzetter die bestaat uit een hoge T_c supergeleidende AD-omzetter en halfgeleiderelektronica om de snelheid te verlagen en de data te bewerken. De supergeleidende elektronica moet gekoeld worden naar 30 K terwijl de halfgeleiderelektronica moet werken op een temperatuur tussen 80 K en 150 K of op kamertemperatuur. Een elegante optie om de supergeleiders te koelen is een kleine sorptiekoeler te plaatsen op de relatief grote koeler van de halfgeleidertrap. Sorptiekoelers hebben echter een relatief complex compressorontwerp en hebben een relatief lage efficiëntie vergeleken met andere typen koelers. Beide aspecten zijn onderzocht in dit werk.

Om de complexiteit te verminderen, is een alternatieve sorptiecompressor, bestaande uit een enkele compressorcel, twee passieve kleppen en twee buffervolumes, geïntroduceerd. Dit ontwerp is eenvoudiger aan te sturen, kan meer massastroom leveren met een enkele compressorcel en heeft een hogere betrouwbaarheid vergeleken met het traditionele ontwerp. Een eigenschap van dit concept is dat de drukken in beide buffers fluctueren in de tijd. De druk in de lage druk buffer bepaalt de temperatuur van de koeltrap en drukvariaties resulteren in fluctuaties van deze temperatuur. Drukvariaties in de hoge druk buffer zijn in het algemeen niet problematisch. De drukvariaties kunnen geminimaliseerd worden door aanpassingen in het ontwerp van de buffers.

Drie verschillende typen buffers zijn toegepast: 'lege' volumes, passieve en actieve koolbuffers. De benodigde grootte van de 'lege' buffers om de drukfluctuaties op een acceptabel niveau te houden zijn groot in vergelijking met het volume van

de compressor. De grootte en de drukvariatie kunnen worden gereduceerd door de buffers te vullen met een sorbermateriaal. In principe kunnen de drukvariaties volledig onderdrukt worden wanneer de druk in de koolbuffer actief geregeld wordt door verwarmen en koelen van de sorber. Dit gaat ten koste van de efficëntie van de compressor. Een niet-optimale actieve koolbuffer reduceerde het buffervolume al met een factor 30 in vergelijking met een 'lege' buffer. Tegelijkertijd werd de drukvariatie gereduceerd met een factor 7. Volgens modelberekeningen is een extra hoeveelheid energie nodig van circa 10% dat van de compressor gedurende een cyclus.

De efficiëntie van een sorptiecompressor kan verhoogd worden door tweetraps-compressie toe te passen in plaats van een enkele compressietrap. Elke compressietrap heeft dan een kleinere drukslag waardoor minder gas verloren gaat in het dode volume. Bovendien comprimeert de tweede compressietrap het gas vanaf een hogere druk waarbij significant meer gas wordt geadsorbeerd. Een tweetrapscompressor kan ook significant hogere drukken bereiken in vergelijking met een enkele compressietrap met vergelijkbare efficiënties. Dit is gunstig omdat een hogere druk leidt tot een hogere efficiëntie van de koeltrap. De efficiëntie van de koeltrap kan ook worden verhoogd door voorkoeling van het hoge druk gas. Dit is vooral aantrekkelijk wanneer het hoge druk gas condenseert in de voorkoeler. Tweetrapscompressie geeft, in sommige gevallen, de mogelijkheid om de voorkoeler te integreren door het hoge druk gas van de tweede compressietrap te expanderen naar de tussendruk. Dit bespaart een sorptiecompressorcel in vergelijking met een externe sorptiekoeler die wordt gebruikt als voorkoeler, maar gaat ten koste van de efficiëntie. Een model is ontwikkeld om de efficiëntie van een sorptiecompressor te bepalen. Dit model is gecombineerd met een beschrijving van de koeltrap om de efficiëntie van de hele koeler te bepalen en te optimaliseren. Een opstelling is gerealiseerd om de tweetrapscompressor te testen. De efficiënties van de compressor die gemeten zijn voor deze compressor waren consistent met modelresultaten.

Een alternatieve koeloptie voor de AD-omzetter is het gebruik van een LH koeltrap die wordt voorgekoeld door de koeler van de halfgeleidertrap. Deze aanpak is toegepast om een MgB_2-SQUID te koelen. Een glasbuiskoeler was ontwikkeld die gebaseerd is op een open lus LH cyclus. De koeler bestaat uit twee tegenstroomwarmtewisselaars en een voorkoeler die gerealiseerd zijn in een buis-in-buisconfiguratie. Het hoge druk gas wordt voorgekoeld door de buis-in-buisconfiguratie door een bad met vloeibaar stikstof te voeren. Het hoge druk gas in de binnenste buis wordt dan gekoeld via het lage druk gas in de annulus. Een temperatuur van circa 30 K is bereikt met een gemeten netto koelvermogen van 43 mW. Dit kwam overeen met modelberekeningen. Het koelvermogen en de gerealiseerde temperatuur zijn geschikt voor het koelen van een MgB_2-SQUID.

Acknowledgements

Performing the work that is described in this thesis was a valuable experience with quite some highlights, but also with a lot of hard work. Fortunately, I could rely on and received help from a large number of people. I like to thank everybody that contributed to this work. Some people I would like to mention in particular.

First of all, I would like to thank my promotors Marcel ter Brake and Horst Rogalla. I thank Marcel in particular for his optimism and for his encouraging and positive supervision. I'm grateful to Horst for giving me the opportunity to carry out this work in his research group and for his useful comments during meetings. The research described in this thesis is financially supported by the THz research orientation of the MESA+ research institute of the University of Twente. I thank Gerrit Gerritsma, who unfortunately deceased, and Jaap Flokstra, the project leaders of the THz project, for their discussions and for introducing me into the project.

I would like to thank Johannes Burger for sharing his knowledge and experience and for the fruitful discussions we had. I'm grateful to Harry Holland for all his help, his good advices, and for introducing me into the technical ins and outs of sorption compressors and cryogenic work. Besides, he always took time to discuss matters which I highly appreciated. Erwin Hondebrink helped me enormously in realising the different experimental set-ups. I would especially like to mention the tedious and hard work he performed on the glass-tube cooler and the fast conversion of the single-stage set-up into a two-stage set-up. Without this, chapter 7 would probably not have been written. Thanks a lot for the pleasant cooperation!

Many thanks also go to the other people of the Instrumentation and Cooling group, Bert, Gunter, Pieter, Robert-Jan, Srini, Theo, and the different students, for their help in solving problems, the very pleasant coffee breaks, the borrowing of their equipment, the nice company during trips, and the ice cake that took a honeymoon to defrost. Christian Breukers and Roy de Kinkelder assisted me in realising some of the experimental set-ups as a part of their internship. Thanks for your work! I would also like to thank the other members of the Low Temperature Division for their help,

assistance, and the pleasant time I had. A special thank you in this respect goes to Ans and Inke, not only for their accurate way of handling organisational matters, but also for their many little chats.

In addition, I would like to thank my parents, Antwan and Gerda, Huub and Thea, Wouter, Maarten, David, and my 'mede koude kant', Hanneke and Aline, for their support and interest in my work. Finally, I would like to thank my wife Judith for her advice, her encouraging support, and for her assistance in completing the manuscript.

Gideon Wiegerinck
Enschede, May 2005